

University Library

Author/Filing Title ZHENG

Class Mark T

**Please note that fines are charged on ALL
overdue items.**

| | | |
|--|--|--|
| | | |
|--|--|--|

0403820405



DEPARTMENT OF ELECTRONIC AND ELECTRICAL ENGINEERING
FACULTY OF ENGINEERING
LOUGHBOROUGH UNIVERSITY

OPTO-PHYSIOLOGICAL MODELLING
OF
IMAGING PHOTOPLETHYSMOGRAPHY
BY
JIA ZHENG

A Doctoral Thesis
Submitted in partial fulfilment of the requirements for the award of
Doctor of Philosophy of Loughborough University

Jan 2010

Supervisors: Dr. Sijung Hu
Department of Electronic and Electrical Engineering

© Copyright
JIA ZHENG, 2010



Loughborough
University

Pilkington Library

Date

9/7/10

Class

T

Acc
No.

0403820405

In Memory of My Grandfather

ABSTRACT

Imaging photoplethysmography (IPPG) is one of the emerging medical imaging modalities to visualise peripheral blood perfusion of a specific tissue. Blood perfusion, defined as the blood volume exchange, can provide numerous information of physiological function for tissue and for cardiac-vascular system.

For current IPPG, most published observations are based upon a qualitative nature of blood perfusion. The performance of IPPG is difficult to investigate in these measurements as it is difficult to determine experimentally the effect of changes in the optical properties of segmented biological tissues on the output signals. Thus a representative model for the quantification of this effect is necessary to better understand the underlying principle of the IPPG signal and further improve the applicability of IPPG. This research aims to develop such an appropriate opto-physiological model to quantify IPPG signals with segmented optical properties of tissue.

The opto-physiological model is created by redefining the path length of the Beer-Lambert law. The redefined path length, referred to as mean path length, is derived through the outputs of the Monte Carlo simulation on multi-layered tissue with layered optical properties and specified geometries. The simplified representation of the opto-physiological model eliminates the mathematic complexity of some current propagation models such as photon diffusion model and thus it can be applied in complicated tissue. On the other hand, the accuracy of the model prediction increases by taking scattering into account. This approach is similar to the modified Beer-Lambert law which has been widely used to quantify the concentration of tissue chromophores by a ratiometric approach. Differently, this opto-physiological model quantifies the blood perfusion in a multi-layered format by treating the tissue in a multi-layered structure with respective blood volume changes, rather than a whole and static tissue.

The opto-physiological model is validated via high correlation with corresponding *in-vitro* experiments based upon the multi-layered phantom. This correlation proves the capability of the opto-physiological model, which not only can accurately predict

the output in the range of μ_a and μ_s close to human tissue, but also predict the effect of changes of μ_a and μ_s on the output. There is expected variation between the model prediction and the *in-vivo* experimental outputs due to the difficulty to quantify surface reflection and the sensitivity of the current approach based upon a predefined tissue structure. The model prediction approaches the experimental result when increasing the thickness of the top layer and decreasing the pulsatile volume fraction of tissue. Consequently, as the parameters of the predefined tissue approach real life, the outputs of the opto-physiological model and the experiment increasingly correlate. This research would greatly benefit from a close-to-real tissue structure with accurate measurement of the internal makeup of the tissue bed.

The opto-physiological model contributes to quantifying the output signals of IPPG with the segmented optical properties of tissue and then constructing the layered perfusion mapping of a designated tissue. The layered mapping mainly provides information about optical properties of tissue and illustrates the quantitative relationship between the segmented and the total IPPG signal. There is no blood perfusion in epidermis and top dermis layers as these two layers contain no pulsatile blood. The deep dermis layer is the main contributor up to 80% to the total blood perfusion.

It is concluded that the opto-physiological model is effective and applicable to quantify the IPPG signal with segmented optical properties in a complex tissue structure. The model helps to understand the fundamental of the IPPG signal and implement IPPG with the layered mapping functionality.

ACKNOWLEDGEMENT

I want to express my love and appreciation for my parents and my husband, whose unwavering support during the past years has played a critical role in the completion of this research.

It gives me great pleasure to acknowledge my supervisor, Dr. Sijung Hu. It has been a privilege to be under his supervision, whose contributions have gone well beyond the scope of this work. I am immensely grateful for his undying support, patience and dedication throughout the duration of this research.

I want to express my sincere appreciation to all the members of the Photonics Engineering Group for their friendship and numerous enlightening discussions.

I would like to thank Dr. Vicente Azorin Peris and for his personal contributions and support to my work.

I would like to acknowledge the Department of Electronic and Electrical Engineering for the full support of my studentship during the course of this research.

Finally, I would like to acknowledge my late supervisor, Professor Peter Smith. In the short time that I had the privilege of working with him, his example instilled in me an image of genuine respect and leadership and his memory is one that I will always call upon for guidance.

TABLE OF CONTENTS

ABSTRACT I

ACKNOWLEDGEMENT III

TABLE OF CONTENTS IV

NOTATION TABLE (IN ORDER OF APPEARANCE)..... VIII

1. SUMMARY OF RESEARCH 1

1.1 BACKGROUND 2

1.2 AIM AND OBJECTIVES 3

1.3 RELEVANT PUBLICATIONS 5

2. RESEARCH IN IMAGING PHOTOPLETHYSMOGRAPHY 6

2.1 PHOTOPLETHYSMOGRAPHY 7

2.1.1 Background of physiology..... 7

2.1.2 Optical Principles 11

2.1.3 Operation Principles..... 14

2.2 IMAGING PPG..... 16

2.2.1 Emergence 16

2.2.2 Operation Principles..... 18

2.2.3 Prospects..... 18

2.3 RESEARCH DIRECTION IN IMAGING PPG..... 19

3. OPTO-PHYSIOLOGICAL MODEL..... 21

3.1 PRINCIPLES OF TISSUE OPTICS 22

3.1.1 Refraction 22

3.1.2 Scattering..... 23

3.1.3 Absorption 25

3.2 EXISTING MODELS OF LIGHT PROPAGATION 26

3.2.1 Radiative Transport Theory 27

3.2.1.1 Analytic approximation-photon diffusion model 28

| | |
|--------------------------------------------------------------|-----------|
| 3.2.1.2 Numerical solution-Monte Carlo simulation..... | 28 |
| 3.2.2 Beer-Lambert law | 29 |
| 3.2.3 Modified Beer-Lambert law | 30 |
| 3.3 PROPRIETARY OPTO-PHYSIOLOGICAL MODEL..... | 30 |
| 3.3.1 Opto-Physiological Modelling | 31 |
| 3.3.2 Revised Beer-Lambert Formulation | 32 |
| 3.3.3 Resultant Formulation of Opto-physiological Model..... | 33 |
| 3.3.4 Extended Opto-physiological Model..... | 35 |
| 3.3.4.1 Description of Multi-layered tissue | 35 |
| 3.3.4.2 Multi-layered absorbance | 35 |
| 3.3.4.3 Multi-layered blood perfusion | 36 |
| 3.3.4.3 Specific-layered blood perfusion | 36 |
| 3.3.5 The applicability of Opto-physiological model | 37 |
| 3.3.5.1 Detector-dependent opto-physiological model | 37 |
| 3.3.5.2 Transmission mode and reflection mode | 38 |
| 4. MONTE-CARLO SIMULATION | 39 |
| 4.1 SIMULATION OVERVIEW | 40 |
| 4.2 TISSUE MODEL PREPARATION..... | 42 |
| 4.2.1 Model Structure..... | 42 |
| 4.2.2 Choice of Optical Properties..... | 43 |
| 4.3 RAY-TRACING SETTINGS | 44 |
| 4.4 POST DATA PROCESSING..... | 44 |
| 5. VALIDATION PLATFORM | 49 |
| 5.1 IMAGING PPG SYSTEM | 50 |
| 5.1.1 Engineering Setup..... | 50 |
| 5.1.1.1 Imaging Hardware..... | 50 |
| 5.1.1.2 Illumination Configuration | 52 |
| 5.1.1.3 Control layout | 55 |
| 5.1.2 Post Signal Processing | 55 |
| 5.2 VALIDATION PROCEDURE | 57 |
| 5.2.1 Phantom-Based Validation | 58 |
| 5.2.1.1 Experimental phantom preparation..... | 58 |
| 5.2.1.2 Multi-layered phantom model in simulation..... | 62 |
| 5.2.1.3 Validation analysis..... | 63 |

| | |
|-----------------------------------------------------------------------------------------------|------------|
| 5.2.2 Subject-Based Validation..... | 63 |
| 5.2.2.1 <i>Experiment preparation.....</i> | 63 |
| 5.2.2.2 <i>Skin tissue model in simulation.....</i> | 66 |
| 5.2.2.3 <i>Validation analysis.....</i> | 70 |
| 5.3 MAPPING FUNCTION..... | 70 |
| 5.3.1 2-D mapping of static and dynamic component | 71 |
| 5.3.2 Layered mapping of blood perfusion..... | 71 |
| 5.3.3 Spatial Resolution | 73 |
| 5.3.1.1 <i>Effect of camera parameters on imaging resolution</i> | 73 |
| 5.3.1.2 <i>Effect of quality of IPPG signal on ROI_{ip}.....</i> | 75 |
| 5.3.1.3 <i>Effect of tissue's spatial point spread function on ROI_{ip}.....</i> | 76 |
| 6. EXPERIMENTS, RESULTS AND DISCUSSIONS | 80 |
| 6.1 VALIDATION BASED ON ONE-LAYERED PHANTOM..... | 81 |
| 6.1.1 Results of Experiment | 81 |
| 6.1.1.1 <i>Experimental setup</i> | 81 |
| 6.1.1.2 <i>Experimental protocol</i> | 82 |
| 6.1.1.3 <i>Experimental Results and discussion.....</i> | 83 |
| 6.1.2 Results of Simulation..... | 85 |
| 6.1.2.1 <i>Simulation setup.....</i> | 85 |
| 6.1.2.2 <i>Simulation Results and discussion.....</i> | 86 |
| 6.1.3 Validation Analysis..... | 87 |
| 6.2 VALIDATION BASED ON MULTI-LAYERED PHANTOM..... | 90 |
| 6.2.1 Results of Experiment | 90 |
| 6.2.1.1 <i>Experimental protocol</i> | 90 |
| 6.2.1.2 <i>Experimental Results and Discussion.....</i> | 91 |
| 6.2.2 Results of Simulation..... | 93 |
| 6.2.2.1 <i>Simulation setup.....</i> | 93 |
| 6.2.2.2 <i>Simulation Results and Discussion.....</i> | 94 |
| 6.2.3 Validation Analysis..... | 96 |
| 6.3 SUBJECT-BASED VALIDATION..... | 99 |
| 6.3.1 Display of PPG waveform..... | 100 |
| 6.3.1.1 <i>Experimental protocol</i> | 100 |
| 6.3.1.2 <i>Experimental Results and discussion.....</i> | 101 |
| 6.3.2 Cardiac-Vascular parameters | 103 |

| | |
|----------------------------------------------------------------|------------|
| 6.3.2.1 <i>Experimental protocol</i> | 103 |
| 6.3.2.2 <i>Experimental Results and discussion</i> | 103 |
| 6.3.3 Reliability | 106 |
| 6.3.3.1 <i>Experimental protocol</i> | 106 |
| 6.3.3.2 <i>Results and Discussion</i> | 107 |
| 6.3.4 Validation Analysis | 109 |
| 6.3.4.1 <i>Results of subject-based experiment</i> | 109 |
| 6.3.4.2 <i>Results of skin-model-based simulation</i> | 110 |
| 6.3.4.3 <i>Validation Results</i> | 111 |
| 6.4 RESULTS OF PERFUSION MAPPING | 115 |
| 6.4.1 Experimental setup and protocol | 115 |
| 6.4.2 2-D Mapping of Static and dynamic component | 115 |
| 6.4.2.1 <i>Static component mapping</i> | 115 |
| 6.4.2.2 <i>Dynamic component mapping</i> | 116 |
| 6.4.3 Layered Mapping of Blood Perfusion | 119 |
| 7. CONCLUSIONS AND FURTHER WORK | 122 |
| 7.1 CONCLUSIONS | 123 |
| 7.1.1 Opto-Physiological Modelling | 123 |
| 7.1.2 Experiments | 124 |
| 7.1.3 Validation | 124 |
| 7.1.4 Perfusion Mapping | 124 |
| 7.2 FURTHER WORK | 125 |
| 7.2.1 Effective Monte-Carlo Engine | 125 |
| 7.2.2 Close-to-real Tissue model | 126 |
| 7.2.3 Model Settings | 127 |
| 7.2.3 Dynamic Component Validation | 128 |
| REFERENCE | 129 |
| APPENDICES | |
| I Graphic User Interface of OptiCAD software | 141 |
| II LabView Application for Frame Grabber | 142 |
| III LabView Application for DISCO4 PPG Board | 144 |
| IV Specification of dye, FD&C # 1 | 146 |

NOTATION TABLE (in order of appearance)

| | |
|-------------------------------------------------------------------------------------------------------------------|--------------------------------------------------------------|
| AC: dynamic component of PPG signal | k: total number of layers in a medium |
| DC: static component of PPG signal | i: number of layer |
| n: refractive index | λ : wavelength |
| v: speed of light transportation | I_s : scattered light intensity when $\mu_a=0$ |
| θ : angle of light deflection | x,y,z: axes of coordinate system |
| d: thickness of medium | f: volume fraction |
| I_0 : incident light intensity | j: component of a medium |
| I: direct transmitted light intensity without considering scattering or scattered light intensity with scattering | V: vertex structure |
| μ_s : scattering coefficient | S: segment structure |
| g: anisotropic factor | D: detector structure |
| μ'_s : reduced scattering coefficient | G: Global structure |
| μ_a : absorption coefficient | p: pointer |
| \vec{r} : position vector | t: time |
| \vec{n} : direction vector | ac: mean peak-to-peak amplitude of AC |
| P_d : scattering probability density function | dc: mean value of DC |
| Ω : solid angle | N: total number |
| l: path length | R: ratio |
| A: absorbance | dis: distance between lens and imaging plane or object plane |
| B: scattering-dependent factor | dia: diameter of lens |
| Sen: sensor-dependent factor | NA: numerical aperture |
| Geo: geometry-dependent factor | fl: focal length of lens |
| M: a composite medium | Mag: magnification of lens |
| m: a layer in a composite medium | Res: resolution |
| | w: weight function |

1. SUMMARY OF RESEARCH

Imaging PPG (IPPG) is one of the medical imaging modalities based upon the light-tissue interaction to monitor peripheral blood perfusion of tissue. It takes the advantages of conventional PPG, but removes the primary limitations of spot measurement and contact sensor. However, lack of a sufficiently accurate model to quantitatively describe the principle has limited the development of this technology. As such, this is the potential area of research when attempting to increase the applicability of the technology.

1.1 BACKGROUND

Photoplethysmography (PPG) is an optical bio-monitoring technique that non-invasively measures peripheral blood perfusion *in-vivo*. Its ease of use and convenience make it an attractive area of research in the biomedical and clinical community. However, spot measurement, contact sensor and over simplified model have limited its applicability and have halted its evolution to a near standstill.

The past few years have witnessed the revolutionary development of some conventional medical optical technologies into imaging or more specifically tomography as a result of the considerable advances in understanding light migration through tissue and the resulting development of tomographic algorithms. The potential that conventional PPG could be evolved into imaging PPG was soon realised. Different from Doppler related technologies^{[1][2]}, IPPG aims to detect the blood volume change of tissue rather than blood velocity. Besides, IPPG can deliver other important physiological parameters such as heart rate variability (HRV) and pulse transit time (PTT). IPPG takes the advantages of conventional PPG, but removes the primary limitations of spot measurement and contact sensor. It facilitates the continuous and real-time measurement of blood perfusion in different compartments of tissue. It has excellent potential towards remote sensing, reducing the physical restrictions and cabling associated with patient monitoring.

To better understand the underlying principle of IPPG and further increase the applicability of the technology, an appropriate model is essential to quantify the effects of the optical properties of biological tissues on the output signal and contributes to blood perfusion mapping of a designated tissue.

In this thesis, the approach to generate such a model of IPPG is to create an opto-physiological model through the use of Monte Carlo (MC) simulation on multi-layered tissue. The concept behind this approach is to describe the complex light-tissue interaction in a simplified format with representative parameters. As the parameters of the opto-physiological model approach those occurring in the corresponding real-life situation, the outputs of the model and empirical

measurement increasingly correlate. The high correlation proves the validity of the model and hence its ability to predict the real-life output.

1.2 AIM AND OBJECTIVES

The aim of this research is to create an appropriate opto-physiological model of IPPG to mathematically describe the relationship between segmented optical properties and the IPPG signal. The model can be validated through the correlation between the prediction of the opto-physiological model and the experimental output. Subsequently, this validated model can be applied into real-life measurements to construct the segmented perfusion mapping of a designated tissue.

From the aim, the following objectives are inferred:

- 1) For PPG and IPPG, the relevant concepts of physiology, the principles of operation, the applicability, the engineering issues and the limitations are recounted (Chapter 2).
- 2) Relevant concepts of optics, specifically those which pertain to human tissue optics is examined and put into context (Chapter 3).
- 3) The strengths and weaknesses of the currently used mathematical models including the Radiative Transport Theorem (RTT), the Beer-Lambert law and the modified Beer-Lambert law are discussed from the standpoint of the application in IPPG. Based on the advantages of these existing models, an opto-physiological model of IPPG is created by redefining the key parameter in the Beer-Lambert law through the use of the MC simulation, which is regarded as a numerical solution of RTT (Chapter 3).
- 4) The structure and dataflow of the MC simulation for optical propagation through tissue of arbitrary geometries is detailed along with all output data processing algorithms to generate the redefined parameter, referred to as mean path length *MPL*, for the opto-physiological model (Chapter 4).

- 5) Specifications of validation experiments including all hardware setup, control layout, phantom preparation, and data processing algorithms used for generation of experimental results are provided (Chapter 5).
- 6) The validation procedure based upon the output of the opto-physiological model and real-life experiments is detailed. Additionally, the function of perfusion mapping is detailed (Chapter 5).
- 7) The results of the opto-physiological model and corresponding validation experiments are distilled with emphasis on the correlation between theoretical and experimental outputs, followed by an in-depth discussion of their accuracy and sensitivity (Chapter 6).
- 8) The results of segmented perfusion mapping in a designated tissue are presented, followed by a detailed explanation of the underlying principle (Chapter 6).
- 9) The conclusions which the results lead to are summarised, and suggestions are made for future work with respect to the MC simulation (Chapter 7).

1.3 RELEVANT PUBLICATIONS

The following articles related to this work have been published:

Zheng J., Hu S., Echiadis A. S., Azorin-Peris V., Shi P., and Chouliaras V., “A remote approach to measure blood perfusion from the human face,” *Proc. SPIE*, **7169**, 716917 (2009).

Zheng J., Hu. S., Azorin-Peris V., Echiadis A., Chouliaras V. and Summers R., “Remote simultaneous dual wavelength imaging photoplethysmography: a further step towards 3-D mapping of skin blood microcirculation,” *Proc. SPIE*, **6850**, 68500S(2008).

Hu S., **Zheng J.**, Chouliaras V., and Summers, R., “Feasibility of Imaging Photoplethysmography,” *BMEI 2008 International Conference*, **2**, pp. 72 – 75 (2008).

Zheng J. and Hu S., “The preliminary investigation of imaging photoplethysmographic system,” *J. Physics: Conference Series*, **85**, 012031 (2007).

Other publications related to work carried out in relevant areas of research are listed below:

Zheng J., Hu S., Xin S. and Crabtree V. P., “The effect of postural changes on lower limb blood volume with non-invasive photoplethysmography,” *J. Med. Eng. Technol.*, **32(5)**, pp. 358-364 (2008).

Xin S., Hu, S., Crabtree V. P., **Zheng J.**, Azorin-Peris V., Echiadis A., Smith P. R., “Investigation of blood pulse PPG signal regulation on toe effect of body posture and lower limb height,” *J. Zhejiang University – Science A*, **8**, pp. 916-920, 2007.

Chouliaras V., Hu S., Azorin-Peris V., Echiadis A., Summers R., **Zheng J.**, King I., “Real-time VLSI architecture for bio-medical monitoring,” *Proc. ITAB 2008*, Shenzhen, China, 2008.

2. RESEARCH IN IMAGING PHOTOPLETHYSMOGRAPHY

PPG is an optical bio-monitoring technique that non-invasively measures peripheral blood perfusion *in-vivo*. Among its applications, IPPG is recently emerging and is most attractive thanks to its great capability of remote imaging. By a need of understanding and predicting the effect of optical properties on the IPPG signal, modelling of the optical propagation in biological tissue is under research.

2.1 PHOTOPLETHYSMOGRAPHY

PPG, the origin of IPPG, is an optical bio-monitoring technique firstly devised in the 1930's for the non-invasive measurement of peripheral blood perfusion *in-vivo* ^[3]. Blood perfusion generated by heartbeat, defined as the blood volume change in PPG, can provide a measure of physiological function for tissue and for the cardiac-vascular system. The ease of use and convenience of PPG make it an attractive area of research in the biomedical and clinical community ^[4].

Plethysmography is a combination of the Greek words, 'plethysmos' meaning increase and 'graph' which translates as write, and is used mainly to determine and register the volume variations within an organ or whole body ^[5]. The term photoelectric plethysmography, also known as photoplethysmography (PPG), meaning optical plethysmography, is therefore to describe the electro-optic technique of measuring the cardio-vascular blood volume change at a measurement site ^[6]. The observed pulse wave now referred to as the PPG signal can deliver clinically valuable information for the study of cardiovascular system ^[7] and skin microcirculation ^[8].

PPG is the core technology on which IPPG is based. An introduction of the fundamental concepts of PPG can help to understand the development of IPPG and its principle. First of all, a basic knowledge of the human circulatory system and of the optical principle is required.

2.1.1 Background of physiology

The main functions of the human circulatory system are to deliver oxygen and nutrients to all the cells in the body and to remove waste products from the cells. The system is also responsible for the transportation of hormones and for regulation of body temperature. The human circulatory system is essentially composed of the lungs, the heart, and the venous and arterial trees. The closed path of blood circulation is as follows: The heart pumps blood out of the right ventricle into the lungs via the pulmonary arteries. In the lungs, carbon dioxide is released from the blood and replaced by oxygen. Oxygenated blood from the lungs gathers in the left

atrium of the heart and passes to the left ventricle. The left ventricle pumps this blood out to the whole body via the arteries. After the oxygen in the blood is released into the tissue and organs of the body and carbon dioxide is collected, the blood returns to the right atrium via the veins, where it passes into the right ventricle and the cycle repeats, as shown in Figure 2. 1.

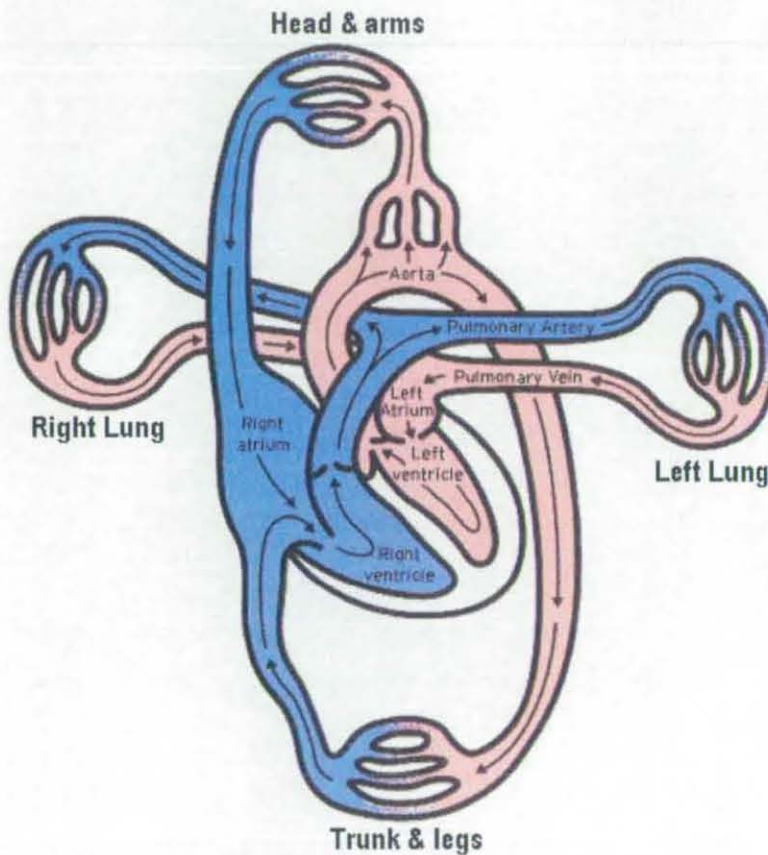


Figure 2. 1 A simplified diagram of the circulatory system (image courtesy of <https://eapbiofield.wikispaces.com/FRF+Circulatory+System>).

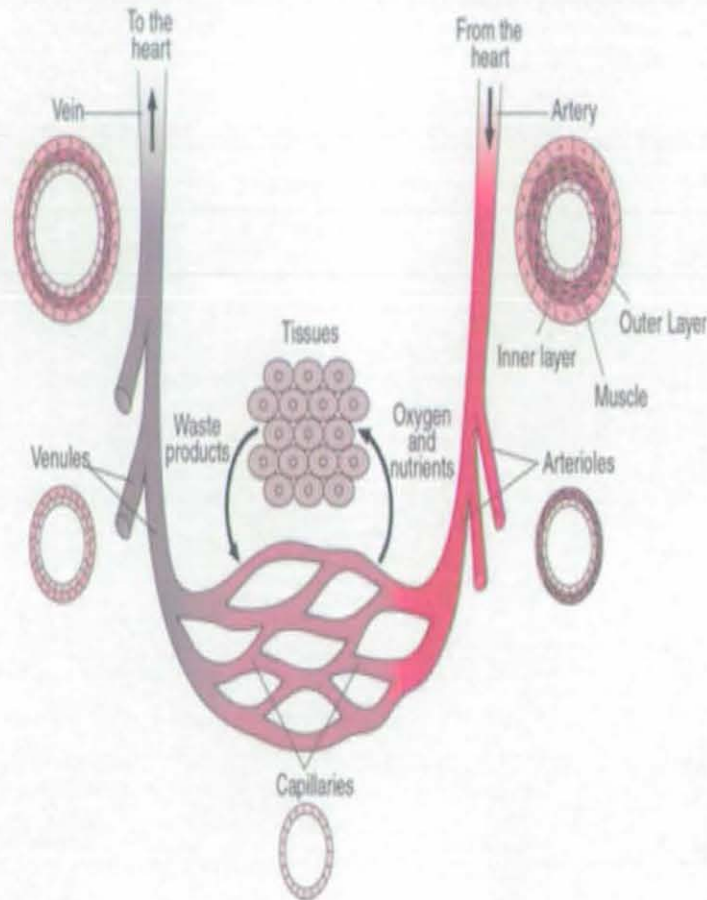


Figure 2. 2 Structure of the vascular tree, with relative vessel wall thicknesses and capillary-tissue fluid exchange (image courtesy of www.merck.com).

Blood circulation as described above covers two stages of the heartbeat: during systole, the heart pumps blood both to the body and to the lungs, and during diastole, both ventricles fill with blood. The arteries are the thick walled vessels that withstand the highest pressures and largest pressure oscillations in the vascular tree as shown in Figure 2. 2. Arteries branch into arterioles and then into capillaries, thus reducing blood pressure, pressure oscillation and velocity due to an increase in corresponding cross-sectional area in the capillaries, as detailed in Figure 2. 3. Blood leaving the capillaries converges into venules and then veins. The latter are large, thin walled vessels, where blood travels with the aid of gravitational pressure. The effect anastomosis also exists, in which arterial blood is shunted directly to the venous system without traversing capillaries.

The heart pumps blood into the blood circulation, the arteries then expand hence increasing the blood volume fraction and therefore the absorption of light in the tissue increases. Thus the fraction of light attenuated by the blood fluctuates as a function of this pumping action of the heart. PPG measures changes in blood volume; therefore the pulsatile nature of arterial blood is inherently important to the technology.

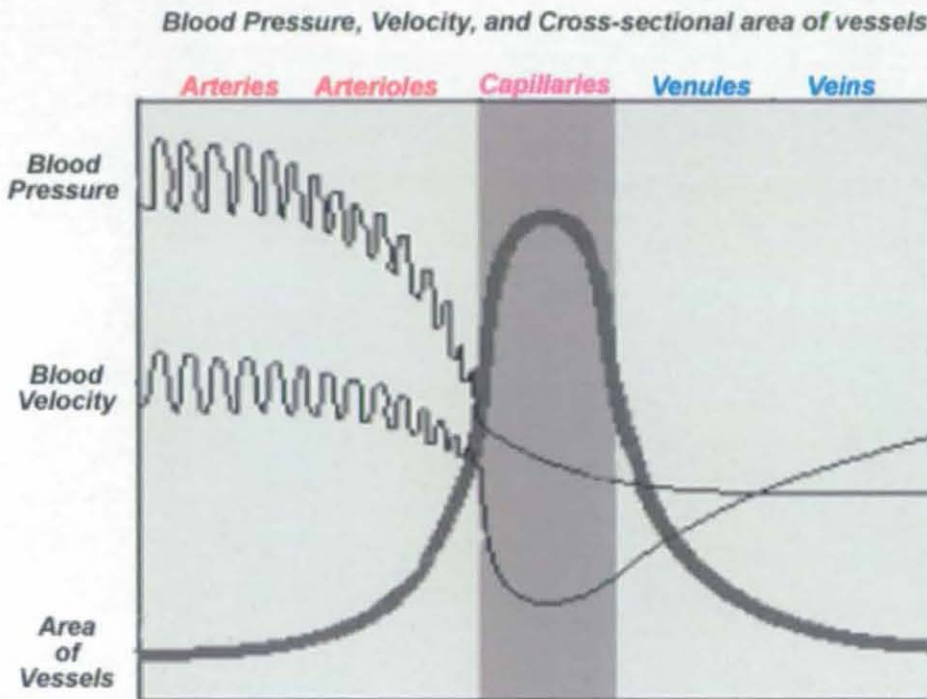


Figure 2. 3 Comparative cross-sectional analyses of scales in the cardiovascular tree (image courtesy of <http://www.coolschool.ca/lor/BI12/unit9/U09L08.htm>).

An exchange of oxygen, nutrients and waste products takes place between the blood and adjacent tissues as the blood traverses the capillaries, where its reduced speed allows this to occur effectively. Out of all the organs of the body that are perfused with blood, skin has a high relevance in PPG as its surface is the site onto which sensing probes are placed. Consequently, its anatomical and physiological characteristics always influence the technology. Human skin is essentially divided into three layers, namely, epidermis, dermis and subcutaneous fat. The epidermis is the outermost layer, in which the skin pigment melanin is produced by cells called melanocytes. This pigment is responsible for the protection of the skin against harmful radiation by means of absorption. The dermis houses blood vessels which

are largely categorised as two vascular beds, namely the superficial and deep vascular plexus. Subcutaneous tissue is a layer of fat which houses larger blood vessels, nerves and connective tissue and it plays an important role in the regulation of skin and body temperature. A diagram of skin is presented in Figure 2. 4.

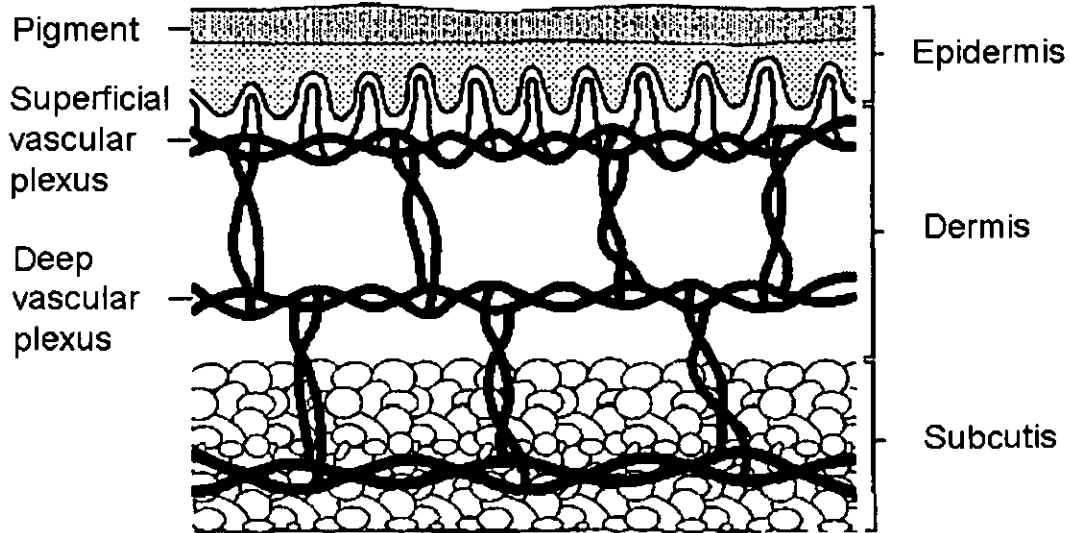


Figure 2. 4 A diagram of skin ^[9].

2.1.2 Optical Principles

As an optical bio-monitoring technique, PPG requires a light source and detector to function, and relies on the optical properties of biological tissue. The fundamental modus-operandi of PPG technology is the optical detection of the pulsatile cardio-vascular pulse wave, referred to as blood perfusion, as it travels throughout the body. PPG can be performed in transmission mode or reflection mode ^[10]. In the former, the light source and detector are facing each other and are usually placed on opposite sides of the tissue under inspection, where as in reflection mode, the light source and detector are facing the same direction and are usually adjacent.

In the transmission mode as shown in Figure 2. 5, observation of the PPG signal can be achieved by illumination of a suitable pulsating vascular bed. The monitoring sites for the transmission mode are limited to well perfused areas of the body that are transparent enough for the transmitted light to be easily detected, such as the fingers and earlobes.

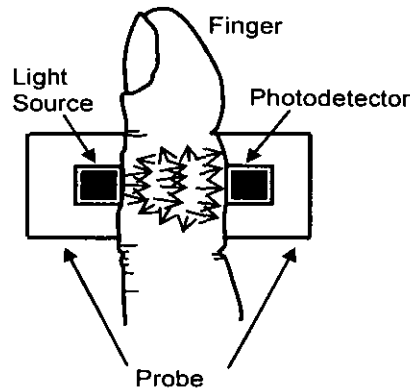


Figure 2. 5 PPG probe in transmission mode.

In the reflection mode as shown in Figure 2. 6, both the source and the detector are positioned at the skin surface, with back-scattered light returning from a range of depths within the highly scattering tissue. In the near-infrared (NIR) spectral region, light can penetrate several millimetres into tissue ^[11] where the dynamic absorption of the pulsatile vascular bed modulates the total scattered light. There are certain advantages in using reflection mode rather than transmission mode. The design of the reflection probe is simpler with greater mechanical strength, and the reflection mode relies on backscattered light returning to the skin surface, which allows it to be used in most parts of the human body, such as the forehead, limbs and chest ^[12].

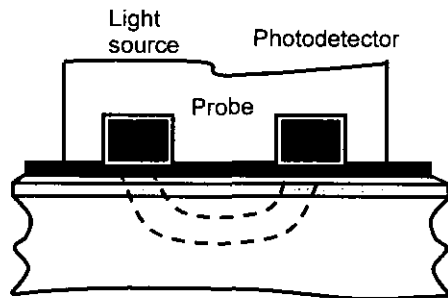


Figure 2. 6 PPG probe in reflection mode.

Ideally for PPG, blood would absorb greatly and all other tissue would absorb weakly as this would provide high contrast, allowing for accurate monitoring of blood perfusion. Besides blood, the main absorption components of human tissue are mainly water and the pigment melanin. Figure 2. 7 and Figure 2. 8 illustrate that light

is increasingly absorbed by melanin towards the ultra-violet (UV) band and greatly absorbed by water towards the microwave band.

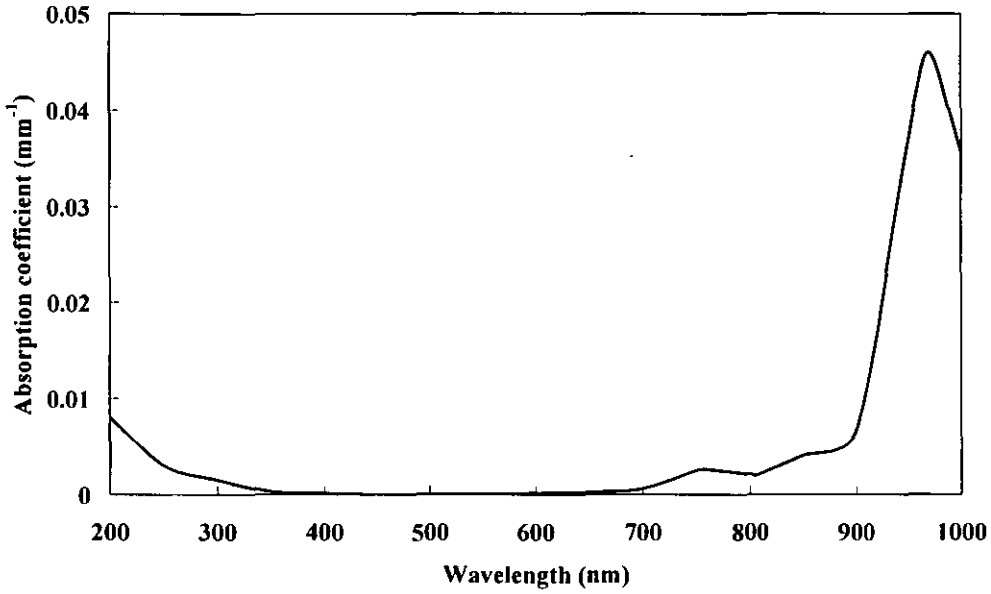


Figure 2. 7 Absorption spectra of water ^[13].

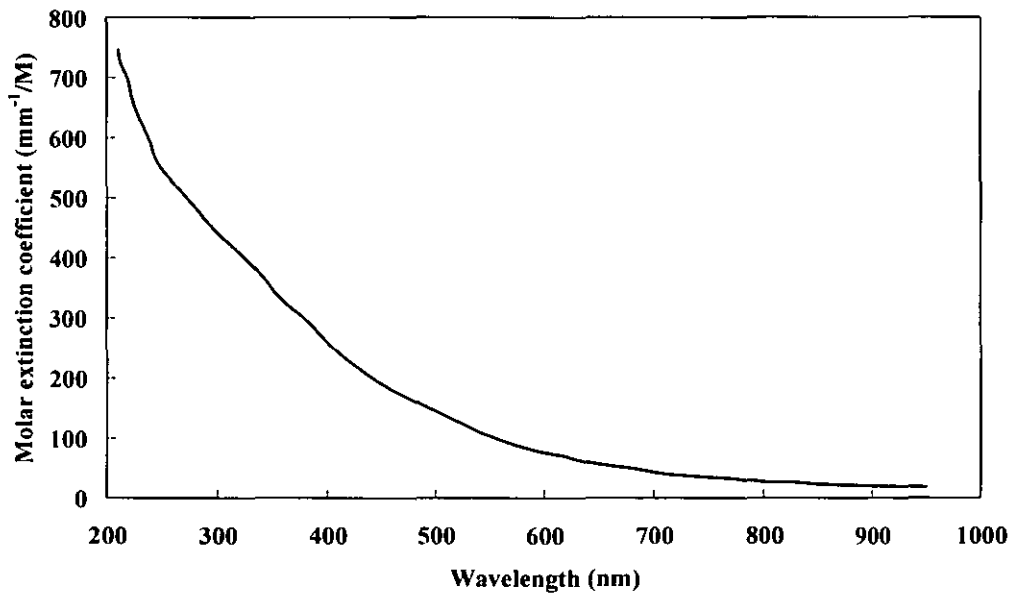


Figure 2. 8 Absorption spectra of melanin ^[14].

These factors limit practical wavelengths of a PPG light source roughly to the NIR spectral range of 600-1000 nm. Since the volume fraction of blood accounts for only

a few percent of the total tissues, its effect on light transport is moderate. On the other hand, when light in the range of 600-1000 nm strikes a blood vessel, it encounters the full strong absorption of whole blood. Hence, blood governs light absorption in the NIR spectral range, and tissue governs light transport.

There are two primary absorbers in blood of light in the NIR spectral region including both oxygenated and deoxygenated haemoglobin ^[15]. The simultaneous region of absorption at NIR wavelengths of these two absorbers in tissue is illustrated in Figure 2. 9.

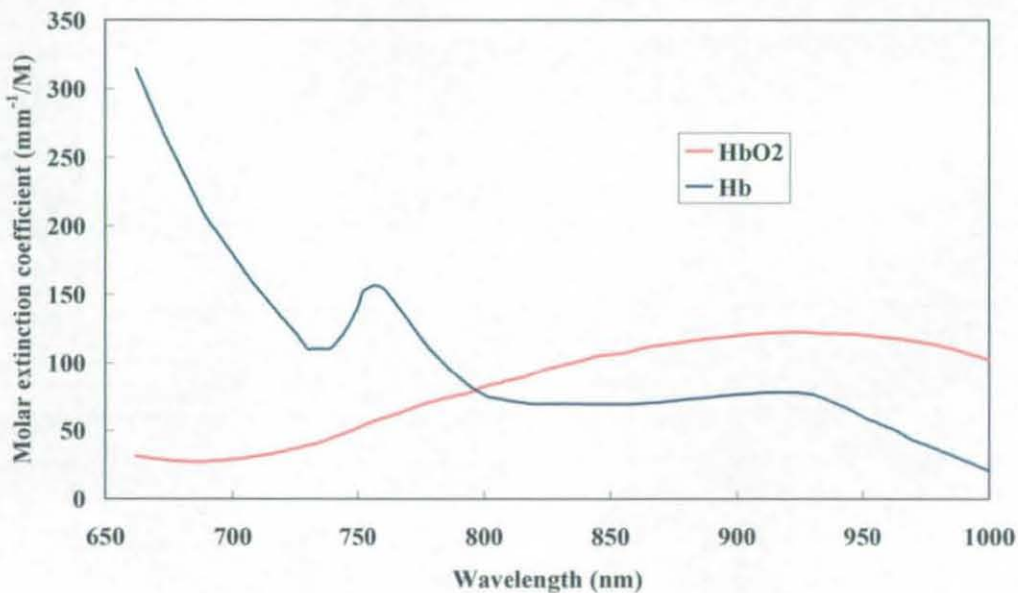


Figure 2. 9 Absorption spectra of oxygenated (HbO₂) and deoxygenated (Hb) haemoglobin ^[16] in the NIR spectral region.

The concentrations of oxygenated and deoxygenated haemoglobin change according to the function and metabolism of the tissue. The corresponding changes in concentration can be reflected in absorption variation and thus provide clinically useful physiological information, which is the fundamental principle of pulse oximetry ^[17], another application of PPG.

2.1.3 Operation Principles

Due to the limited wavelength selection in the NIR spectral range, PPG can monitor blood. Moreover, the technique itself is only made possible by the dynamic pulsation

of arterial blood. During the systole stage, the amount of blood increases resulting in more light absorption. During the diastole stage, the amount of blood decreased resulting less light absorption. Thus the measured waveform of PPG, referred to as the PPG signal, contains a dynamic signal *AC* due to the arterial pulsation of blood corresponding to the absorption change in the systole and diastole stage, and a much larger, slowly changing quasi-static signal *DC* governed to a large extent by the static component in tissue such as baseline arterial and venous blood, bloodless tissue and bone etc., as shown in Figure 2. 10.

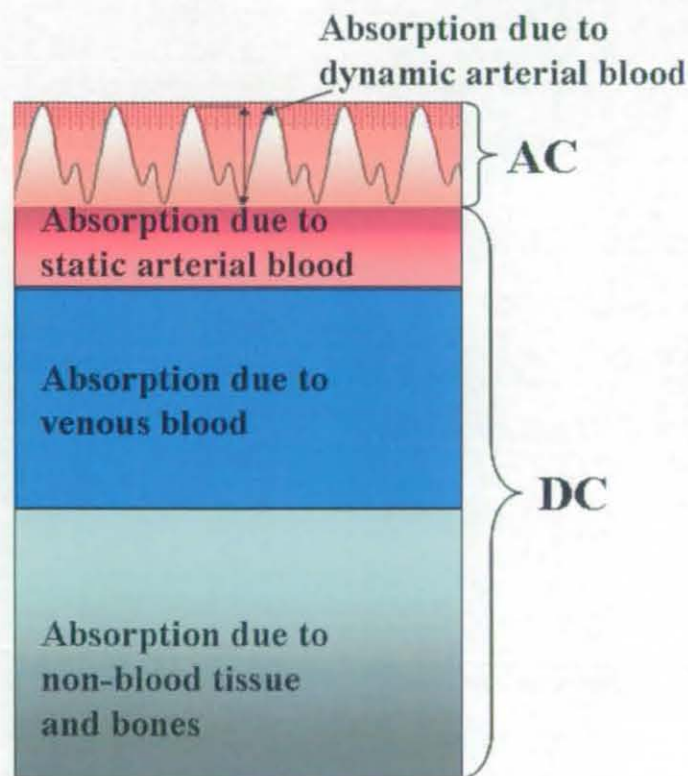


Figure 2. 10 Relative absorption of blood and tissue.

Observation of the measured intensity in both transmission and reflection modes indicates that the pulsatile component accounts for only a very small proportion of the total intensity^[18]. This results from the fact that a skin vascular bed contains only a small amount of blood about 2%-5%^[19], which itself experiences only a volumetric change of a few percent about 5%^[20] with the cardio-vascular pulse wave. A significant correlation has been reported between *AC* signals and the dynamic strain-gauge plethysmography^[21] which measures the changes of the lengthening of the gauge due to blood volume change. This correlation verifies that the predominant

cause of AC is the pulsatile blood ^[22]. It has also been demonstrated that the amplitude of AC signal is related to variations in blood volume, i.e. blood perfusion, throughout the cardiac cycle ^[23].

Assuming that the optical characteristics of bloodless tissue remain constant, the resultant dynamic component AC of the PPG signal can be solely attributed to pulsatile arterial blood, i.e. blood perfusion ^[6], as shown in Figure 2. 11, and any quasi-static DC components can be attributed to changes in non-pulsatile arterial and venous blood due to breathing or otherwise ^{[24] [25] [26]}.

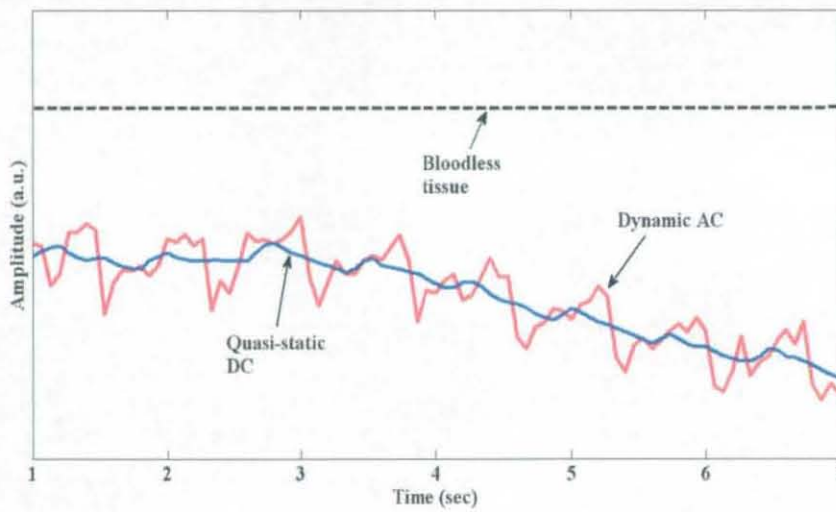


Figure 2. 11 Components of a raw PPG signal.

2.2 IMAGING PPG

Remote-sensing imaging offers additional values for any parameter by appealing to human cognition and literally facilitates insights that would otherwise be difficult or even impossible to obtain. Thus non-contact or remote camera-based IPPG has recently developed from PPG to meet this demand. In this section, the operation principles, applicability, engineering issues and challenges of IPPG are recounted.

2.2.1 Emergence

Compared to other measurement techniques of blood perfusion such as Laser Doppler, PPG is easy to setup, simple to use, absolutely safe and low in cost.

However, current PPG can only monitor the blood perfusion at a single site with a volume of a few cubic centimetres. Another obvious disadvantage is that its sensor must be attached to the tissue of the subject, which restricts its applications to some clinical situations such as wound diagnostics.

The last decade has witnessed the enormous progress of optical imaging technologies for biomedical applications. With the recent evolution of several technologies such as laser Doppler and spectroscopy into imaging area, it is soon realised that PPG could be extended to imaging as well. The basic concept of this, namely imaging PPG (IPPG), is to illuminate the specific tissue with an array of light sources and to measure the light leaving the tissue with multiple detectors. The introduction of the fast digital camera inspires the development of this concept to allow non-contact monitoring from a larger field of view by applying multi-wavelength illumination sources.

IPPG has been created towards remote sensing and reduction of the physical restrictions and cabling associated with patient monitoring. It can benefit in removal of potentially injurious wires from magnetic resonance imaging (MRI) machines^[27]. Different with other technologies of perfusion imaging such as laser Doppler perfusion imaging (LDPI) and laser speckle contrast analysis (LASCA)^[28], IPPG is aiming to detect the blood volume change of tissue, rather than blood velocity. Blood perfusion refers to the process of nutritive delivery of arterial blood to a capillary bed in biological tissue^[29]. Strictly speaking, perfusion implies both the amount of blood volume change and the blood velocity. Thus IPPG, LDPI or LASCA look at blood perfusion from different aspects. Besides blood perfusion, IPPG can deliver other important physiological parameters such as heart rate variability (HRV)^[30] which reflects the time-varying influence of the autonomic nervous system and pulse transit time (PTT)^[31] which is related to the arterial compliance.

The feasibility of a non-contact camera-based PPG has been well illustrated for the visualisation of blood perfusion^[32], which demonstrated the simultaneous capture of PPG waveforms from the extremities at three wavelengths (660nm, 840nm and 905nm) in both transmission and reflection modes. Another work has reported a reflection mode capture of “heartcycle-related” pulsatile variations using a CMOS camera^[33], with illumination at 660, 810, and 940 nm. An additional research^[34]

presented a camera-based system capable of capturing two PPG signals at two wavelengths simultaneously in a non-contact manner.

2.2.2 Operation Principles

IPPG has relatively similar background physiology and optical principles with conventional PPG. IPPG measures blood perfusion of multi-layered tissue from a large area. The measured waveform of IPPG, referred to as the IPPG signal, contains a dynamic component *AC* that represents the arterial pulsation, i.e. blood perfusion, and a static component *DC* governed by the static component in tissue such as the venous blood and bloodless tissue as shown previously in Figure 2. 10.

Similar with conventional PPG, the practical wavelength choice of the illumination source for IPPG is limited in the NIR spectral range of 600-1000nm, allowing high contrast in the absorption of blood compared to other compounds of tissue such as water and melanin as shown previously in Figure 2. 7, Figure 2. 8 and Figure 2. 9.

The key sensing part of an IPPG system is the camera which collects the scattered photons coming from the illuminated tissue. The camera needs to have a high sensitivity over the NIR spectral range, and the flexibility of choosing variable readout speed and exposure time. CCD (charge-coupled device) and CMOS (complimentary metal-oxide semiconductor) camera sensors are currently in a wide range of biomedical research, which aim to convert light into electrons. The camera with CCD sensors creates high-quality, low-noise images, while consumes more power and more expensive. CMOS sensors, traditionally, are more susceptible to noise, but capable of reaching higher frame rate, consume less power and are less expensive.

2.2.3 Prospects

IPPG is non-invasive, non-ionizing, inexpensive and portable, making it possible as a widespread use for biomedical research. These combined features can have a significant impact on a number of many medical and health-care situations. The following section outlines some potential applications of IPPG.

Burned assessment: IPPG is configured to be a contactless way to image the blood perfusion of tissue, so perfusion mapping for burned assessment is an obvious application area. High perfusion corresponds to superficial dermal burns, which heal with dressings and conservative management; burns with low perfusion require surgical management ^[35].

Healing processes: IPPG could also be a new tool of blood perfusion in assessment of the healing progress. Vladimir Blazek ^[36] has observed perfusion increases at the bases of the ulcers, and has demonstrated the capability of IPPG in the contactless and spatially resolved assessment of rhythmical blood volume changes in an ulcer. Verkruysse *et.al.* ^[37] have investigated IPPG can be useful for the characterization of vascular skin lesions after therapy.

Brain Function: A brain–computer interface (BCI) is a direct communication pathway between a brain and an external device ^[38]. A BCI transforms mental decision and reaction into control commands by analyzing the bioelectrical brain activity ^[39]. Electroencephalography (EEG) is the most studied potential non-invasive interface. But as well as the technology's susceptibility to electronic noise, the extensive training required before operation is another substantial barrier when using EEG as a BCI. IPPG has the capability of detecting the blood perfusion from the human forehead where information is contained about the neural system ^[40]. It is easily operated and insusceptible to electronic noise. All of the advantages lead to the possible application of IPPG in BCI. IPPG of brain function can help to elucidate the hemodynamic response to neuronal activity and thus lead to an understanding of the underlying mechanisms.

2.3 RESEARCH DIRECTION IN IMAGING PPG

The ideal IPPG system should make an accurate measurement of blood perfusion in any specific part of the body and for any subject regardless of physiology, state of health, and condition under which the measurement is made. For current IPPG, most published observations ^{[33][36][37]} are based on a qualitative nature of blood perfusion. The performance of IPPG is difficult to investigate in these measurements as it is difficult to determine experimentally the effect of changes in the optical properties of

segmented biological tissues on the output signals. Thus a representative model for the quantification of this effect is necessary to better understand the underlying principle of the IPPG signal and further improve the applicability of IPPG. As this effect is modulated by the light propagation in tissue, such a model needs to be on the basis of an accurate description of the light propagation in tissue.

This research aims to develop such an appropriate opto-physiological model to quantify IPPG signals with the optical properties of segmented tissues. The model is created by redefining the path length of the Beer-Lambert law through the outputs of the MC simulation on multi-layered tissue, and validated subsequently via correlation with corresponding real-life experiments. To this end, the model can contribute to quantifying the output signals of IPPG with the segmented optical properties of tissue, and then constructing the layered perfusion mapping of a designated tissue.

3. OPTO-PHYSIOLOGICAL MODEL

The objective of this chapter is to arrive at an opto-physiological model that can quantitatively describe the relationship between segmented optical properties of tissue and the IPPG signals.

The chapter begins by explaining of the optical and physiological phenomena that govern the light-tissue interaction in optical bio-monitoring techniques, revisits relevant engineering models currently used for *in-vivo* optical propagation, and finally creates an appropriate model to mathematically quantify the IPPG signal in a multi-layered format.

3.1 PRINCIPLES OF TISSUE OPTICS

Figure 3. 1 illustrates the situation how light may travel in tissue. The optical propagation in turbid biological media is jointly governed by the absorption and scattering properties of tissue. The vast majority of light follows a meandering trajectory in tissue due to scattering.

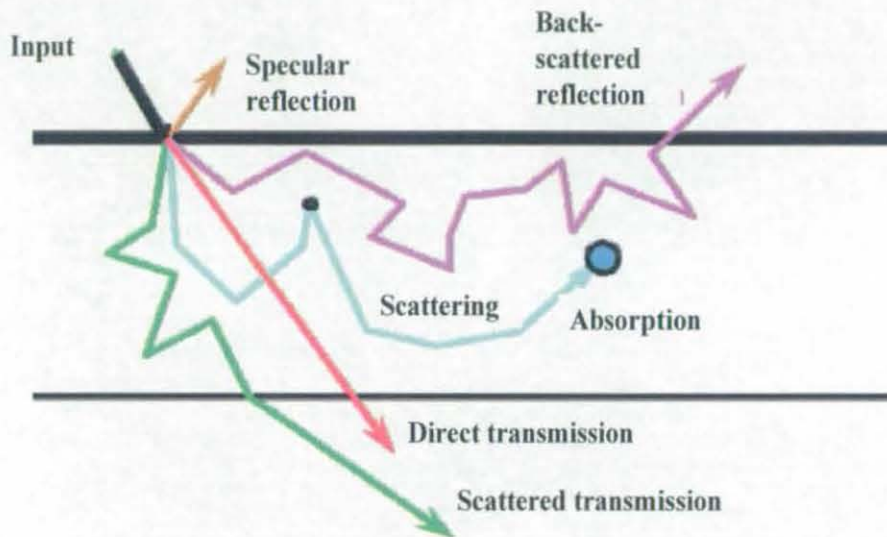


Figure 3. 1 The propagation paths of light in tissue.

The quantification of the optical propagation in tissue is a question of growing concern in many medical applications. Numerous models that predict fluence rates in tissue, or reflection and transmission of light by tissue have been developed. The accuracy of these models ultimately depends upon how well the optical properties of the tissue are known. Hence clearly understanding these optical properties will be of great help when creating an appropriate model for IPPG. This section reviews some key optical properties governing the behaviour of light propagating through an optically dense medium such as human skin.

3.1.1 Refraction

Refraction occurs under any circumstance where propagating light encounters a change in refractive index n as shown in Figure 3. 2. Surface effects due to index mismatched macroscopic boundaries such as those between tissue layers are one

such occurrence. Churmakov *et al.* ^[41] concluded that the spatial photon sensitivity profile which shows the photon density distribution under normal conditions was nearly identical to that achieved when disregarding total internal reflection at the boundary between a highly scattering and absorbing medium and vacuum. This conclusion proves the insignificance of this effect in this investigation. Furthermore, the refractive indices of most soft tissue types at a macroscopic scale are in the range of 1.38-1.41 ^[42], yielding inter-tissue boundary effects which are disregarded in most photon transport models ^{[20] [43]}.

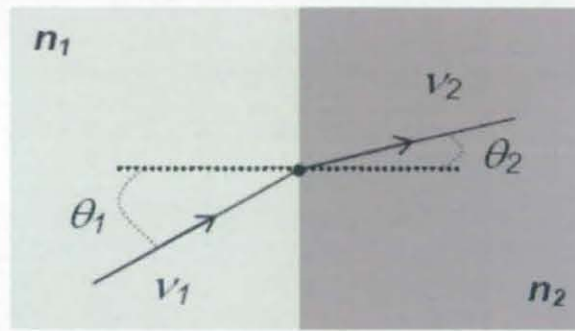


Figure 3. 2 Refraction of light between two media with different refractive index ($n_1 < n_2$), where θ_1 is the angle of incidence, θ_2 is the angle of refraction, and v_1 and v_2 are the speeds of light in each media.

3.1.2 Scattering

Refractive index mismatches within tissues also exist at a microscopic scale, where collagen fibres, blood vessels, cell membranes and organelles etc. submit light to refractive effects ^[44]. This microscopic refraction is called scattering, the effectiveness of which is described with scattering coefficient $\mu_s (mm^{-1})$. Scattering is a physical process by which light interacts with matter to change its direction, so if the medium is scattering, the path taken by the photons is no longer straight as shown in Figure 3. 3. The scattering of light through a medium has a straight effect on its distribution, thus making scattering a dominant effect in such studies.

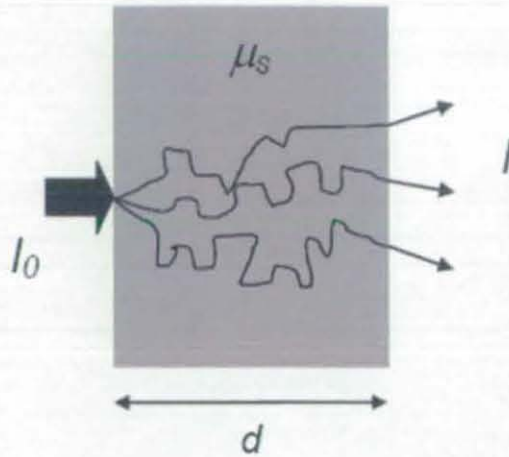


Figure 3. 3 Scattering of light through a scattering medium, where I is the intensity of the scattered transmitted light, I_0 is the incident light intensity, and μ_s is the scattering coefficient of the homogenous medium of thickness d .

In practice, most models approximate the scattering effects through the use of an experimentally determined scattering coefficient μ_s and an anisotropy factor g to describe tissue types at a macroscopic scale. $1/\mu_s$ is the mean free path (*mfp*, *mm*) between scattering events and g is the mean cosine of the scattering angle as shown in Figure 3. 4. An anisotropy factor g is used to describe the scattering anisotropy of a medium, where $g = 0$ represents isotropic scattering and $g = 1$ as scattering becomes more forward peaked. In the photon diffusion (PD) theory, the scattering effect is further approximated by using a reduced scattering coefficient μ'_s (mm^{-1}), which incorporates the scattering coefficient μ_s and the anisotropy g :

$$\mu'_s = \mu_s \times (1 - g) \quad [3. 1]$$

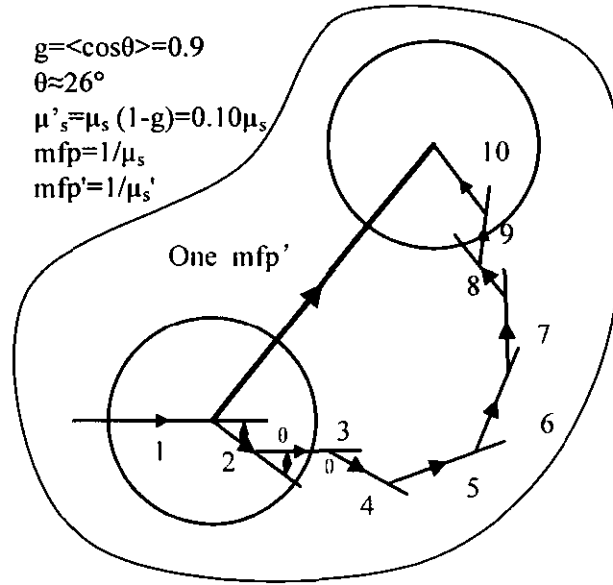


Figure 3. 4 A simple description of the scattering effect using μ_s , g , and μ'_s . mfp is the mean free path of each small step with anisotropic deflection angles θ , and mfp' is the equivalent reduced mean free path of one big step.

The scattering effect is determined by the ultra-structure of the tissue ^[45]. Tissue ultra-structure extends from membranes to membrane aggregates to collagen fibres to nuclei to cells. Light is most strongly scattered by those whose size matches the wavelength of light. In this research, the attention is focused on NIR spectral region. In this region, the structures of skin that contribute most to scattering such as collagen fibre bundles and red blood cells are considerably at least three times larger ^[46] than the NIR wavelength. Thus the scattering coefficient is expected to change slightly with the shift of wavelength.

3.1.3 Absorption

Absorption is an effect that is explained at an atomic scale as the conversion of photons into thermal energy upon collision with atoms. More specifically, this effect is most likely to occur when the energy of a photon (determined by its frequency) coincides with one of the excited states of the atom it is colliding with. Its direct relationship to the effective transmission of light through a medium makes this a key effect in the present study.

The absorption coefficient $\mu_a (mm^{-1})$ of a medium for a given wavelength λ describes the effectiveness of absorption as shown in Figure 3. 5 and it represents a probability per unit length of a photon being absorbed.

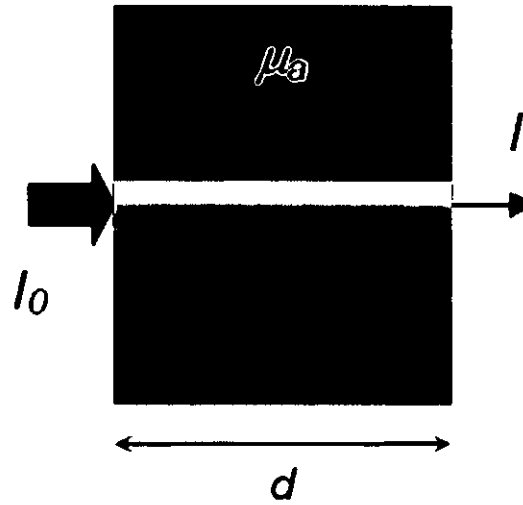


Figure 3. 5 Absorption of light through a non-scattering medium, where I is the intensity of the direct transmitted light, I_0 is the incident light intensity, and μ_a is the absorption coefficient of the homogenous medium of thickness d .

In tissue, the main absorbers of light in the NIR spectral region include oxygenated and deoxygenated haemoglobin. Each has its own particular absorption spectrum which describes the level of absorption at each wavelength ^[47]. The absorption spectra of the two absorbers have been previously presented in Figure 2. 9.

3.2 EXISTING MODELS OF LIGHT PROPAGATION

Optical bio-monitoring modalities can be described in general terms as systems that modify a specific light intensity, where the transfer function is determined by a number of anatomical and optical properties of biological tissues. Most biological tissue is a turbid medium with strong scattering; thus light follows a complicated path, the signal strength attenuates rapidly, and the propagation is inherently 3-D ^[48]. This makes the modelling of light propagation extremely difficult. A wide variety of linear and non-linear propagation models have been developed attempting to address the problem in conventional PPG, especially in pulse oximetry. Kubelka–Munk theory incorporated scattering in a heuristic approach to deriving optical density, and

was applied to *in-vitro* and *in-vivo* pulse oximetry ^[49]; however, its assumption of isotropic scattering was unrealistic. A highly accurate description of the physical system like the radiative transport equation (RTE) ^[50] incorporates anisotropic scattering more accurately reflecting the tissue characteristics, however the greatly increasing mathematic complexity with the tissue structure makes the application of this model extremely difficult in complicate description of tissue ^[43] ^[44] . An oversimplified format of the Beer-Lambert law, would, for example, disregard scattering effects within human tissue, thus tending to invalidate it as a representation of the system. The following section introduces three main models used for *in-vivo* optical propagation which lay the foundation of the opto-physiological model of IPPG.

3.2.1 Radiative Transport Theory

Propagation of light in tissue can, in principle, be described using fundamental electromagnetic theory. Based upon radiative transfer theory (RTT), the propagation can be simplified by only considering the flow of energy through the medium, which gives a very good approximation for large thicknesses (>several *mm*) of biological tissue in the NIR region. The following formulation of the radiative transport equation (RTE) considers monochromatic light and disregards polarisation ^[50]:

$$\frac{\partial I(\vec{r}, \vec{n})}{\partial \vec{n}} = -\mu_t I(\vec{r}, \vec{n}) + \frac{\mu_s}{4\pi} \int_{4\pi} I(\vec{r}, \vec{n}') P_d(\vec{r}, \vec{n}, \vec{n}') d\Omega' \quad [3. 2]$$

The left side of Equation [3. 2] represents the net change in energy due to energy flow, where $I(\vec{r}, \vec{n})$ is the radiance at a position \vec{r} in direction \vec{n} . The first term of the right side represents the radiance lost due to absorption and scattering, where $\mu_t = \mu_a + \mu_s$, μ_s is the scattering coefficient and μ_a is the absorption coefficient. The last term denotes the gain in $I(\vec{r}, \vec{n})$ per unit length in direction \vec{n} due to scattering from all other directions \vec{n}' . The light power per unit area confined within solid angle $d\Omega$ coming from direction \vec{n}' is $I(\vec{r}, \vec{n}') d\Omega'$ with scattering probability density function $P_d(\vec{r}, \vec{n}, \vec{n}')$ for scattering from \vec{n}' to direction \vec{n} . While exact solutions for the RTE

exist only for simple cases such as isotropic scattering in a simple geometry ^[50], there is no general solution. Therefore further approximations and computing numerical solutions have been developed.

3.2.1.1 Analytic approximation-photon diffusion model

The diffusion approximation, also known as photon diffusion (PD) model ^[51] assumes isotropic scattering through all media by using the reduced scattering coefficient μ'_s as Equation [3. 1]. Schmitt ^[52] derived approximate analytical solutions of PD theory based on a homogeneous tissue model for pulse oximetry. Marble *et al.* ^[53] found *in-vivo* results from the fingers of 50 health subjects for a transmission mode PPG sensor followed PD model predictions when considering the tissue as a slab medium. Takatani *et al.* ^[54] and Schmitt *et al.* ^[43] obtained the analytic PD solutions based on two- and three-layered tissue with simplifying assumptions. Until now only one tissue model up to four layers has been proposed by Van Gemert *et al.* ^[44] in studying laser dosimetry, but an analytic solution was not published. The greatly increasing mathematic complexity with the tissue structure makes the application of photon diffusion (PD) model extremely difficult in multi-layered tissue.

3.2.1.2 Numerical solution-Monte Carlo simulation

Monte Carlo (MC) simulation, a numerical solution to RTE as Equation [3. 2], refers to a technique first proposed by Metropolis and Ulam ^[55] to solve various physical problems using a statistical model based upon RTT. In case of the light-tissue interaction, the tissue can be generally considered as a strongly scattering turbid media, and the light injected into tissue undergoes events including absorption, scattering and reflection at the interface of different tissue layers. MC methods simulate the optical propagation process in turbid tissues at a macroscopic level and evaluate the multiple physical quantities simultaneously.

Inexpensive computing capability has removed a major obstacle to the successful use of MC methods. MC simulations offer a numerical modelling scheme that has shown good correlation with practical results in situations where an analytic solution is either unnecessary or impractical. The scheme can be conceptually applied to any

analytic theory and complex geometric configurations even heterogeneous media. Graaff *et al.* ^[56] employed MC simulations of light travelling through a homogeneous, single-layer tissue model to demonstrate the importance of light scattering in understanding reflectance pulse oximetry. Tuchin ^[48] used MC methods to solve the inverse problem of obtaining optical parameters from tissue samples based upon a five-layer model.

3.2.2 Beer-Lambert law

The Beer-Lambert law describes the effective optical absorbance of a medium when light travels through a given path length commonly employed in pulse oximetry ^[57] ^[58]. The degree of absorption depends on the nature of the trans-illuminated material and the wavelength of the illumination. Experimental measurements are usually made in terms of incident and transmitted light intensity in a transmission mode. Ignoring the light transmitted directly from the light source to the receiver or light which does not pass through arterially perfused tissue, the relationship between the incident and transmitted light is obtained from the Beer-Lambert law as:

$$I = I_0 \times \exp(-\mu_a \times l) \quad [3. 3]$$

where

I_0 incident light intensity

I transmitted light intensity

μ_a the wavelength-dependent absorption coefficient, mm^{-1}

l the path length, mm .

In the transmission mode, the Beer-Lambert law is normally simplified to regard the path length as the thickness of a medium and does not take scattering into account. Nonetheless, it yields the ratiometric approach to oxygen saturation calculation; empirical calibration removes the effects of other tissue characteristics as long as they remain close to their state at calibration. In the reflection mode, the simplification of the Beer-Lambert law is of limited accuracy and applicability, as the optical path is less well defined than that in the transmission mode, and may differ between two wavelengths.

3.2.3 Modified Beer-Lambert law

The Beer-Lambert law defines the absorbance A of tissue as the log to the base e of the ratio of the intensity of the incident light to the transmitted light:

$$A = -\ln\left(\frac{I_0}{I}\right) = \mu_a \times l \quad [3.4]$$

If scattering is present, the incident light is attenuated due to both scattering and absorption. Consequently, the overall attenuation, in optical density OD , can be expressed as the sum of the attenuation due to absorbance and scattering:

$$OD = A + B = \mu_a \times DP + B \quad [3.5]$$

where DP is the differential path length ^[59] depending upon both absorption and scattering coefficients, and B is a geometry-dependent factor, which is independent of absorption and represents attenuation caused by scattering. This equation is often referred to as the modified Beer-Lambert law ^[60]. The modified Beer-Lambert law has been widely applied in the near-infrared tissue spectroscopy to quantify the concentration changes of tissue chromophores, mainly oxy- and deoxyhaemoglobin ^{[61][62]}. Humphreys *et al.* also introduced the modified Beer-Lambert law into IPPG to calculate the oxygen saturation ^[34].

3.3 PROPRIETARY OPTO-PHYSIOLOGICAL MODEL

A linear increase in the accuracy of a model for light propagation in biological tissue results in an exponential increase in its complexity. The high computational cost of MC simulation as a numerical solution to RTE is a clear illustration of this. On the other hand, the simplification of the Beer-Lambert law normally disregards scattering. This research aims to create an accurate, yet applicable opto-physiological model to quantify the effect of the segmented optical properties of tissue on the blood perfusion, which is represented by the IPPG signal. To achieve both accurate and applicability, a simply representation with descriptive parameters is desired.

3.3.1 Opto-Physiological Modelling

The modified Beer-Lambert law demonstrates that a modification in pathlength can be used to take into account the effects of scattering and increase the accuracy of the model prediction. The modified Beer-Lambert law is usually applied to static homogeneous scattering media. In the model developed in this thesis, the tissue is treated as a multi-layered structure with respective dynamic blood volume changes, rather than a whole and static tissue. Such a model is named as the opto-physiological model, where ‘opto’ referring to the light-tissue interaction and ‘physiological’ indicating that the model is used to mathematically quantify the effect of segmented optical properties of tissue on the blood perfusion, represented by the IPPG signal. Following this idea, quantification of IPPG signals in such multi-layered tissue requires knowledge, or at least an estimate, of the optical path length in each layer.

To date, various methods have been proposed for analysing optical path length through tissue. In the application of the modified Beer-Lambert law, DP can be measured by using the time-resolved and intensity-modulated spectroscopy that determines the photon mean time-of-flight or the phase shift of an intensity modulated light wave^{[60][63]}. The complexity and the cost of these systems prohibit the implementation of these measurements in IPPG. Some continuous wave spectroscopic systems use some tabulated DP values^[64], but none of these values is specialised for segmented human skin. Another approach has been the MC method, which can be applied to an inhomogeneous medium and calculate the path length directly. Moreover, this method offers the chance to connect the optical path length with the various parts or segments of a biological tissue. This will help to quantify IPPG signals with segmented optical properties. Thus the MC method is selected to derive the optical path length of a multi-layered tissue in this investigation.

Following above, an opto-physiological modelling is employed to introduce scattering-related path length into the Beer-Lambert law. In this investigation, the path length named as mean path length (MPL) is derived from the output of the MC simulation based upon a multi-layered tissue model. The process of the opto-physiological modelling is illustrated in Figure 3. 6. MPL is yielded by the MC

simulation on a multi-layered tissue model with wavelength-dependent distinct optical properties and sensor parameters of the actual measurement such as the size and position of the light source and the detector. The opto-physiological model relying on *MPL* and the optical properties of tissue is derived following the formulation of the Beer-Lambert law. This model can be used to quantify the tissue absorbance and the IPPG signal.

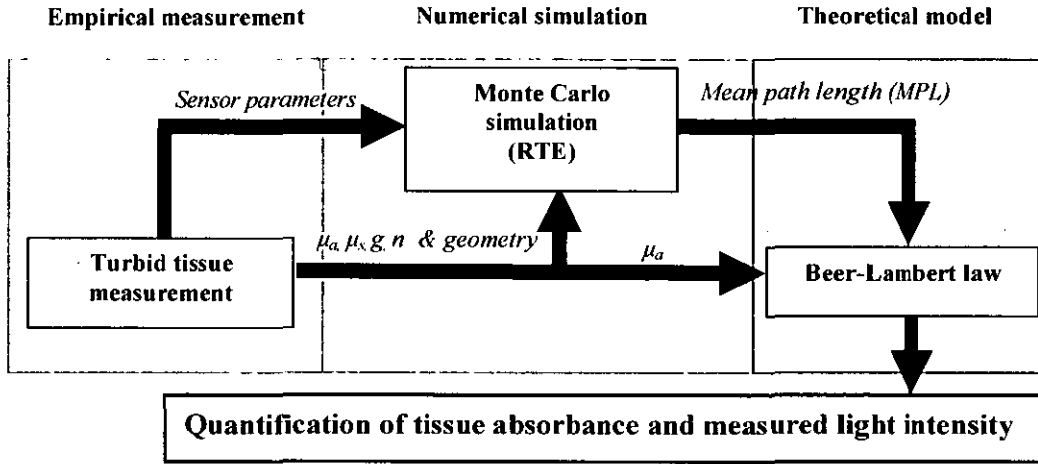


Figure 3. 6 A diagram of the opto-physiological modelling.

3.3.2 Revised Beer-Lambert Formulation

The path length in the Beer-Lambert law is redefined by *MPL*, a more descriptive characterisation of light-tissue interaction:

$$I = I_0 \times \exp(-\mu_a \times MPL) \quad [3. 6]$$

where

I_0 the incident light intensity

I the scattered light intensity

μ_a the wavelength-dependent absorption coefficient, mm^{-1}

MPL the mean path length, mm .

MPL, yielded by the MC simulation, takes account of anisotropic scattering, as well as the characteristics of the light source and the detector, and the geometry of tissue:

$$MPL = (Sen + Geo) \times l(\mu_a, \mu_s, g) \quad [3. 7]$$

where

- Sen* a factor that accounts for the sensor parameters in Figure 3. 6
- Geo* a factor that accounts for a specific tissue model including the geometry and the layered-interaction
- $l(\mu_a, \mu_s, g)$ the path length modulated by the wavelength-dependent absorption coefficient μ_a , scattering coefficient μ_s and the anisotropy factor g .

3.3.3 Resultant Formulation of Opto-physiological Model

As introduced in Chapter 2, the IPPG signal contains a dynamic component due to the pulsation of arterial blood, and a quasi-static component governed by the static part of tissue. The arterial blood volume changes upon each heart beat resulting in the dynamic path length, $MPL_{dynamic}$. This allows the dynamic component to be expressed separately from the static component.

The revised Beer-Lambert formulation can then be derived as:

$$I = I_0 \times \exp[-(\mu_{a,static} \times MPL_{static} + \mu_{a,blood} \times MPL_{dynamic})] \quad [3. 8]$$

where

- $\mu_{a,static}$ the wavelength-dependent absorption coefficient of the static component of tissue, mm^{-1}
- $\mu_{a,blood}$ the wavelength-dependent absorption coefficient of arterial blood, mm^{-1}
- MPL_{static} the static component of MPL , mm
- $MPL_{dynamic}$ the dynamic component of MPL , mm .

Separating the static and the dynamic component, Equation [3. 8] can be expressed as:

$$I = I_{static} \times \exp(-\mu_{a,blood} \times MPL_{dynamic}) \quad [3. 9]$$

where

$$I_{static} = I_0 \times \exp(-\mu_{a,static} \times MPL_{static}) \quad [3. 10]$$

The dynamic component of the absorption accounts for only a few percent about 0.1-2% ^[18] of the total absorption, i.e. the exponent of the second part in Equation [3. 9] is very small. The approximation in mathematics:

$$\exp(x) = 1 + x \quad \text{for } |x| \ll 1 \quad [3. 11]$$

can be applied to Equation [3. 9] as:

$$I = I_{static} \times (1 - \mu_{a,blood} \times MPL_{dynamic}) \quad [3. 12]$$

This light intensity can easily be broken down into two components, a time-independent I_{static} :

$$I_{static} = I_0 \times \exp(-\mu_{a,static} \times MPL_{static}) \quad [3. 13]$$

and a time-variant $I_{dynamic}$:

$$I_{dynamic} = I_{static} \times \mu_{a,blood} \times MPL_{dynamic} \quad [3. 14]$$

Following Equation [3. 13] and [3. 14], the dynamic component can be further separated from the static component by normalisation as:

$$I_{perfusion} = \frac{I_{dynamic}}{I_{static}} = \frac{I_{static} \times \mu_{a,blood} \times MPL_{dynamic}}{I_{static}} = \mu_{a,blood} \times MPL_{dynamic} \quad [3. 15]$$

where $I_{perfusion}$ refers to the normalised intensity of the dynamic component, which represents the blood perfusion of tissue.

Equation [3. 15] is the general formulas of the blood perfusion in the opto-physiological model, which can be extended into a multi-layered format.

3.3.4 Extended Opto-physiological Model

3.3.4.1 Description of Multi-layered tissue

To extend the opto-physiological model into a multi-layered format, the tissue is treated as a composite medium $M=\{m(1), m(2) \dots m(k)\}$ composed of k -layer media ($k=1,2 \dots$). $MPL(i)$ is the mean path length for each layer $m(i)$. Each layer is defined by a set of optical coefficients such as μ_a , μ_s , g , n and the geometry such as the thickness d .

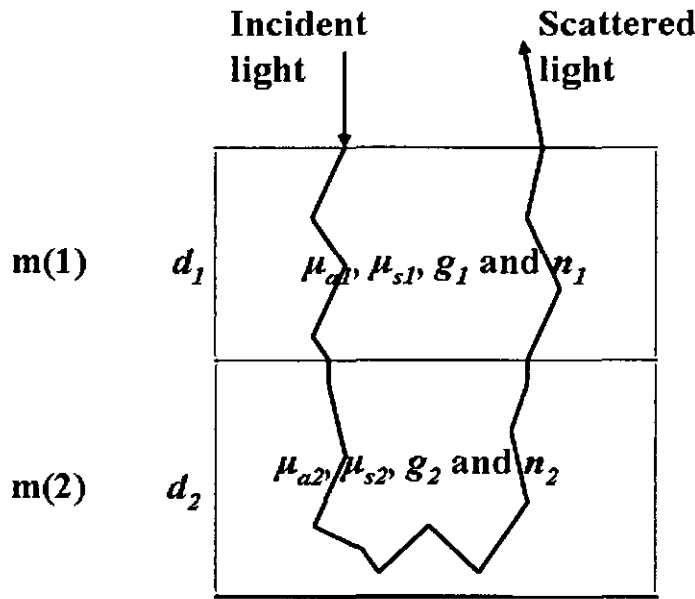


Figure 3.7 A diagram of a two-layered tissue $M=\{m(1), m(2)\}$.

This treatment of a tissue is in line with previous research ^{[43] [54]}, which facilitates the quantitatively description of the relationship between the segmented optical properties and the IPPG signal.

3.3.4.2 Multi-layered absorbance

For such a given IPPG system composed of k -layered optical media ($k=1, 2 \dots$), every medium $m(i)$ experiences a $MPL(i)$ that translates to absorbance according to the absorption coefficient $\mu_a(i)$ of the medium:

$$A(i) = \mu_a(i) \times MPL(i) \quad [3. 16]$$

Following Equation [3. 16], the system absorbance of light through the k -layered media can be derived as:

$$A = \sum_{i=1}^k A(i) = \sum_{i=1}^k [\mu_a(i) \times MPL(i)] \quad [3. 17]$$

3.3.4.3 Multi-layered blood perfusion

The static light intensity of multi-layered tissue can be expressed as the product of the steady absorption from individual layers following Equation [3. 13]:

$$I_{static} = I_0 \times \exp(-\mu_{a,static} \times MPL_{static}) = I_0 \times \prod_{i=1}^k [\exp(-\mu_{a,static}(i) \times MPL_{static}(i))] \quad [3. 18]$$

where

- $\mu_{a,static}(i)$ the wavelength-dependent absorption coefficient of the static component from layer i , mm^{-1}
- $MPL_{static}(i)$ the static component of MPL of layer i , mm .

The blood perfusion of multi-layered tissue can be expressed as the sum of the dynamic absorption of individual layers following Equation [3. 15]:

$$I_{perfusion} = \mu_{a,blood} \times MPL_{dynamic} = \sum_{i=1}^k [\mu_{a,blood}(i) \times MPL_{dynamic}(i)] \quad [3. 19]$$

where

- $\mu_{a,blood}(i)$ the wavelength-dependent absorption coefficient of the arterial blood from layer i , mm^{-1}
- $MPL_{dynamic}(i)$ the dynamic component of MPL from layer i .

3.3.4.3 Specific-layered blood perfusion

Consequently, the static component of a specific layer i can be derived with its weight $w_{static}(i)$ and the total static component following Equation [3. 18] as:

$$\begin{aligned}
 I_{static}(i) &= I_{static} \times w_{static}(i) = I_{static} \times \frac{\exp(-\mu_{a,static}(i, \lambda) \times MPL_{static}(i))}{\prod_k \exp(-\mu_{a,static}(k, \lambda) \times MPL_{static}(k))} \\
 &= I_{static} \times \frac{1}{\prod_{i' \neq i} \exp(-\mu_{a,static}(i', \lambda) \times MPL'_{static}(i'))}
 \end{aligned} \tag{3. 20}$$

Similarly, the perfusion $I_{perfusion}(i)$ of a specific layer i can be expressed as the product of the total perfusion and $w_{perfusion}(i)$ following Equation [3. 19]:

$$\begin{aligned}
 I_{perfusion}(i) &= I_{perfusion} \times w_{perfusion}(i) = I_{perfusion} \times \frac{\mu_{a,blood}(i, \lambda) \times MPL_{dynamic}(i)}{\sum_k \mu_{a,blood}(k, \lambda) \times MPL_{dynamic}(k)} \\
 &= I_{perfusion} \times \frac{MPL_{dynamic}(i)}{\sum_k MPL_{dynamic}(k)}
 \end{aligned} \tag{3. 21}$$

3.3.5 The applicability of Opto-physiological model

3.3.5.1 Detector-dependent opto-physiological model

Equation [3. 6] is the fundamental formula of the opto-physiological model assuming an infinite detector which collects all the scattered light. If considering finite size of detector in reality, even with $\mu_a=0$, there is attenuation because of the scattering of light away from the detector. Thus the light I_s arriving at the detector when $\mu_a=0$ is introduced into Equation [3. 6] as:

$$I' = I_s \times \exp(-\mu_a \times MPL') \tag{3. 22}$$

where I' is the detector-dependent scattered light intensity and MPL' is the detector-dependent mean path length.

Thus the detector-dependent static component I'_{static} is derived following Equation [3. 13] as:

$$I'_{static} = I_s \times \exp(-\mu_{a,static} \times MP'_{static}) \tag{3. 23}$$

and the detector-dependent dynamic component $I'_{perfusion}$ following Equation [3. 15] as:

$$I'_{perfusion} = \frac{I'_{dynamic}}{I'_{static}} = \mu_{a,blood} \times MPL'_{dynamic} \quad [3.24]$$

Following Equation [3.17], the detector-dependent absorbance A' of light through the k -layered media can be derived as:

$$A' = \sum_{i=1}^k [\mu_a(i) \times MPL'(i)] \quad [3.25]$$

Equation [3.18] [3.19] [3.20] and [3.21] are revised according to Equation [3.23] and [3.24] as:

$$I'_{static} = I_s \times \prod_{i=1}^k [\exp(-\mu_{a,static}(i) \times MPL'_{static}(i))] \quad [3.26]$$

$$I'_{perfusion} = \sum_{i=1}^k [\mu_{a,blood}(i) \times MPL'_{dynamic}(i)] \quad [3.27]$$

$$I'_{static}(i) = I'_{static} \times w_{static}(i) = I'_{static} \times \frac{1}{\prod_{i' \neq i} \exp(-\mu_{a,static}(i', \lambda) \times MPL'_{static}(i'))} \quad [3.28]$$

$$I'_{perfusion}(i) = I'_{perfusion} \times w_{perfusion}(i) = I'_{perfusion} \times \frac{MPL'_{dynamic}(i)}{\sum_k MPL'_{dynamic}(k)} \quad [3.29]$$

3.3.5.2 Transmission mode and reflection mode

The opto-physiological model can be applied in both transmission mode and reflection mode. In transmission-model IPPG, MPL is largely dependent on the geometry and the layered-interaction of tissue model, rather than the characteristics of the light source and the detector. In reflection-mode IPPG, the characteristics of the light source and detector, especially the distance and size^[43], are crucial factors in determining MPL . It should be noted that the surface reflection can not be disregarded in reflection-mode IPPG, especially in remote-capturing configurations.

4. MONTE-CARLO SIMULATION

The opto-physiological model of IPPG relies on the output of the MC simulation. The objectives of this chapter are to build up a MC simulation platform as a virtual environment to describe the light propagation in multi-layered tissue and to yield the key parameter *MPL* for the opto-physiological model.

The main procedures of the MC simulation include three stages: the model preparation to export a constructed anatomical tissue model, the MC ray tracing to output the coordinates of traced ray vertices from the tissue model, and the post data processing to generate *MPLs*.

4.1 SIMULATION OVERVIEW

The MC simulation of this research offers a flexible, yet rigorous approach to photon transport in turbid tissue. The simulation aims to provide a detailed description of the light propagation in a multi-layered tissue with dynamic blood volume changes in a virtual environment.

The platform utilises two commercially available software packages (OptiCAD and MATLAB), and can be sectioned into several phases of operation: model preparation, simulation and post-processing. OptiCAD was selected by virtue of its being one of the only available software platforms capable of performing MC simulations of optical propagation in arbitrary geometries. The software offers a direct perception how rays travel in tissue. Moreover, the basic unit for each ray can be directly related to the path length which makes the calculation of *MPL* much easier and more straightforward. MATLAB was chosen as a highly efficient development language for data processing algorithms.

The main procedures of the MC simulation are shown in Figure 4. 1. Model preparation was performed in MATLAB (Mathworks Co., USA) using “STL” function to export the 3-D CAD data of a constructed anatomical tissue model into OptiCAD. The main process of MC ray tracing was performed by OptiCAD (OptiCad Co., USA), which outputs the coordinates of traced ray vertices from the tissue model onto a file. Post data processing was performed in MATLAB through the use of custom algorithms specific to the outputs of the previous phases.

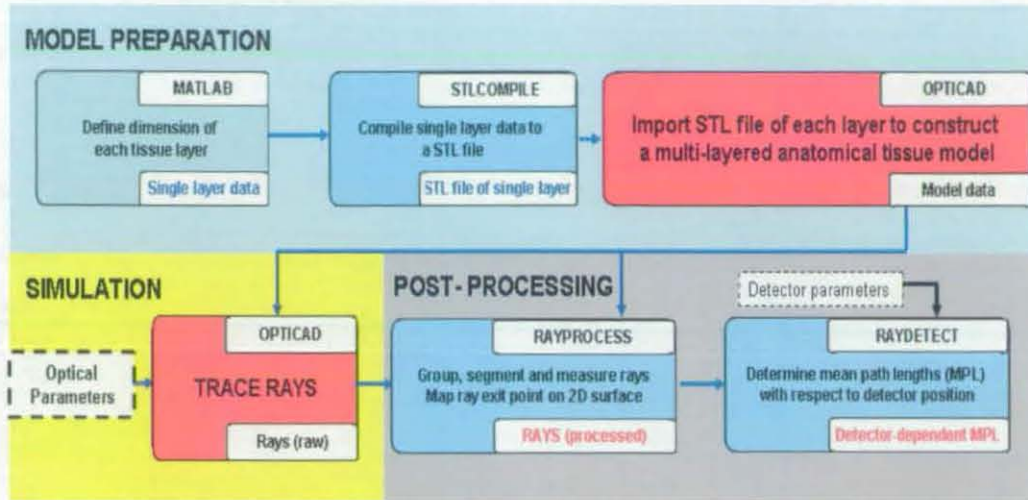


Figure 4. 1 The block diagram of MC ray-tracing platform where MATLAB functions are labelled in blue blocks and OPTICAD in red blocks.

Results of the MC simulation from OptiCAD and post-processing were utilised solely for the generation of *MPL* in the opto-physiological model. The following assumptions determine how MC ray-tracing and subsequent post-processing is performed:

- Time varying physiological components lead to changes in absorption and scattering, but not in tissue geometry. As introduced in Chapter 2, a skin vascular bed contains only a small amount of blood about 2-5% and the blood experiences only a volumetric change about 5% percent with the cardio-vascular pulse wave ^{[19] [20]}. Thus the small amount of the pulsatile blood brings insignificant change in the macroscopic geometry of the whole tissue.
- Differences between indices of refraction of tissue layers are considered negligible as introduced in section 3.1.1 that inter-tissue boundary effects are disregarded in most photon transport models ^{[20] [43]}.

The first assumption entails the use of time-varying absorption and scattering coefficients. For the second assumption, the only macroscopic index mismatch that is considered in the model is that found in the outermost surface of the measuring site.

4.2 TISSUE MODEL PREPARATION

A tissue model of complexity sufficient to approximate mammalian skin tissue requires multiple layers with distinct optical properties.

4.2.1 Model Structure

MPL is defined in Equation [3. 7] taking account of optical properties, as well as the geometry of tissue *Geo* and the characteristics of the light source and the detector *Sen*. *Geo* is a factor that accounts for a specific tissue model including the geometry and the layered-interaction, which is defined in the tissue model such as the arrangement of layers and the thickness of each layer.

In the general tissue model as shown in Figure 4. 2, a Cartesian coordinate system was used to define the model geometry *Geo* and trace photon movement. The origin of the coordinate system was the centre of model surface; the z-axis was the normal of the surface pointing toward the inside of the model; and the xy-plane was therefore on the model surface. Geometrical symmetry was assumed, and the tissue was defined by the specific size in xy-plane and finite thickness *d* along the z-axis.

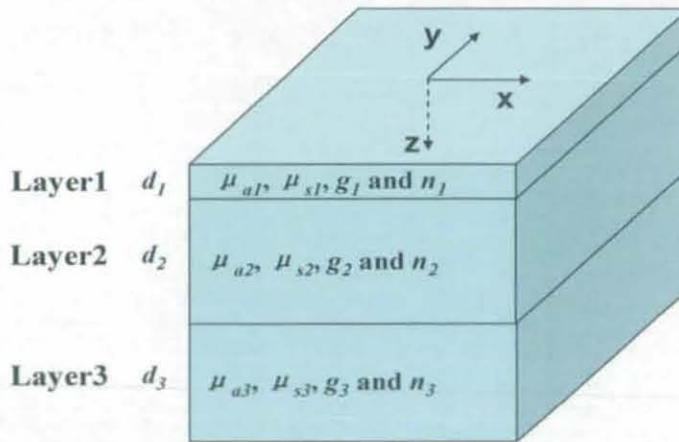


Figure 4. 2 A diagram of a general tissue model with three layers.

In the current model, all the layers were assumed to be homogeneous, and each layer was characterised by a bulk absorption coefficient μ_a , scattering coefficient μ_s , anisotropy factor g and refractive index n . Contrary to this assumption, the layers that make up tissue are neither homogeneous nor well-defined and planar. Nonetheless,

results of a previous study ^[65] indicate that the optical properties of whole tissue samples and tissue homogenates are similar. Therefore the model abstractions seem justified when the source and the detector apertures cover a large enough area of the tissue surface that small inhomogeneities do not substantially affect the final measurements.

4.2.2 Choice of Optical Properties

The light propagation in turbid biological media is jointly governed by the absorption and scattering properties of tissue. Most of these properties are wavelength-dependent. In simulation, the effect of illumination at different wavelength on light propagation is reflected by setting different optical properties such as μ_a and μ_s with the changes of wavelength.

Absorption and scattering of NIR light in tissues depend on numerous components of tissue, including pigmentation, blood content, and the size, shape, and distribution of collagen fibres that give tissue its structural integrity. The values of the absorption and scattering coefficients of biological tissues have been reported in previous literature ^{[66] [67] [68]}. Lack of agreement among experimental values obtained by different investigators for similar types of tissue is a consequence of inherent biological variability as well as of differences in measurement techniques and tissue preparation methods.

For the MC simulation in this research, the tissue was treated as a mixture of components, such as bloodless tissue and whole blood. Thus the absorption and scattering coefficient was calculated as a linear combination of the coefficients of each component weighted by its respective fraction:

$$\mu_a = \sum_j (f_j \times \mu_{a,j}) \quad [4.1]$$

$$\mu_s = \sum_j (f_j \times \mu_{s,j}) \quad [4.2]$$

where

f_j the volume fraction of component j

$\mu_{a,j}$ the absorption coefficient of component j , mm^{-1}

$\mu_{s,j}$ the scattering coefficient of component j , mm^{-1}

4.3 RAY-TRACING SETTINGS

OptiCAD treats the imported components of the 3-D model as solids and allows the volumetric optical properties of each to be computed from Equation [4. 1] and [4. 2]. The scattering coefficient μ_s together with anisotropy factor g was used rather than approximately reduced scattering coefficient μ'_s in order to increase the accuracy, and rays were traced using Cartesian coordinate to locate the position of each step.

Simulations were configured in accordance to the simplifying assumptions. Internal reflection and refraction between interfaces were disregarded, with the exception of the refraction between epidermis and air. Apart from yielding an intrinsic reduction in ray tracing times, this ensured minimisation of inaccuracies due to the inherently difficult task of modelling the microscopic textures of interfaces, which would otherwise pose a significant level of complexity in contrast to their minor contribution to the output.

The sensor parameters Sen in Equation [3. 7] account for the position and size of the light source and detector. For the illumination, all ray traces were performed using multiple spherical light sources with defined view angles. This approach was used as a simplification to the illumination covering the whole tissue surface to simulate the actual configuration in IPPG. The total output power of light source was set to be 1, and the threshold for traced ray setting was set to be 0.001% of ray's incident energy. A lens with the defined aperture was positioned over the tissue model to collect rays. The user interface of OptiCAD is presented in Appendix I.

4.4 POST DATA PROCESSING

Several algorithms were made into functions for the processing and analysis of output data from OptiCAD, all of which have been optimised in terms of speed, memory usage and data pipelining capability. Pipelining was achieved by

Ray2Mat.m function reads raw OptiCAD ray tracing data, splits it into full subsets of rays, and compresses the data into multiple files ready to be read by subsequent algorithms.

The function *RayProcess.m* removes unwanted rays, delimits rays with respect to vertices and segments, labels ray segments by layer, and measures segment path lengths as shown in Figure 4. 4.

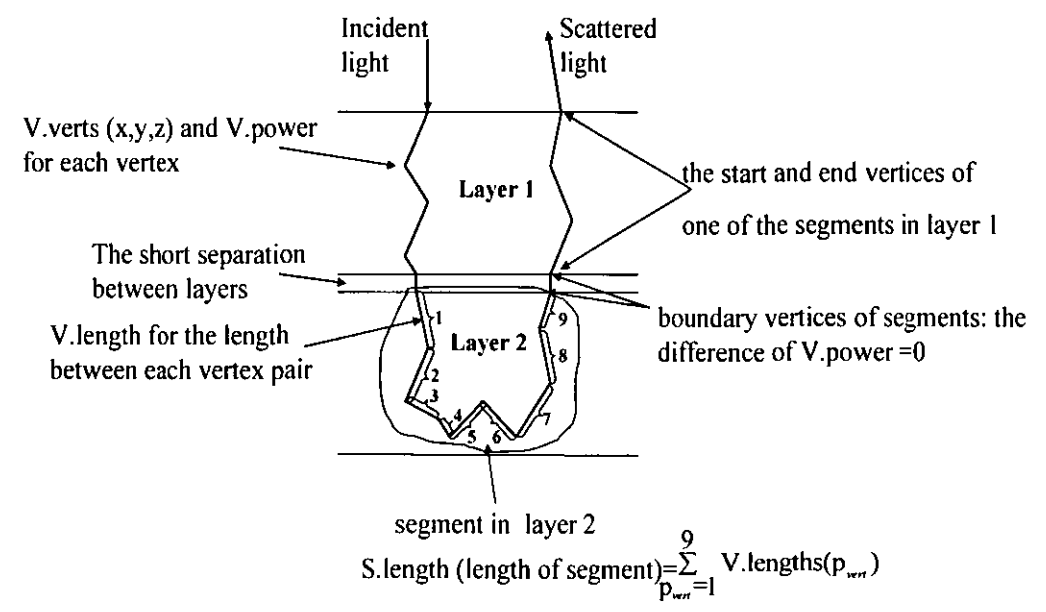


Figure 4. 4 An example of the *RayProcess.m* function to process a single ray in a two-layered tissue model.

The *RayProcess.m* function divides the ray tracing data into data structures (*Ray*, *V*, *S*), which group relevant ray data in terms of the ray, vertex, segment. The ray structure *Ray* stores the sum total of rays waiting to be processed. The components of the vertex structure *V* are all as long as the sum total of vertices for all stored rays. In the context of simulation, a ray segment refers to the portion of a ray within a single layer of the model. Thus, the components of the segment structure *S* are all as long as sum total of segments for all stored rays. Segments are delimited through the use of *V.powers*, where the vertices at which the difference of *V.powers*=0 are the boundary vertices. This effect was due to the finite separation that OptiCAD required between layers of the model, which results in the generation of short ray sub-segments connecting model layers during ray tracing.

Segment lengths are determined in two steps:

In the vertex domain,

$$V.lengths(p_{vert}) = |V.vertices(p_{vert}) - V.vertices(p_{vert} - 1)| \quad [4.3]$$

where p_{vert} is the vertex pointer.

In the segment domain:

$$S.lengths(p_{seg}) = \sum_{p_{vert} \in S.vgroups(s,1)}^{S.vgroups(s,2)} V.lengths(p_{vert}) \quad [4.4]$$

where p_{seg} is the segment pointer.

RayDetect.m is used to store the rays within the designated detector and generate *MPL'* for the defined detector position in Equation [3. 22]. This process is the final stage in the post processing, and as such consists of the defining detector structure *D* and the global data structure *G* containing data pertaining to the complete set of the MC data, such as *MPL'*.

The detector-dependent *MPL'* is yielded as follows: First, segment path lengths are accumulated for every layer for the stored rays according to detector position as:

$$G.Det(i, x, y, o) = \sum_{S_{sel}} S.lengths \quad [4.5]$$

where S_{sel} contains pointers to all segments within layer i for all ray ends within the detector area, and the detector area is defined by the size $x \times y$ and the centre o .

It follows that

$$G.MPL'(i, x, y, o) = G.Det(i, x, y, o) / G.Detnrays(x, y, o) \quad [4.6]$$

where $G.Detnrays(x, y, o)$ is the number of rays in $S_{sel}(x, y, o)$.

$G.MPL'(i, x, y, o)$ serves as the fully processed core data *MPL'* in Equation [3. 25] to be used for the quantification of absorbance A based upon the opto-physiological model.

When considering tissue with dynamic blood volume changes, the arterial pulsation is simulated by adding the pulsatile blood into the non-pulsatile tissue and thus changing the volume fraction of each component in tissue. So the scattering and absorption properties of tissue are changed in the non-pulsatile and pulsatile stage following Equation [4. 1] and [4. 2], which affects the light propagation in tissue and thus the MPL' in each stage. This simulation procedure is in accordance with the separation of the static and dynamic component in Equation [3. 13] and [3. 14]. Consequently, $MPL'_{dynamic}$ is calculated as:

$$G.MPL'_{dynamic} = G.MPL'_{pulsatile} - G.MPL'_{non-pulsatile} \quad [4. 7]$$

where $G.MPL_{non-pulsatile}$ is derived following Equation [4. 3] to [4. 6] from the simulations based upon the tissue model with non-pulsatile optical properties, and $G.MPL_{pulsatile}$ based upon the tissue model with pulsatile properties.

5. VALIDATION PLATFORM

The opto-physiological model is generated based upon the Beer-Lambert law and the MC simulation on multi-layered tissue. To validate the model, a reflection-mode IPPG setup and a series of *in-vitro* and *in-vivo* experimental protocols are developed. The experimental outputs serve as reference for the validation of the opto-physiological model.

The objectives of this chapter are to build up the experimental platform, define the validation procedure, and finally build up the mapping function of blood perfusion.

5.1 IMAGING PPG SYSTEM

The basic concept of IPPG is to illuminate the tissue with an array of light sources and to detect the light leaving the tissue with multiple detectors. The introduction of the fast digital camera facilitates the development of the concept to allow non-contact monitoring from a large field of view by applying illumination covering a large area as shown in Figure 5. 1. The basic elements in the current IPPG system including the ringlight illuminating a large area, the lens and the CCD sensor as the detector, and the skin tissue defined by optical coefficients and its geometry. In this investigation, a reflection-mode IPPG setup was built up for the validation experiment.

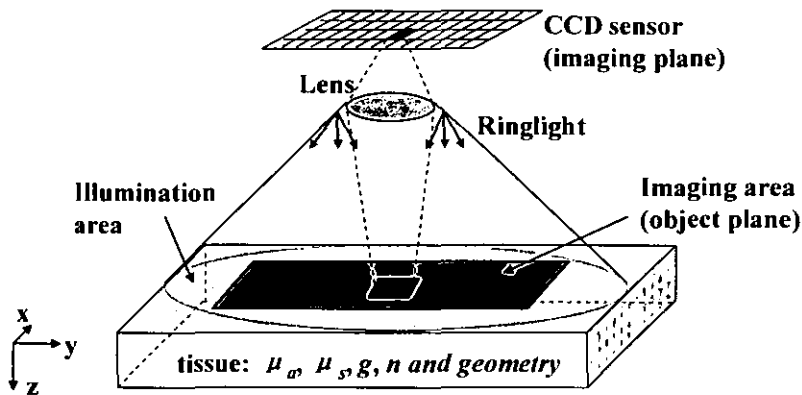


Figure 5. 1 The schematic diagram of IPPG setup including the ringlight, lens, CCD sensor and skin tissue.

5.1.1 Engineering Setup

5.1.1.1 Imaging Hardware

The key part of IPPG is a camera to collect the transmitted photons coming from tissue. The camera requirements should include the flexibility to choose variable readout speed, sensitivity and exposure time. CCD and CMOS cameras are currently in wide applications of biomedical research. The CCD camera creates high-quality and low-noise images, while it consumes more power and is more expensive. The CMOS camera is susceptible to noise, yet capable of reaching higher frame rates.

In this investigation, both camera solutions by virtue of each were selected as the imaging hardware.

A. Mikrotron CMOS camera

The Mikrotron camera (MC1311, Mikrotron GmbH, Germany) has a CMOS sensor with dimension $15.36 \times 12.29 \text{ mm}^2$. The sensor has a maximum resolution of 1280×1024 pixels with square pixels measuring $12 \mu\text{m}$. The pixels are encoded in 10 bits, making it eligible to detect the weak arterial pulsation. The camera was connected to a personal computer (PC) via a Camera Link® frame grabber PCI card (Inspecta-5, Mikrotron GmbH). With the custom image capture and control software developed in LabVIEW (National Instruments Co., USA), the camera can deliver quality images, and the frame rate can be as high as 32 fps in a full resolution and up to 4852 fps using a region of interest (ROI) mode. The system used an industry-standard C-Mount zoom lens (Focal length: 8mm, F/#: 1.4, M0814-MP, Computar, Japan). Depending upon the lens, it is possible to observe arbitrary parts of tissue, from a few square millimetres to several square centimetres as requested in the actual measurement.

B. Hamamatsu CCD camera

The CCD camera (C10000-201, Hamamatsu, Japan) has a maximum resolution of 2048×128 pixels. The pixels are encoded in 12 bits, providing a high digitization resolution, i.e. 4096 intensity levels. The CCD camera was connected to a PC via the same frame grabber card as the CMOS camera and the streamed frames were recorded in the custom image capture and control software in LabVIEW. An industry-standard F-Mount zoom lens (focal length: 50mm, f/#=1.8, AF Nikkor, Japan) was attached to the camera. The CCD camera has a much narrower capturing window. This limits its application in *in-vivo* measurements, as a large captured area is always desired to facilitate the comparison between different compartments of tissue. Nevertheless, the CCD camera has a much better spectra response as shown in Figure 5. 2 and a higher dynamic range when compared with the Mikrotron CMOS camera. Better digitisation resolution can greatly increases the quality of the detected signal, which directly affects the accuracy of the validation.

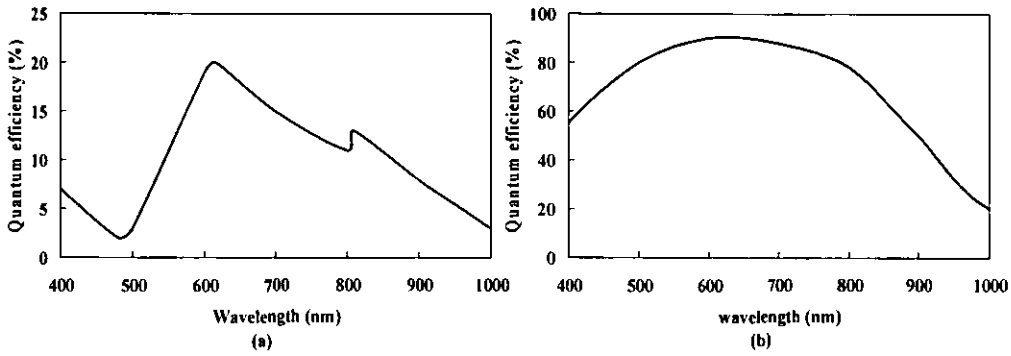


Figure 5.2 (a) The spectral response of the CMOS camera; (b) The spectral response of the CCD camera.

5.1.1.2 Illumination Configuration

A. Illumination source

The light-emitting diode (LED) has been used as the illumination source for the PPG-based instrumentation. However the LED does have some disadvantages, which could reduce the accuracy of detecting signals and the model prediction:

- The LED is not strictly monochromatic so that the optical properties such as μ_a and μ_s can not be estimated accurately based on the peak wavelength;
- The peak wavelength of the LED shifts over extended operation caused by the high temperature;
- Owing to the production spreads, there is a variation in the peak wavelength of different diodes up to 15nm ^[69].

To overcome these disadvantages of LED, resonant cavity light-emitting diode (RCLED) was introduced as the illumination source of the custom IPPG platform. The RCLED is a kind of high-speed LED which has been employed as potential light sources for several optoelectronic applications, such as optical communication systems and optical interconnections. RCLED retains the non-coherent characteristics of LED, but has a narrower spectral bandwidth which can help the estimation of the optical properties with a smaller deviation. Also it has good temperature stability proving superior to conventional LED ^[70]. All those advantages

brings benefits in the acquisition of better signal to noise ratio (SNR) and hence increasing the reliability of the output signal of IPPG.

B. Optical outline

The illuminator is expected to be the ring light, which can distribute the light over a large area of tissue. The ideal position of the ring light is around the camera lens, thus a hole the same size as the camera lens is required in the middle of the ring light as illustrated in Figure 5. 3.



Figure 5. 3 The position of the ringlight with lens in the middle.

The ringlight arrangement shown in Figure 5. 3 with a large hole in the centre results in a non uniform light distribution. Thus a parabolic reflector with multiple LEDs facing backwards towards the reflector was employed to compensate the shadow and collimate the light from multiple RCLEDs. This configuration is simulated in OptiCAD as shown in Figure 5. 4.

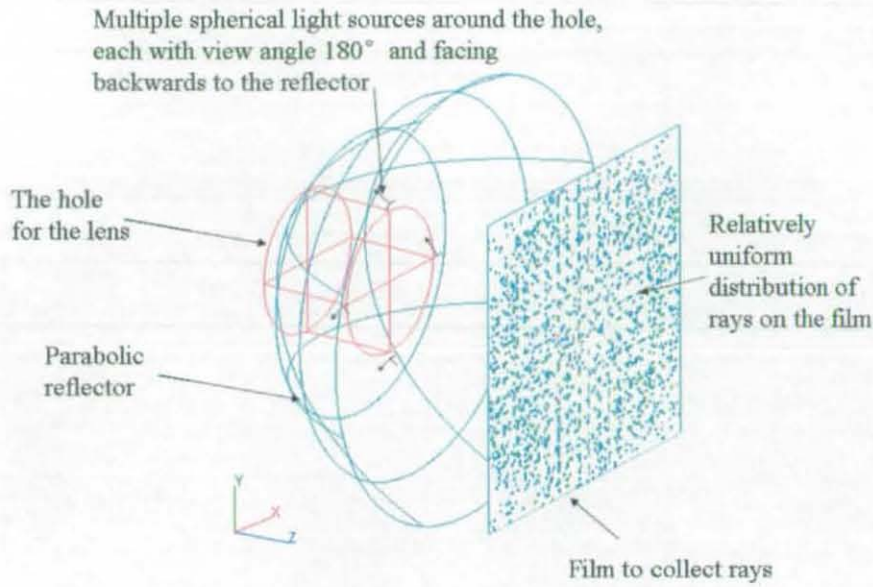


Figure 5. 4 A screen shot of the illumination configuration simulated in OptiCAD. Four spherical light sources are designed to simulate multiple RCLEDs, each with 180° view angle and facing backwards towards the reflector. The parabolic reflector is designed with a hole in the middle same size as the lens. A film with size of 100×100 mm is designed to collect the rays represented by the dots on it.

Figure 5. 4 illustrates the rays on the film relatively uniform distribute all over the detection area. Following this configuration, a custom dual-wavelength RCLED ring light with a parabolic reflector (B&Q, UK) was built up to provide an relatively uniform illumination covering the measurement site. The reflector was mounted around the camera lens (the CMOS camera: DIA, 14cm, depth: 5cm & the CCD camera: DIA: 18cm, depth: 6.5cm). The ring light consisted of 20 RCLEDs —10 with a peak wavelength of 650 nm and spectral bandwidth 30nm (TRC650SMD0603, WelTek Co. Ltd., Taiwan), and 10 with a peak wavelength of 870 nm and spectral bandwidth 20nm (TRC870SMD0603, WelTek Co. Ltd., Taiwan). The arrangement of the 650 and 870 nm RCLEDs is depicted in Figure 5. 5.

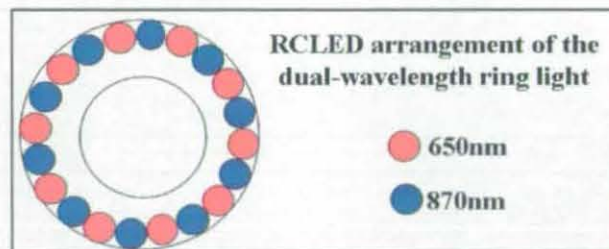


Figure 5. 5 The arrangement of dual-wavelength RCLED ringlight.

5.1.1.3 Control layout

A control circuit with a microcontroller (PIC16F876A, MicroChip Inc., USA) was configured to operate in 2 modes which can be manually selected according to the experimental requirement. The relative timing of the 2 modes is illustrated in Figure 5. 6. In this investigation, mode I was configured to be continuous illumination of single wavelength and mode II was to be alternative illumination of two wavelengths. The circuitry was triggered by the 'frame valid' signal from the camera, which indicates the period of exposure of each frame.

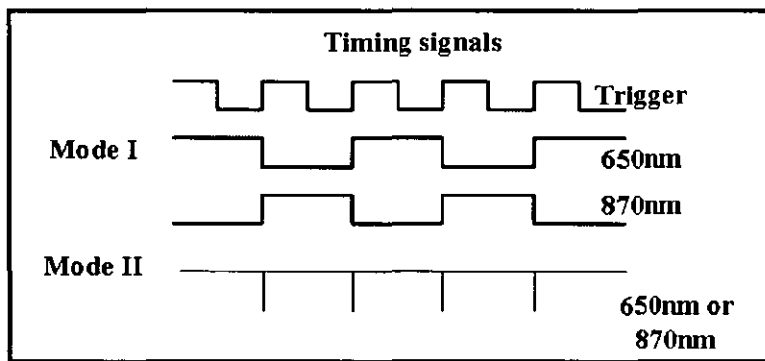


Figure 5. 6 The relative timing of the signal.

The captured frames from the camera were directly streamed into the PC via the frame grabber. The custom LabVIEW control software was developed to control frame grabber, change camera settings, acquire the images in on-line mode and load them for off-line processing. By changing the readout speed and the exposure time, the sample rate can be adjusted to meet requirements. The custom LabVIEW control software is detailed in Appendix II.

5.1.2 Post Signal Processing

The outputs of the camera were a set of raw frames containing the information of the detected light intensity. Post signal processing of these raw frames was performed to yield discrete values of detected light intensity for a designated ROI_{ip} which represents the ROI in the imaging plane as illustrated in Figure 5. 1. The processing follows the three steps:

- De-multiplexing of the raw frame sequence into separate sequences of each wavelength;
- Definition of a ROI_{ip} of arbitrary size;
- Averaging pixel values of the ROI_{ip} to form raw waveforms over frame number for the frame sequence of each wavelength.

The process is illustrated in Figure 5. 7.

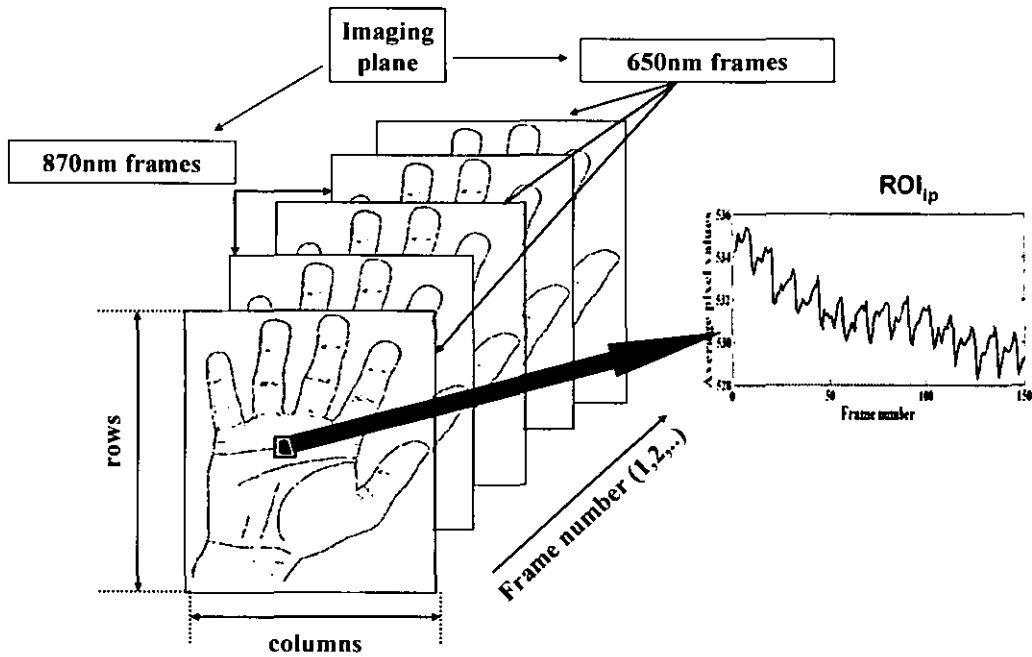


Figure 5. 7 A schematic diagram of post signal processing of detected light intensity.

The average pixel value represents the detected light intensity and the frame number is related to the time t by the frame rate of camera:

$$t = \text{Frame number} / \text{Frame rate} \quad [5. 1]$$

The discrete-time waveform represents the raw IPPG signal.

5.2 VALIDATION PROCEDURE

The ray data processing functions in section 4.2 used to process MC data generated *MPL'* for the opto-physiological model, and the post data processing functions yielded IPPG signals for the validation study. The MC simulation and the experimental platform are then ready for the validation of the opto-physiological model. The CCD camera with F-mount lens was selected as the detector in the validation experiment due to its better spectral response and higher dynamic range.

The validation procedure was achieved in two stages including the *in-vitro* validation on the multi-layered phantom and *in-vivo* validation on the healthy subject. Figure 5. 8 illustrates the concept of the validation. As the assumptions and parameters of the opto-physiological model approach those occurring in the corresponding real-life experiment, the outputs of the opto-physiological model and the experiment increasingly correlate. The high correlation proves the validity of the model.

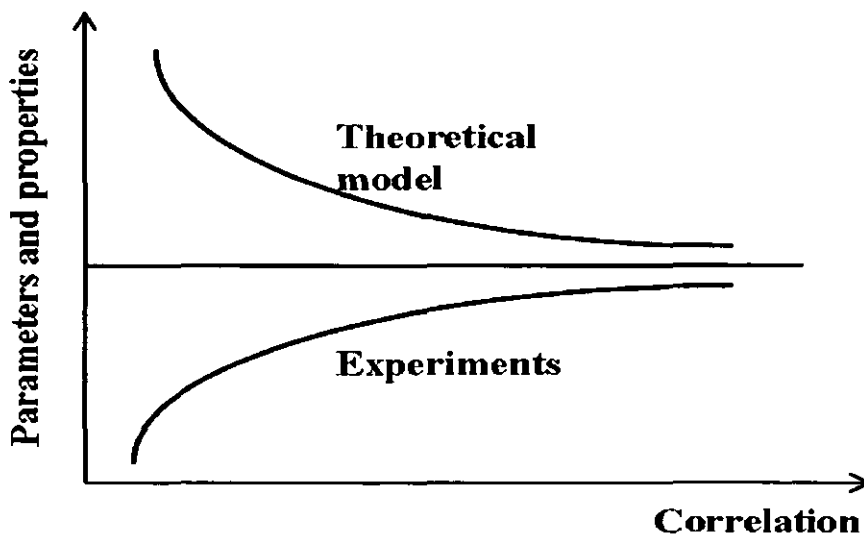


Figure 5. 8 The concept of the validation.

5.2.1 Phantom-Based Validation

5.2.1.1 Experimental phantom preparation

The following factors should be considered during the preparation of appropriate tissue phantoms:

- The structure of the phantom should be suitable for the experimental platform of IPPG;
- The scattering and absorption properties should be close to those of human tissues;
- The absorption and scattering coefficients should be controlled independently to test the accuracy of the opto-physiological model under different conditions;
- The materials should be easy to obtain, safe to use, and acceptably stable.

Balancing the above factors, commercial milk (semi-skimmed, Sainsbury Supermarkets Ltd., UK), food dye (FD&C blue #1, ROHA Ltd., UK) and gelatine (Somerfield Stores Ltd., UK) were selected as the main components of the phantom in the experiment. The milk serving popularly as a scattering substance^{[71][72]} is close to the scattering properties of human skin about 7 mm^{-1} . It can be easily diluted with water to change the scattering properties of the phantom with negligible absorption about 0.0085 mm^{-1} in near infrared range^{[73][74]}. The dye, FD&C Blue #1, was added to increase light absorption preferentially at 650 nm . As the dye can be fully dissolved in water, it does not introduce scattering^[75]. The gelatine mainly provided the structural support so that the solidified layers could be formed to fit into the setup of the reflection-mode IPPG.

A. Phantom construction

The gelatine was firstly dissolved into the dye solution. Measured volume of water-dye-gelatine was then mixed with measured volume of diluted milk. The mixture was poured into a container with a magnetic stirrer (HI 200M, Hanna Instruments Ltd., UK) underneath to keep the mixture homogeneous in the container. When intensive mixing, the container with the mixture was placed in the refrigerator

to solidify. The two-layered phantom was formed by pouring water-milk-gelatine-dye on top of a layer of solidified phantom. Absorption and scattering coefficients can be changed by adjusting the concentrations of dye and milk solution. The procedure of the phantom construction is presented in Figure 5. 9.



Figure 5. 9 The construction of phantoms with different absorption and scattering coefficients.

B. Measurement of optical properties

Following Equation 4.1 and 4.2, the absorption and scattering coefficients of the phantom were computed as a linear combination of the absorption and scattering coefficients of each component. As introduced previously, water-dye-gelatine and milk are the only components attributed to absorption and scattering coefficients respectively, Equation [4. 1] and [4. 2] can be derived as:

$$\mu_a = \sum_j (f_j \times \mu_{a,j}) = f_{dye} \times \mu_{a,dye-gelatine} \quad [5. 2]$$

$$\mu_s = \sum_j (f_j \times \mu_{s,j}) = f_{milk} \times \mu_{s,milk} \quad [5. 3]$$

where

$\mu_{a,dye-gelatine}$ the absorption coefficient of water-dye-gelatine, mm^{-1}

$\mu_{s,milk}$ the scattering coefficient of milk solution, mm^{-1}

$f_{dye-gelatine}$ the volume fraction of water-dye-gelatine

f_{milk} the volume fraction of milk solution.

The absorption and scattering coefficients of water-dye-gelatine and milk were derived from the measurements using a spectrometer (USB4000, Ocean Optics Inc., USA) and a tungsten halogen lamp (LS-1, Ocean Optics Inc., USA). The measurement was performed in an optical transmission method as shown in Figure 5. 10.

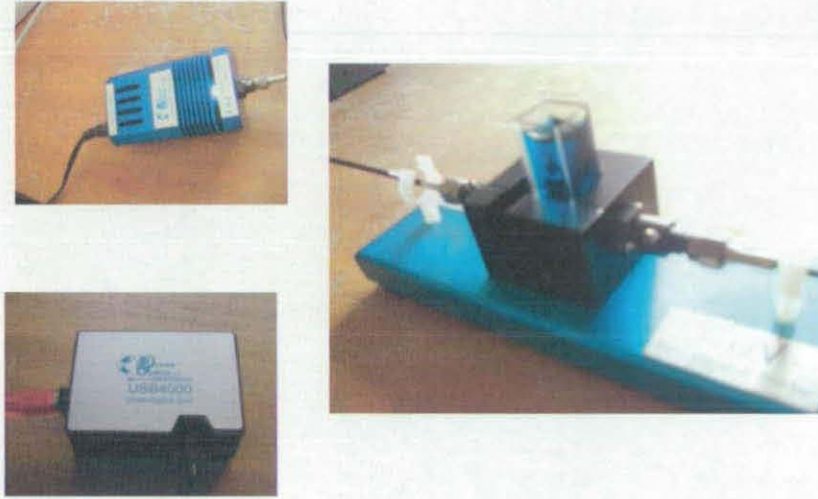


Figure 5. 10 The setup of the measurement of optical properties including a cuvette holder (right), the spectrometer (left bottom), and the lamp (left top).

A 10 mm cuvette loaded with the sample of mixtures was placed in a cuvette holder (CUV-UV holder for 1 cm cuvette, Ocean Optics Inc., USA). The tips of the source and the detector fibre were connected to both sides of the holder and perpendicular to the cuvette. The measurement was repeated three times for each sample and the mean absorbance A_{mean} at the wavelength of 650 nm was recorded for the calculation of μ_a .

To calculate the absorption coefficient $\mu_{a,dye-gelatine}$, the cuvette was filled with the sample of water-dye-gelatine. Following Equation [3. 4], $\mu_{a,dye-gelatine}$ can be derived as:

$$\mu_{a,dye-gelatine} = \frac{A_{mean}}{l} \quad [5. 4]$$

where path length l is the thickness of the cuvette's cavity, i.e. 10 mm.

The scattering coefficient $\mu_{s,milk}$ can not be directly measured as $\mu_{a,dye-gelatine}$, as the expected values are too high beyond the measuring range of the spectrometer. An indirect method was employed to address this problem. The cuvette was loaded with a sample of low concentration milk. When the acceptance angle of the optical detector is very small at best close to zero, single scattering can be assumed in the case of a thin cuvette and low concentration ^[76]. The absorbance of diluted milk can be expressed as:

$$A = \varepsilon_s \times C \times d \quad [5. 5]$$

where

C the concentration of milk solution, %

l the thickness of the cuvette's cavity, mm

ε_s the wavelength-dependent molar scattering coefficient, $M^{-1}mm^{-1}$.

In this investigation, the commercial milk serves as the stock solution and 100% concentration refers to non-diluted of the stock. When fixing the thickness of the cuvette, the molar scattering coefficient ε_s of the milk solution was deduced to be proportional to the slope of the A - C plot in Figure 5. 11.

Based on the thickness of 10 mm , ε_s was calculated as $0.156 mm^{-1}/(\%C)$. The value is nearly identical with the previous literature, in which ε_s was calculated as $0.148mm^{-1}/(\%C)$ ^[77]. For a specific concentration of milk solution, the scattering coefficient $\mu_{s,milk}$ can then be derived as:

$$\mu_{s,milk} = \varepsilon_s \times C \quad [5. 6]$$

The specification and the optical properties of the food dye are detailed in Appendix IV.

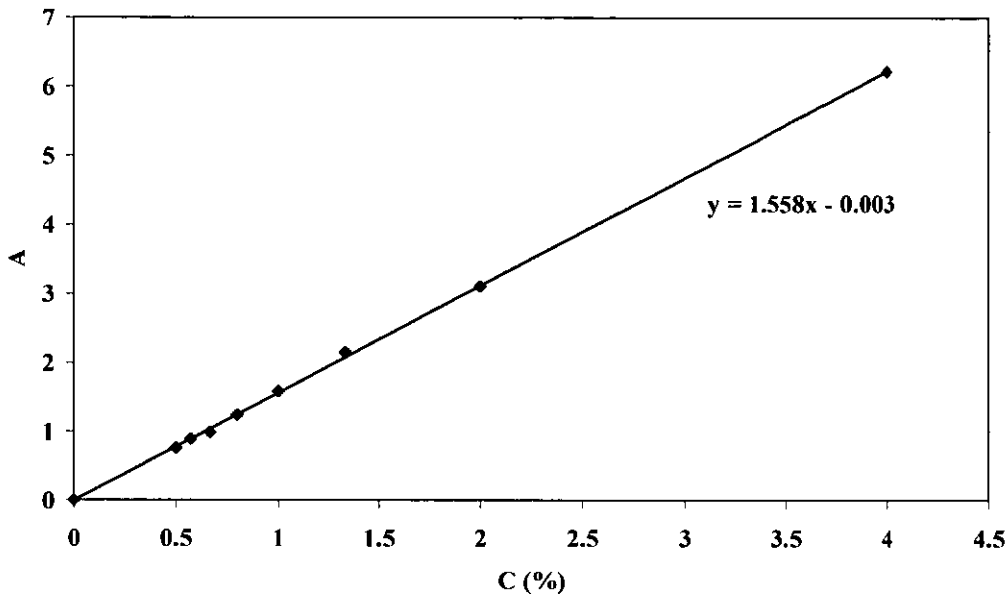


Figure 5. 11 The A - C plot of diluted milk. The square blocks represent absorbance A corresponding to different concentration C of milk. The straight line is the linear trend of these blocks. The 100% concentration refers to non-diluted of milk stock.

5.2.1.2 Multi-layered phantom model in simulation

To simulate the actual phantom, the multi-layered phantom model was constructed consisting of up to two homogeneous layers. Each layer was uniformly thick and the geometry of the model was defined by the size of the experimental phantom. The absorption and scattering coefficients were set close to those of actual phantoms at 650nm.

In the experiment, the diameter of the diaphragm aperture of the F-mount zoom lens of the CCD camera with focal length (FL)=50 mm, $f/\# = 1.8$ was calculated as $50\text{mm}/1.8 \approx 28\text{ mm}$. To simulate this lens, a double-convex lens in the Edmund Optics catalogue (Dia: 30 mm, FL: 50 mm, Centre thickness: 6.55 mm, $R_1 = -R_2$: 50.67 mm) was selected to be closest to the F-mount lens in the experiment. The double-convex lens was positioned 130 mm away from the surface of the tissue model in OptiCAD. Light impinging upon the tissue was simulated using parabolic reflector and multiple spherical light sources which were designed to the same arrangement as shown in Figure 5. 3. Only the rays that fall into the lens aperture are considered for the calculation of MPL.

5.2.1.3 Validation analysis

As parameters and optical properties of the model in MC simulation were close to those of the actual phantom, the simulation was expected to give a good approximation to the real light propagation in tissue. The theoretical A'_{theo} of multi-layered phantom can be expressed following Equation [3. 25] as:

$$A'_{theo} = \sum_{i=1}^k [\mu_a(i) \times MPL_{aperture}'(i)] \quad [5. 7]$$

where $\mu_a(i)$ is the absorption coefficient of layer i , k is the total number of tissue layers and the $MPL_{aperture}'(i)$ represents the aperture-dependent MPL' calculated using Equation [4. 6] based on the group of rays collected by the defined lens aperture.

In phantom-based experiments, the experimental absorbance A_{exp} can be derived as:

$$A_{exp} = -\ln\left(\frac{I'}{I_s}\right) \quad [5. 8]$$

where I_s is the light arriving at the camera when $\mu_a=0$ and I' is the scattered light intensity collected by the camera.

With the change of the optical properties in both simulation and experiment, the phantom-based validation of the opto-physiological model can be achieved by the comparison between A'_{theo} and A_{exp} .

5.2.2 Subject-Based Validation

5.2.2.1 Experiment preparation

In the subject-based experiment, the IPPG signal consists of a static component DC and a dynamic component AC . To yield discrete values of DC and AC from the raw data, the following steps were performed:

- Extraction of quasi-static DC components from raw signals via low-pass filtering;

- Extraction of AC components via subtraction of DC from the raw signal.

A moving average method (“smooth” in MATLAB) was introduced when performing low-pass filtering for the extraction of the quasi-static DC component from the raw IPPG signal. For extraction of quasi-static DC components, the window size should be such that it keeps the DC signal within all peaks and troughs of the raw signal while showing negligible rippling of the heart rate (HR) fundamental frequency found in the latter as shown in Figure 5. 12.

Once the optimum filter parameter was determined, it was kept constant within all signals produced under the specific hardware configuration.

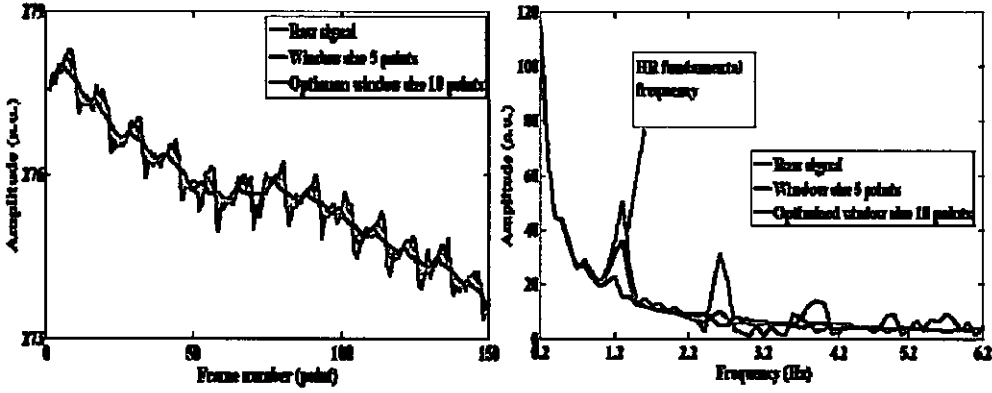


Figure 5. 12 Visual assessments of low-pass filter parameters for quasi-static DC extraction. The raw signal and filtered dc signals in time domain are plotted in the left figure. The Fourier spectra of these signals are plotted in the right figure.

To represent the static light intensity I_{static} and dynamic light intensity $I_{dynamic}$ in the opto-physiological model, the mean value of the DC signal and the mean amplitude of the AC signal are yielded by a custom “PPI” function in Matlab as the following steps:

- The ac_{PPI} is defined as the absolute value from the peak to the trough of the AC signal, and the interval is defined as the absolute value between two wave troughs, termed ‘pulse to pulse interval’ (PPI) as shown in Figure 5. 13. The AC amplitude for each PPI was calculated, and the mean amplitude ac was obtained by:

$$ac = \frac{\sum ac_{PPI}}{N_{PPI}} \quad [5. 9]$$

where N_{PPI} is the total number of PPI during the period of recording and ac is calculated to represent $I'_{dynamic}$ in Equation [3. 24].

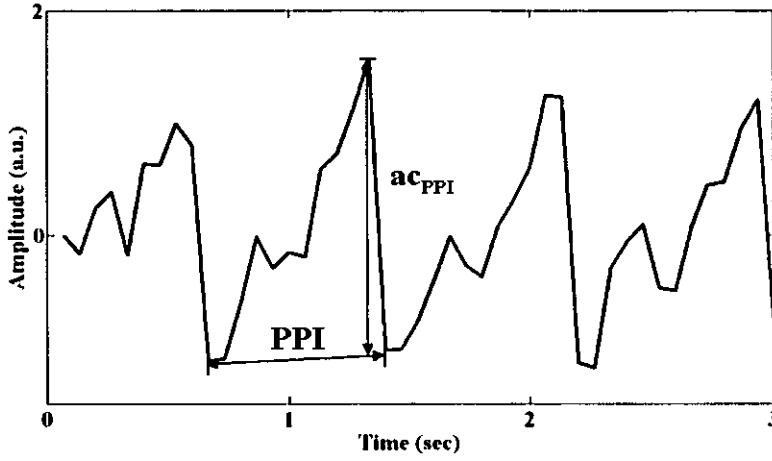


Figure 5. 13 A diagram of the pulse-pulse interval PPI and AC amplitude ac_{PPI} for each PPG.

- The raw IPPG signal is formed by averaging pixel values of the specific ROI over frame number of the frame sequence and the frame number is transformed to time as shown previously in Figure 5. 7 and Equation [5. 1]. dc_{frame} is defined as the value of the DC signal for each frame as shown in Figure 5. 14, and mean value dc was calculated by:

$$dc = \frac{\sum dc_{frame}}{N_{frame}} \quad [5. 10]$$

where N_{frame} is the total number of frames during the period of recording and dc represents I'_{static} in Equation [3. 24].

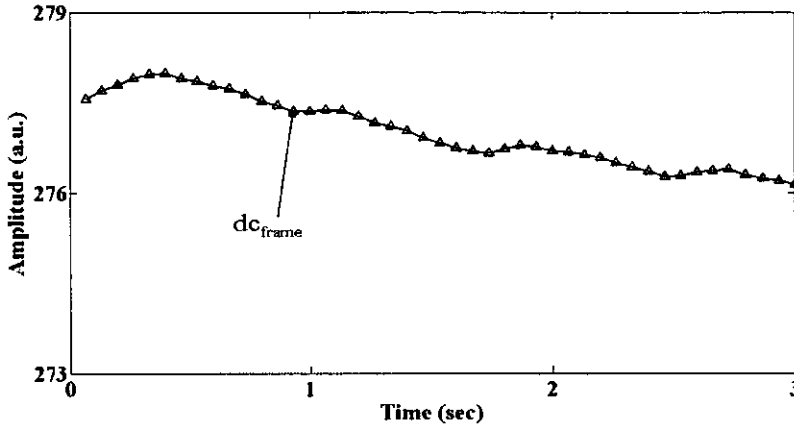


Figure 5. 14 A diagram of the dc_{frame} .

- Following Equation [3. 24], $I'_{perfusion}$ can be represented by the calculation of the ratio R_{exp} of the experimental ac and dc as:

$$R_{exp} = \frac{ac}{dc} \quad [5. 11]$$

5.2.2.2 Skin tissue model in simulation

Since the mean penetration depth of the light source emitting at 650nm and 870nm is into deep dermis layer of human skin ^[78], a tissue model in MC simulation consisting of six layers up to hypodermis was constructed.

The description of a multi-layered skin tissue is described from a simplified anatomy, as shown in Figure 5. 15. The layer was numbered from 1 (most shallow) to 6 (deepest). Each layer was given a name suggestive of the corresponding anatomical structure.

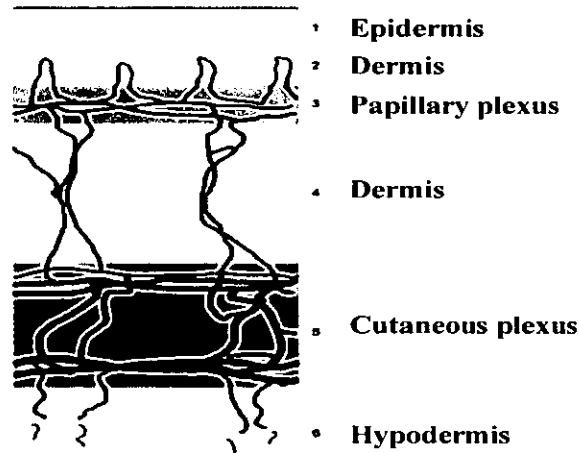


Figure 5. 15 A six-layered description of skin tissue model.

A blood free layer of dermis separated the epidermis from the papillary plexus. The bottom four layers perfused with blood were the main contributors of pulsatility in the tissue model. The melanin content was not considered in the epidermal layer of this tissue model. The contribution of melanin to absorption becomes 10 times smaller in the NIR region ^[79] compared to the UV region as Figure 2. 8 shows. Moreover, since the volume fraction of melanin in the epidermis accounts only very low percent around 6% ^[80] in tissue, it just modestly affects the light transport. Apart from the difference of the optical characteristics, the geometry of the tissue model is similar to the five-layer skin model utilized by Tuchin ^[48] and the six-layer skin model by Reuss ^[20].

In blood perfused layers, the principal absorbers in the NIR region are blood as introduced in section 2.1.2. Hence the bulk absorption coefficients of dermis and other highly vascularised tissues in this spectral region depend on the blood content. In the NIR region, scattering in the dermis and in the sub-dermal tissues dominates absorption. The structures that contribute most to scattering in skin are collagen fibre bundles and red blood cells, which cause highly forward-directed scattering ^[81]. The wavelength-dependent optical properties of blood and tissue from literature ^{[20] [44] [52]} are listed in Table 5. 1.

| Var. | Meaning | 650nm | 870nm |
|-----------------------------------|------------------------------|---------|---------|
| $\mu_{a,bloodless}$ (mm^{-1}) | absorption, bloodless tissue | 0.0285 | 0.0245 |
| $\mu_{a,blood}$ (mm^{-1}) | absorption, blood | 0.397 | 0.583 |
| $\mu_{s,bloodless}$ (mm^{-1}) | scattering, bloodless tissue | 7.150 | 4.45 |
| $\mu_{s,blood}$ (mm^{-1}) | scattering, blood | 161.374 | 106.888 |

Table 5. 1 Optical properties of blood and bloodless tissue at 650nm and 870nm illumination.

The total blood fraction (nominal 5%) is the mean concentration of blood in the total tissue volume during the diastolic state. Layer thickness $d(i)$, and blood fraction $f(i)$ for each layer in the diastolic state with nominal total blood fraction of 5% [20] is listed in Table 5. 2.

| Layer i | Name | d (mm) | f (%) |
|-----------|------------------------------|----------|---------|
| 1 | Epidermis | 0.06 | 0 |
| 2 | Dermis | 0.2 | 0 |
| 3 | Papillary Plexus Superficial | 0.2 | 5.56 |
| 4 | Dermis | 0.8 | 4.17 |
| 5 | Cutaneous Plexus Profundus | 0.6 | 20.4 |
| 6 | hypodermis | 8.0 | 4.17 |

Table 5. 2 Layer thickness d_i and blood fraction f_i for each layer in the non-pulsatile state.

Following Equation [4. 1] and [4. 2], the absorption and scattering coefficients of the skin tissue model were computed as the combination of those coefficients of whole blood and bloodless tissue weighted by their respective volume fractions:

$$\mu_a = (1 - f_{blood}) \times \mu_{a,bloodless} + f_{blood} \times \mu_{a,blood} \quad [5. 12]$$

$$\mu_s = (1 - f_{blood}) \times \mu_{s,bloodless} + f_{blood} \times \mu_{s,blood} \quad [5. 13]$$

where

- f_{blood} the total blood volume fraction
- $\mu_{a,bloodless}$ the absorption coefficient of bloodless tissue, mm^{-1}
- $\mu_{s,bloodless}$ the scattering coefficient of bloodless tissue, mm^{-1}
- $\mu_{a,blood}$ the absorption coefficient of whole blood, mm^{-1}
- $\mu_{s,blood}$ the scattering coefficient of whole blood, mm^{-1} .

Since each layer was assumed uniformly thick, its relative volume was expressed by its relative thicknesses alone. The pulsatile fraction is the fraction of the total tissue volume displaced by the arterial pulse. A nominal diastolic blood fraction $f_{blooded}$ was 5% with nominal pulsatile fraction f_{pulse} as 0.25% [20]. The pulsatile blood fraction was applied uniformly to all perfused layers:

$$f_{pulse}(i) = \left[\frac{d(i)}{d} \right] \times f_{pulse} \quad [5. 14]$$

where

$f_{pulse}(i)$ the pulse blood fraction of layer i

$d(i)$ the thickness of layer i , mm .

d the total thickness, mm .

The optical properties at 870nm for each layer are listed in Table 5.1, calculated from the Equation [5. 12] and [5. 13].

| Layer | $\mu_{a,non-pulsatile}$ (mm^{-1}) | $\mu_{s,non-pulsatile}$ (mm^{-1}) | $\mu_{a,pulsatile}$ (mm^{-1}) | $\mu_{s,pulsatile}$ (mm^{-1}) |
|-----------------------------|------------------------------------------|------------------------------------------|--------------------------------------|--------------------------------------|
| Epidermis (1) | 0.02450 | 4.4500 | 0.02450 | 4.4500 |
| Dermis (2) | 0.02450 | 4.4500 | 0.02450 | 4.4500 |
| Dermis Plexus (3) | 0.05556 | 10.1455 | 0.05559 | 10.1507 |
| Dermis (4) | 0.04779 | 8.7217 | 0.04791 | 8.7424 |
| Dermis Plexus Profundus (5) | 0.1383 | 25.3166 | 0.1384 | 25.3321 |
| hypodermis (6) | 0.04779 | 8.7217 | 0.04892 | 8.9294 |

Table 5. 3 The optical properties of each tissue layer of 870nm.

As introduced in section 4.2, the arterial pulsation was simulated by adding the pulsatile blood into non-pulsatile tissue and thus increasing the blood volume fraction. Consequently, $MPL_{dynamic}$ was calculated by Equation [4. 7] based upon the tissue models with pulsatile optical properties and non-pulsatile properties, respectively.

The anisotropy factor g was set to be 0.8 [43]. Although certain components of the tissue volume such as collagen [82] and red blood cells [83] are more forward-scattering, the value of 0.8 is more representative of overall dermal scattering. The refractive index for all the layers was set to be 1.4, based upon the

results of a recent study [84]. It should be noted that the model layer interfaces are artificial, in the respect that the actual structural interfaces in tissue (e.g., vessel walls) are at a finer level of detail than the model represents. The simplifying assumptions made here are similar to those used in other studies [20] [43] [52].

Similar to the multi-layer phantom model in simulation in section 5.2.1.2, the double-convex lens in the Edmund Optics catalogue (Dia: 30 mm, FL: 50 mm, Centre thickness: 6.55 mm, $R_1 = -R_2$: 50.67 mm) was selected to simulate the F-mount lens. The double-convex lens was positioned 130 mm away from the surface of the tissue model in OptiCAD. Light impinging upon the tissue was simulated using parabolic reflector and multiple spherical light sources which were designed to the same arrangement as shown in Figure 5. 3.

5.2.2.3 Validation analysis

In the subject-based experiment, the ratio R_{exp} of the static and dynamic light intensity can be calculated in Equation [5. 11].

In the opto-physiological model, the ratio of the value of the static and dynamic components can be derived following Equation [3. 27] as:

$$R_{theo} = \sum_{i=1}^k [\mu_{a,blood}(i) \times MPL'_{dynamic,aperture}(i)] \quad [5. 15]$$

where the $MPL'_{dynamic,aperture}(i)$ represents the aperture-dependent $MPL'_{dynamic}$ calculated using Equation [4. 6] based upon the rays that fall into the lens aperture. The correlation between R_{theo} and R_{exp} indicates the validity of the opto-physiological model in real-life measurement. The ratio can also be compared with heuristic values that the dynamic component accounts for only 0.1-2% of the total intensity [18].

5.3 MAPPING FUNCTION

When the opto-physiological model is validated, it can be applied in biological measurement to construct blood perfusion mapping. The CMOS camera with

C-mount lens was selected as the detector in this investigation, as its large capturing area can benefit the perfusion mapping.

5.3.1 2-D mapping of static and dynamic component

A custom mapping function in MATLAB was called to map the blood perfusion from a designated tissue. The dynamic, static light intensity and normalised intensity are represented by ac , dc and R calculated in Equation [5. 9], [5. 10] and [5. 11] of each ROI_{ip} . The ROI_{ip} -dependent ac , dc and R are then mapped to the corresponding physical location of each ROI_{ip} . Figure 5. 16 illustrates an example of the ac mapping function.

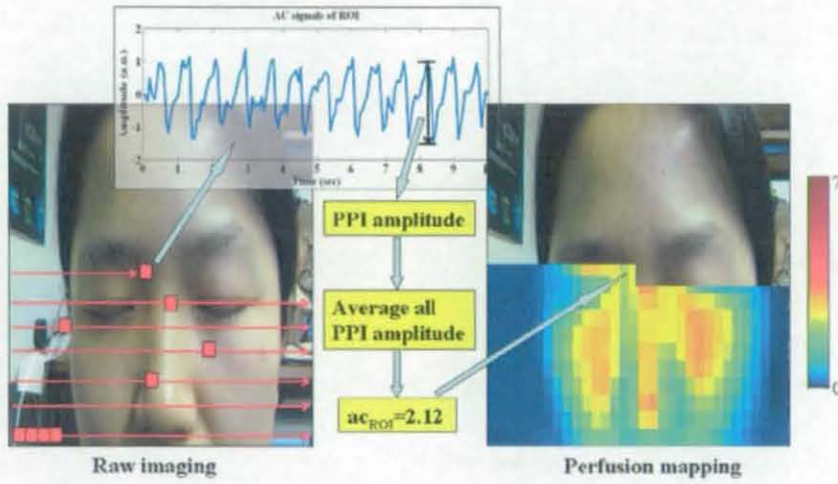


Figure 5. 16 An example of the 2-D ac mapping. ac_{ROI} is calculated from Equation [5. 9].

5.3.2 Layered mapping of blood perfusion

The conversion of 2-D mapping to 3-D perfusion mapping is performed by applying the opto-physiological model at each ROI_{ip} on the 2-D mapping, where the model allows for the determination of the relative contributions of different layers to the ROI_{ip} -dependent perfusion of the 2-D surface mapping.

The double-convex lens in the Edmund Optics catalogue (Dia: 8 mm, FL: 6 mm, Centre thickness: 2.54 mm, $R_1=-R_2$: 7.59 mm) was selected to simulate the C-mount lens. The double-convex lens was positioned 110 mm away from the surface of the tissue model in OptiCAD. Light impinging upon the tissue was simulated using

parabolic reflector and multiple spherical light sources which were designed to the same arrangement as shown in Figure 5. 3. Only rays that fall into the lens aperture are considered for the calculation of MPL .

The layered perfusion $R_{ROI_{ip}}(i)$ of each ROI_{ip} can be derived following Equation [3. 29] as:

$$R_{ROI_{ip}}(i) = R_{ROI_{ip}} \times w_{perfusion, ROI_{ip}}(i) = R_{ROI_{ip}} \times \frac{MPL'_{dynamic, ROI_{ip}}(i)}{\sum_k MPL'_{dynamic, ROI_{ip}}(k)} \quad [5. 16]$$

where $MPL'_{dynamic, ROI_{ip}}(i)$ is the ROI_{ip} -dependent dynamic MPL calculated by the difference of $MPL_{non-pulsatile, ROI_{ip}}(i)$ and $MPL_{pulsatile, ROI_{ip}}(i)$ in Equation [4. 7]. To derive $MPL_{non-pulsatile, ROI_{ip}}$ and $MPL_{pulsatile, ROI_{ip}}$ for each position of the ROI_{ip} in the image plane, the rays that go through the lens aperture is traced back in the corresponding ROI_{op} in the object plane as illustrated in Figure 5. 17. The ROI_{op} is defined by the size $X_{hw} \times Y_{hw}$ and it can be moved over the object plane by step of X_{int} and Y_{int} . $MPL_{non-pulsatile, ROI_{ip}}$ and $MPL_{pulsatile, ROI_{ip}}$ are calculated following Equation [4. 6] based on the rays going through each ROI_{op} .

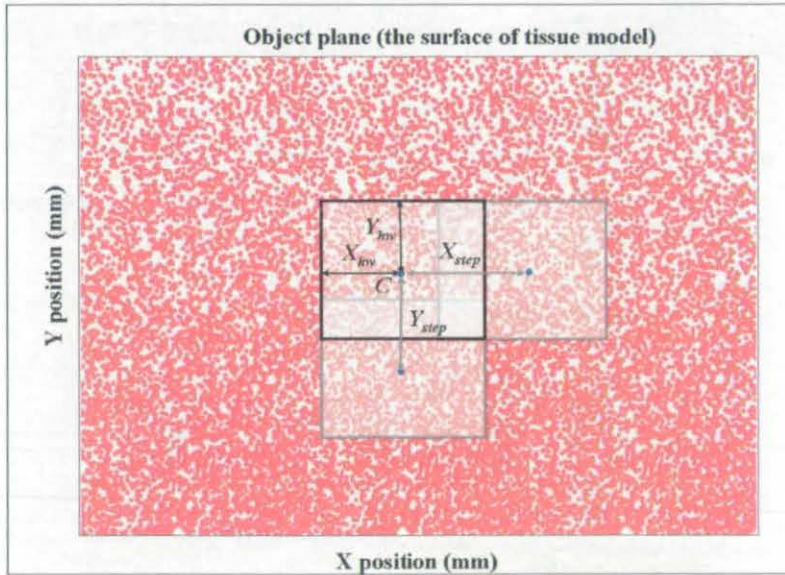


Figure 5. 17 A diagram of the ROI_{op} for the derivation of MPL . The ROI_{op} is defined by the center C and the size $X_{hw} \times Y_{hw}$. It can be moved over the object plane by step of X_{step} and Y_{step} .

Subsequently, the layered mapping can be achieved by mapping layered $R_{ROI_{ip}}(i)$ of each ROI_{ip} calculated from Equation [5. 16]. Figure 5. 18 illustrates an example of the mapping function for three layers.

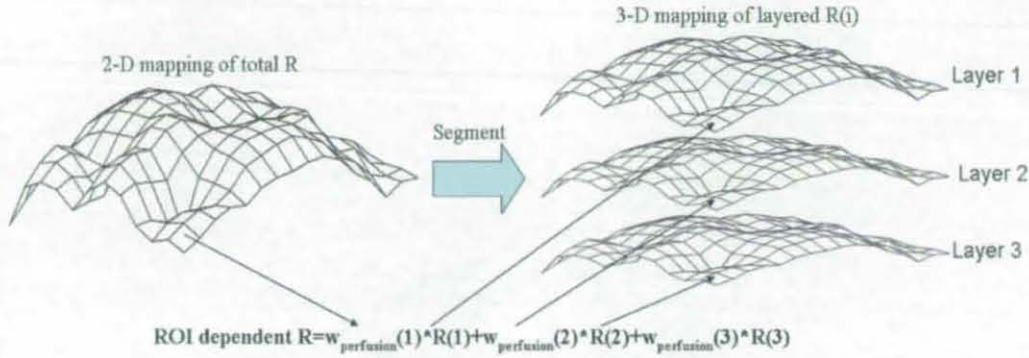


Figure 5. 18 An example of the 3-D mapping of layered R into three layers. $w(i)$ is the weight function for layer i .

Such kind of layered mapping illustrates the relationship between layered AC and DC signal, and the relationship between segmented signal and the total IPPG signal.

5.3.3 Spatial Resolution

The spatial resolution of the 2-D and layered perfusion mapping is determined by the size of ROI_{ip} , which is affected by the resolution of the captured frame, the quality of the IPPG signal and the tissue's spatial point spread function.

5.3.1.1 Effect of camera parameters on imaging resolution

The IPPG system captures a set of frames from the surface of tissue over a period of time. The resolution of each captured frame is dependent on the optical resolution of lens and the pixel size of the camera sensor. As shown in Figure 5. 19, the optical resolution of lens is determined by the diameter of diffraction-limited spot size (dsp).

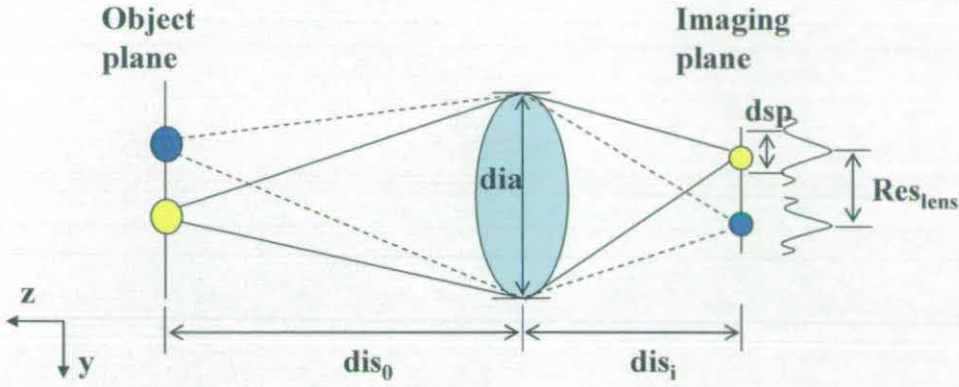


Figure 5.19 A schematic diagram of optical resolution Res_{lens} through a single lens with aperture diameter dia .

The dsp through a circular aperture is the Airy function of width as:

$$dsp = \frac{2.44 \times dis_i \times \lambda}{dia} \quad [5.17]$$

in which

$$\frac{1}{dis_0} + \frac{1}{dis_i} = \frac{1}{fl} \quad [5.18]$$

$$Mag = \frac{dis_i}{dis_0} \quad [5.19]$$

yields

$$dis_i = (Mag + 1) fl \quad [5.20]$$

The minimum resolution to distinguish two spots can be derived as:

$$Res_{lens} = \frac{dsp}{2} = \frac{1.22 \times (1 + Mag) \times \lambda \times fl}{dia} \quad [5.21]$$

where

Mag the magnification

λ the wavelength of illumination

- fl the focal length of the lens, i.e. 8 mm for the C-mount lens
- dia the diameter of the aperture, i.e. 5.7 mm for the C-mount lens

In the current setup, dis_0 is the distance between the measurement site and lens, i.e. 110 mm. dis_l was calculated from Equation [5. 19] as 8.5 mm and the Mag was calculated as 1/13 by Equation [5.20]. Following Equation [5. 21], the optical resolution Res_{lens} for the C-mount lens was calculated as $1.0 \times 1.0 \mu m^2$ of 650 nm and $1.5 \times 1.5 \mu m^2$ of 870 nm which are much smaller than the pixel size of the CMOS camera $12 \times 12 \mu m^2$. Thus the resolution of the captured frame is mainly determined by the pixel size of the camera.

5.3.1.2 Effect of quality of IPPG signal on ROI_{ip}

Looking at the imaging plane in Figure 5. 7, each captured frame is divided into small ROI_{ip}. Averaging pixel values of each ROI_{ip} forms the raw IPPG signal. The relationship between the size of ROI_{ip} and the quality of AC signals is presented in Figure 5. 20 from the sequence of frames under 870nm illumination. Figure 5. 20 illustrates that larger ROI_{ip} yields a signal with smaller distortion and consistent peak-to-peak intensity compared to the signals from smaller sizes of ROI_{ip}. This means spatial averaging of the pixel value is a useful approach to significantly reduce the effect of motion artefacts and improve SNR.

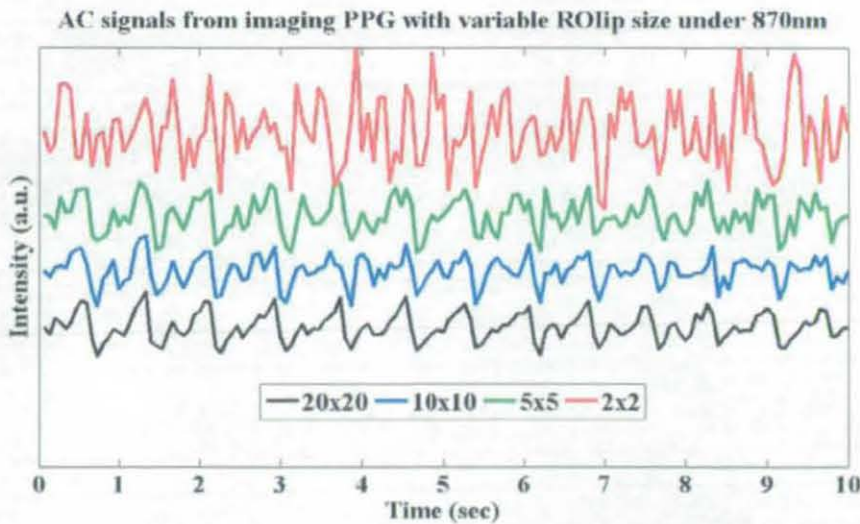


Figure 5. 20 AC signals generated with different sizes of ROI_{ip} (20x20, 10x10, 5x5, 2x2 pixel²) under 870nm illumination following the procedure in Figure 5. 7.

On the other hand, to distinguish between different compartments of the measurement tissue such as the nose and cheek of the face, the smaller ROI_{ip} is preferred as shown in Figure 5. 21, which presents the mapping of ROI_{ip} -dependent dc calculated using Equation [5. 10] under 870nm illumination is presented in a 2-D format with different sizes of ROI_{ip} to illustrate the static component of the face.

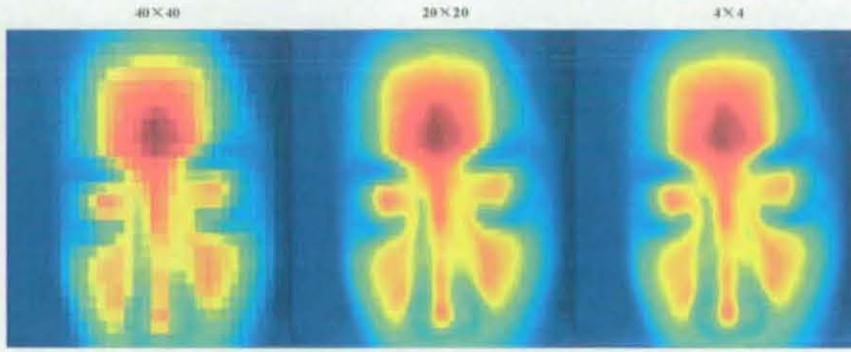


Figure 5. 21 The dc mapping with ROI_{ip} of size 40x40, 20x20, 4x4 pixel² under 870nm illumination on human face. ROI_{ip} -dependent dc was calculated using Equation [5. 10].

Thus the suitable size of ROI_{ip} needs to balance both the aspects to guarantee the relatively high SNR of the IPPG signal and also maintain the basic structure of the illuminated area.

5.3.1.3 Effect of tissue's spatial point spread function on ROI_{ip}

As previously discussed in section 5.3.2, $MPL_{ROI_{ip}}$ is derived by tracing back the rays that go through the lens aperture in the corresponding ROI_{op} in the object plane as illustrated in Figure 5. 17. The relationship between ROI_{op} and ROI_{ip} follows:

$$ROI_{ip} = ROI_{op} \times Mag \quad [5. 22]$$

where Mag is the magnification calculated as 1/13 by Equation [5.20].

The ROI_{op} needs to be big enough to cover enough information to derive representative MPL for each layer, which is determined by the tissue's spatial point spread function of each layer. As the pulsatile component accounts for only a very small proportion of the total intensity, it just modestly affects the total light transport. Thus tissue's spatial point spread function based on non-pulsatile and pulsatile tissue

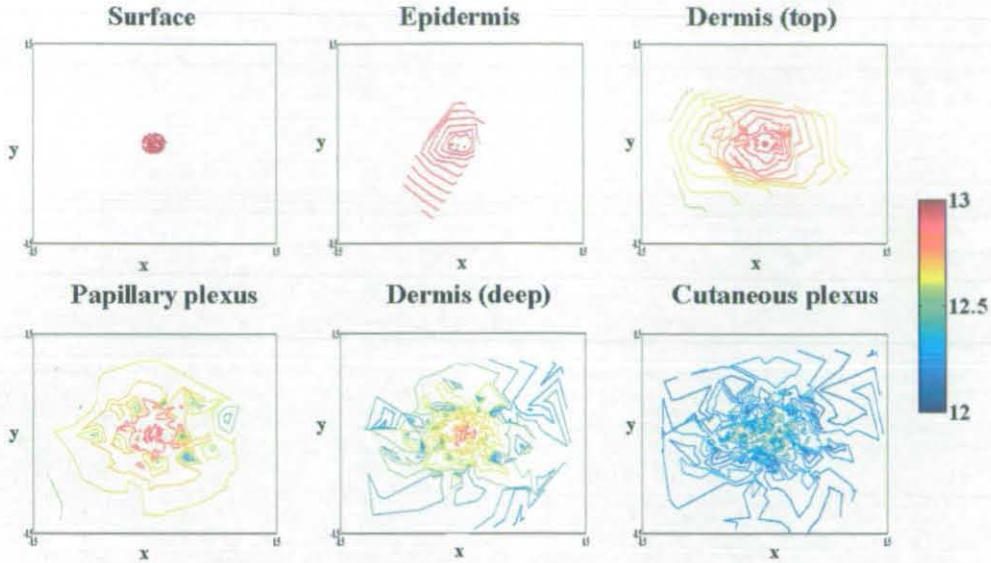


Figure 5. 23 The contour plots of $V.power$ at specific depths based upon six-layer tissue model in simulation except the hypo-dermis layer as no detected rays coming from that layer.

The contour plots in Figure 5. 23 demonstrate a loss of the definition in the Gaussian distribution with respect to depth, which may be due to a limited number of traced rays. The deeper the light penetrates, the higher the probability that rays have been backscattered out of the model. It is difficult to estimate by eye the spread distance of the tissue's spatial point spread function, especially in the deeper layers. By applying Gaussian fitting to the 2-D data of these contour plots at each depth, the standard deviation $\sigma = \sqrt{\sigma_x^2 + \sigma_y^2}$ is taken as a measure of the spread distance of the tissue's spatial point spread function, where σ_x and σ_y are the standard deviations along x and y dimension in a 2-D Gaussian distribution. Figure 5.24 demonstrates the relationship between σ and the depths of tissue layers.

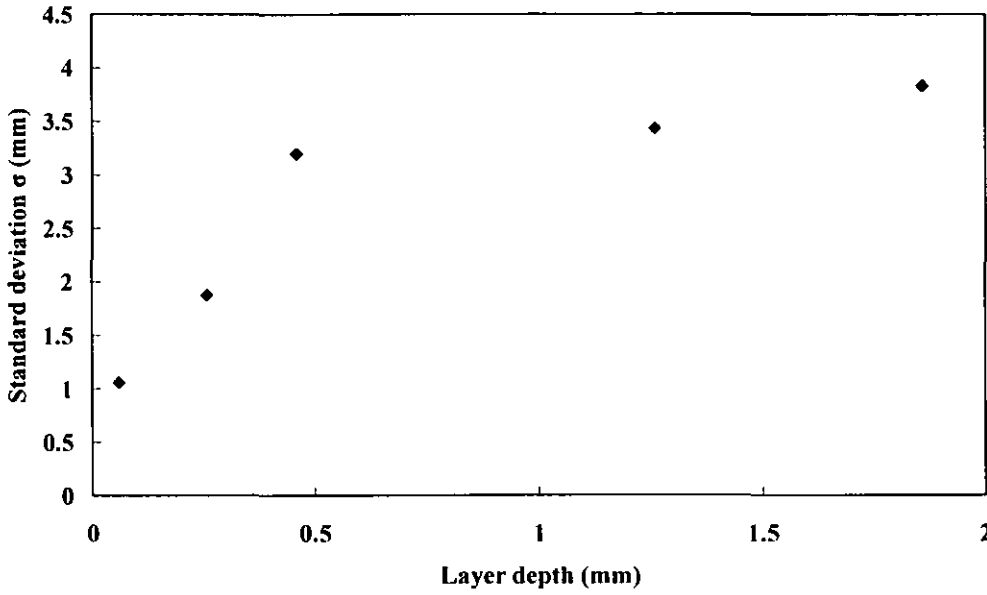


Figure 5. 24 The relationship between the tissue layer depth and the standard deviation σ of the Gaussian fitting to the 2-D data in the contour plots in Figure 5.23 at each layer.

Figure 5. 24 demonstrates σ of the Gaussian fitting of the cross sectional plots increases with respect to depth, which exhibits a diffusion of power distribution. This illustrates the reduction of optical spatial resolution when penetrating deeper. As about 95% of the values lie within $\text{mean} \pm 2\sigma$ for a Gaussian distribution, the spread distance of tissue's spatial point spread function at each layer is estimated as $4 \times \sigma$.

Given that the uniform illumination and the homogenous tissue model, the MPL for all layers should remain constant as long as ROI_{op} size is above the optical spatial resolution of the deepest layer, i.e. $(4 \times \sigma_{\text{cutaneous}})^2 = 15.3^2 \text{ mm}$, corresponding to the size of $\text{ROI}_{\text{ip}} 100 \times 100 \text{ pixels}^2$.

6. EXPERIMENTS, RESULTS AND DISCUSSIONS

Having developed the opto-physiological model and the experimental platform, this chapter moves on to detailing *in-vitro* and *in vivo* validation studies performed with both of these.

This chapter begins by presenting the results of the *in-vitro* validation based on multi-layered phantoms with emphasis on the correlation between opto-physiological and experimental outputs. The results of the *in-vivo* validation performed on healthy subjects were then refined and presented followed by an in-depth discussion of the sensitivity of the opto-physiological model and the limitation of the current setup. Finally, the application of the opto-physiological model to layered map blood perfusion is demonstrated.

6.1 VALIDATION BASED ON ONE-LAYERED PHANTOM

In this section the *in-vitro* validation was performed on a one-layered phantom to test the MC simulation platform and validate the assumptions of the opto-physiological model. This was achieved by investigating the relationship between the absorbance A and the optical properties of tissue, i.e. μ_a and μ_s , in both the opto-physiological model and the experiments.

6.1.1 Results of Experiment

6.1.1.1 Experimental setup

As described previously about the phantom construction in section 5.2.1.1, commercial milk (semi-skimmed, Sainsbury Supermarkets, Ltd., UK), food dye (FD&C blue #1, ROHA Ltd., UK) and gelatine (Somerfield Stores Ltd., UK) were selected as the main components of the phantom in the *in-vitro* experiment. The room temperature was maintained at 20 ± 2 °C during the experiment, and all the experiments from preparation to measurement were finished within a 4 hour period to keep the properties of milk stable ^[85].

Considering the effect of gelatine on the absorption coefficient, the portion of gelatine for all the measurements was kept constant as 5.72 g. The absorption coefficient of the water-dye-gelatine was thus mainly determined by the concentration of the dye solution. The absorbance $A_{dye-gelatine}$ of the water-dye-gelatine sample was measured by the spectrometer. The measurement was repeated three times and the mean absorbance A_{mean} at the wavelength of 650 nm was recorded for the calculation of $\mu_{a,dye-gelatine}$ using Equation [5. 4]. $\mu_{s,milk}$ was calculated using Equation 错误！未找到引用源。.

30ml water-dye-gelatine was then mixed with equal volume of diluted milk to keep the calculation of μ_a and μ_s in a simplified format. The mixture was then poured into a rectangular container with base dimensions of 100 mm×60 mm, resulting in the thickness of the phantom 10 mm. The magnetic stirrer was used to keep the mixture

homogeneous. When intensive mixing, the mixture was placed in the refrigerator to solidify for 2 hours.

As the scattering coefficient of water-dye-gelatine and the absorption coefficient of milk were disregarded, and the volumes of both were equal, μ_a and μ_s of this phantom can be calculated following Equation [5. 2] and [5. 3] as:

$$\begin{aligned}\mu_a &= \sum_j (f_j \times \mu_{aj}) = f_{\text{dye-gelatine}} \times \mu_{a,\text{dye-gelatine}} + f_{\text{milk}} \times \mu_{a,\text{milk}} \\ &= \frac{1}{2} \times \mu_{a,\text{dye-gelatine}}\end{aligned}\quad [6. 1]$$

$$\mu_s = \sum_j (f_j \times \mu_{sj}) = f_{\text{milk}} \times \mu_{s,\text{milk}} + f_{\text{dye-gelatine}} \times \mu_{s,\text{dye-gelatine}} = \frac{1}{2} \times \mu_{s,\text{milk}} \quad [6. 2]$$

The concentrations C of the dye and milk solution were varied to obtain different absorption and scattering coefficients. To simulate *in-vivo* tissue, the scattering coefficients μ_s were prepared to lie between 1 and 8 mm^{-1} , corresponding to the concentration of milk between 10% and 100%. Absorption coefficients μ_a were set to vary between 0.01 and 0.1 mm^{-1} , corresponding to the concentration of dye solution between 1.5×10^{-4} and $3.8 \times 10^{-3} M\%$.

The CCD camera was configured to capture 20fps. The ring light was adjusted to continuously illuminate at the single wavelength of 650nm. To increase SNR, the output power was configured to the highest possible value on the condition of not saturating the camera's sensor.

6.1.1.2 Experimental protocol

All the measurements were performed in a dark room to avoid the effect of ambient light. The phantom was positioned on an optical bench with black curtain underneath. The camera with the ring light around the lens was set to be 130 mm away from the optical bench with focus on the centre of the bench. Each measurement was set to capture 5 sec, i.e. 100 frames. Post signal processing of these raw frames was performed following the steps in Figure 5. 7. The mean values of the detected light intensity were yielded by averaging the pixel values of the whole captured area over

all the frames. The purpose for this is to minimise the effect of small inhomogeneities on the results of measurements.

The experiment was performed following four steps:

- Firstly, The dark noise I_{dark} of camera itself was firstly captured for 5sec without any illumination;
- The ring light was then set to continuously illuminate at 650nm, and a reflectance standard (SRS-99, Labsphere Inc., UK) was positioned at the centre of the optical bench. The detected light $I_{s,det}$ was captured from the surface of the reflectance standard, whose intensity consists of the scattered light I_s arriving at the detector when $\mu_a=0$ in Equation [3. 22] and the dark noise I_{dark} ;
- A phantom consisting of only distilled water and gelatine was then positioned on the bench for capturing. As there was no scattering in the water-gelatine phantom, the detected light was mainly coming from the surface reflection of the phantom, whose intensity was referred to as the reflected light intensity I_{ref} ;
- Finally, the milk-dye-gelatine phantom was placed at the same position as detailed in the last two steps. The detected light I_{det} mainly consists of the reflected light I_{ref} from the surface and the detector-dependent backscattered light I' through the internal components of the phantom. Thus the detector-dependent absorbance A_{exp} of the phantom-based experiment can be derived following Equation [5. 8] as:

$$A_{exp} = -\ln\left(\frac{I'}{I_s}\right) = -\ln\left(\frac{I_{det} - I_{ref}}{I_{s,det} - I_{dark}}\right) \quad [6. 3]$$

6.1.1.3 Experimental Results and discussion

Experimental results of the relationship between the absorbance A_{exp} calculated using Equation [6. 3] and absorption coefficients μ_a are presented in Figure 6. 1. The concentration C_{milk} of milk solution was prepared to 100%, resulting in the scattering coefficients μ_s of the phantom constant as $7.79mm^{-1}$ calculated using Equation [6. 2]. The absorption coefficients μ_a were calculated using Equation [6. 1] as 0.0122, 0.0263, 0.0455, 0.0612 and $0.0789 mm^{-1}$ respectively corresponding to different

concentrations of dye solution from 1×10^{-4} to $1.2 \times 10^{-3} M\%$. The curve fitting for the data is performed in Excel.

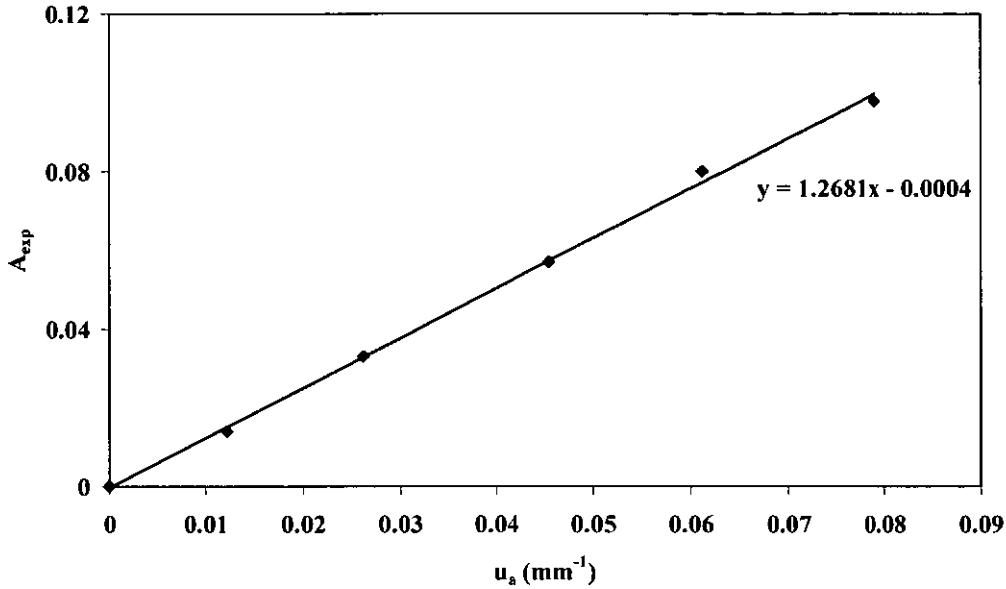


Figure 6. 1 Experimental results of A_{exp} of one-layered phantoms with different μ_a . The diamond blocks represent A_{exp} corresponding to $\mu_a=0, 0.0122, 0.0263, 0.0455, 0.0612$ and 0.0789 mm^{-1} . The solid line is the linear trend of these blocks.

In Figure 6. 1, A_{exp} of the one-layered phantom changes directly with the absorption coefficients μ_a . The approximate linear trend indicates that the absorbance can be regarded as a linear function of μ_a in the range of $0\text{-}0.08 \text{ mm}^{-1}$ when the scattering effect is constant.

Figure 6. 2 presents the experimental results of the relationship between A_{exp} calculated using Equation [6. 3] and scattering coefficients μ_s . The concentrations C_{dye} of the dye solution were prepared to $6.2 \times 10^{-4} M\%$ resulting in μ_a of the phantom constant as 0.0263 mm^{-1} calculated using Equation [6. 1]. μ_s were calculated from Equation [6. 2] as $3.89, 5.19, 6.23$ and 7.79 mm^{-1} respectively, corresponding to different concentrations of milk solution from 50% to 100%.

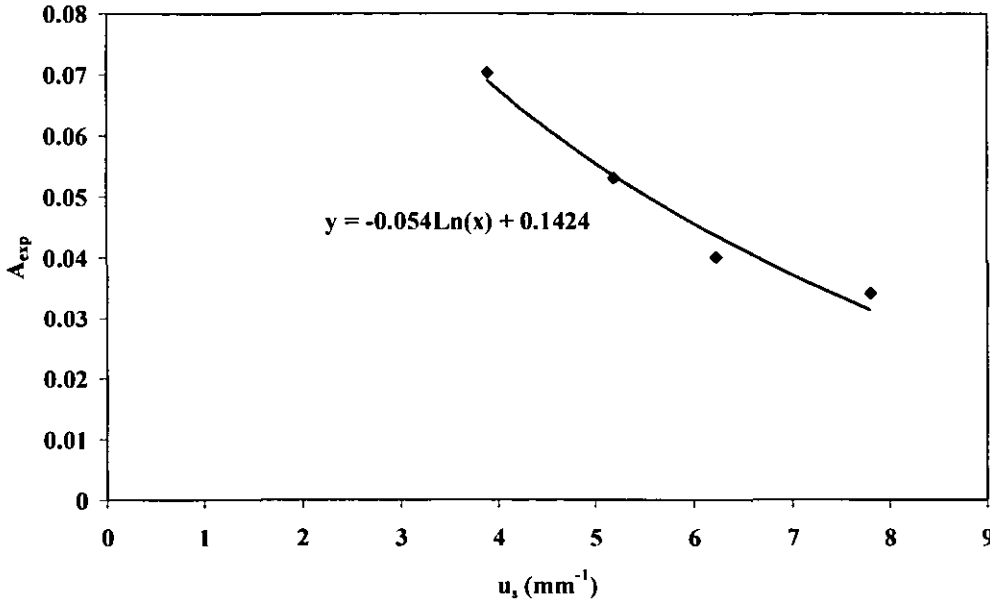


Figure 6. 2 Experimental results of A_{exp} of one-layered phantoms with different μ_s . The diamond blocks represent A_{exp} corresponding to $\mu_s=3.89, 5.19, 6.23$ and 7.79 mm^{-1} . The solid curve is the logarithm trend of these blocks.

Figure 6. 2 demonstrates a non-linear relationship between A_{exp} and μ_s . This indicates the significant effect of scattering on light propagation in a turbid medium. The absorbance non-linearly decreases when the scattering coefficients μ_s increase.

6.1.2 Results of Simulation

6.1.2.1 Simulation setup

In the simulation, the phantom model was constructed to approach the properties of the experimental phantom. As introduced previously about the phantom model of simulation in section 5.2.1.2, the one-layered phantom model was assumed to be homogeneous, and was characterised by a bulk absorption coefficient μ_a , scattering coefficient μ_s , anisotropy factor g and an index of refraction n . The geometry of the model was $100 \text{ mm} \times 60 \text{ mm} \times 10 \text{ mm}$ defined by the size of the experimental phantom. To simulate the optical properties of the actual phantom, μ_s was set to lie between 1 and 10 mm^{-1} . μ_a was set between 0.01 and 0.1 mm^{-1} . The anisotropy g was set to 0.72 and the refractive index n was to 1.41, identical to the properties of milk [73]. The surface reflection was disregarded.

6.1.2.2 Simulation Results and discussion

The main function of the simulation was to generate the aperture-dependent MPL' for the opto-physiological model. The aperture-dependent MPL' for the one-layered phantom model was calculated using Equation [4. 6] in a one-layered format following the procedure of the post data processing of the simulation in section 4.4. The results of the relationship between MPL' and μ_a of the one-layered phantom model are presented in Figure 6. 3. μ_s was set to 7.79 mm^{-1} . μ_a was set to 0.01, 0.03, 0.05, 0.07 and 0.09 mm^{-1} respectively close to the optical properties in the phantom-based experiments.

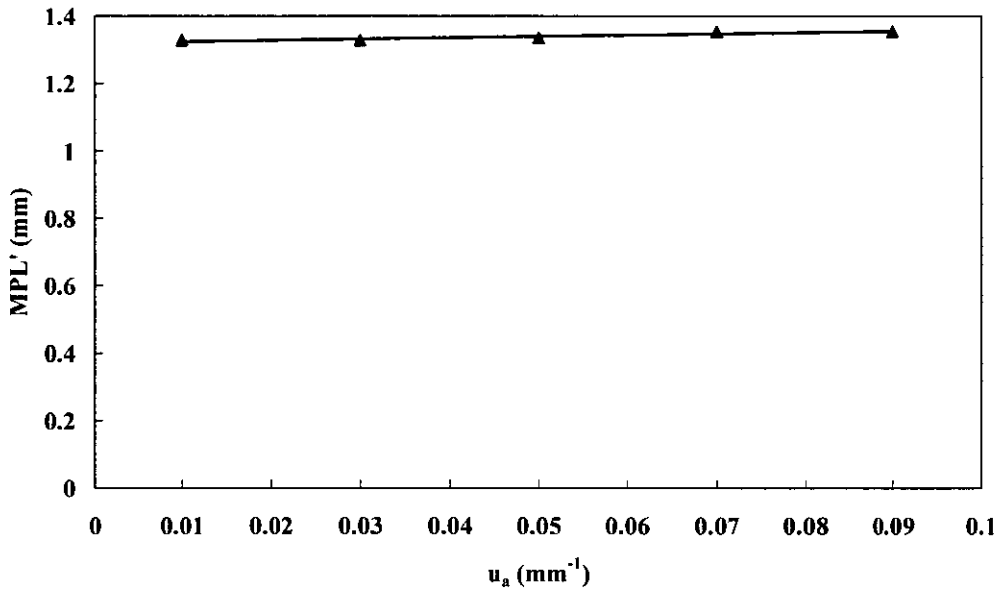


Figure 6. 3 Simulation results of MPL' on the one-layered phantom model with different μ_a . The triangle blocks represent MPL' corresponding to $\mu_a = 0.01, 0.03, 0.05, 0.07$ and 0.09 mm^{-1} . The solid curve is the linear trend of these blocks.

The MPL' in Figure 6. 3 shows little variation with change of μ_a . This indicates MPL' is mainly determined by scattering properties in the range of low μ_a from 0 mm^{-1} to 0.09 mm^{-1} .

Figure 6. 4 presents the results of MPL' yielded by the simulation on the one-layered tissue model with same μ_a , but different μ_s . The absorption coefficient μ_a was set to 0.0263 mm^{-1} . The scattering coefficients μ_s were set to 0, 3, 5, 7 and 9 mm^{-1} respectively, close to those of the experiments.

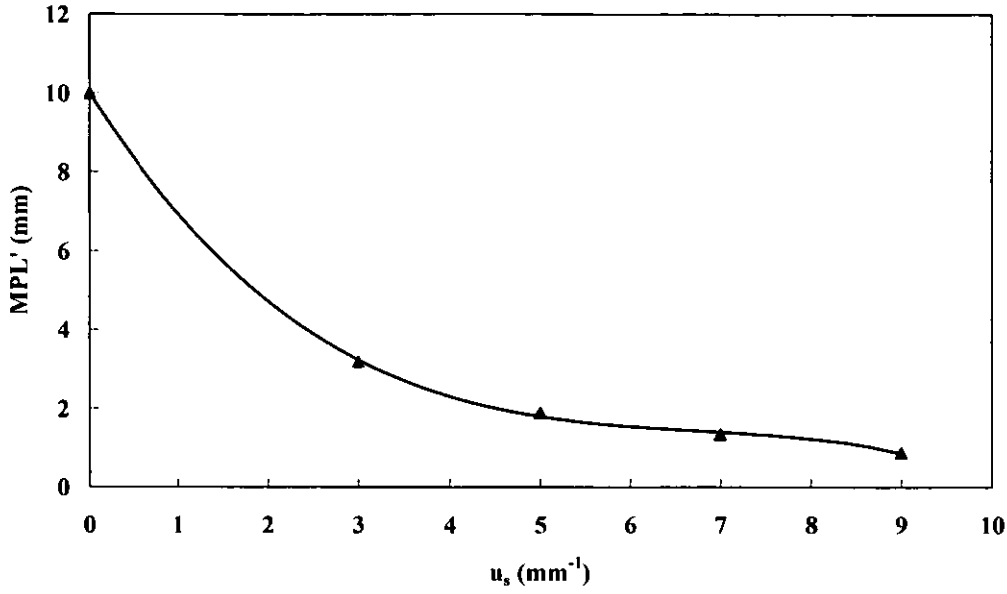


Figure 6. 4 Simulation results of MPL' on the one-layered phantom model with different μ_s . The triangle blocks represent MPL corresponding to $\mu_s = 0, 3, 5, 7$ and 9 mm^{-1} .

The MPL' in Figure 6. 4 demonstrates a non-linear function of μ_s , i.e. MPL' increases when the scattering coefficient decreases. With less effect of scattering, the light propagation tends to be more forward-directed and can transmit deeper into tissue. Thus the smaller the scattering coefficient is, the longer the path length is. When the scattering coefficient is 0, the path length is equal to the thickness of the phantom, i.e. 10 mm .

6.1.3 Validation Analysis

In the opto-physiological model, the absorbance A'_{theo} of the one-layered phantom model was derived in a one-layered format following Equation [5. 7] as:

$$A'_{theo} = \mu_a \times MPL_{aperture}' \quad [6. 4]$$

where

μ_a the wavelength-dependent absorption coefficient, mm^{-1}

$MPL_{aperture}'$ the aperture-dependent mean path length generated by the simulation as shown in Figure 6. 3 and Figure 6. 4.

In phantom-based experiments, the absorbance A_{exp} was calculated from Equation [6.3].

A'_{theo} and A_{exp} of the one-layered phantoms with same absorption coefficients μ_a , but different scattering coefficients μ_s are presented in Figure 6.5.

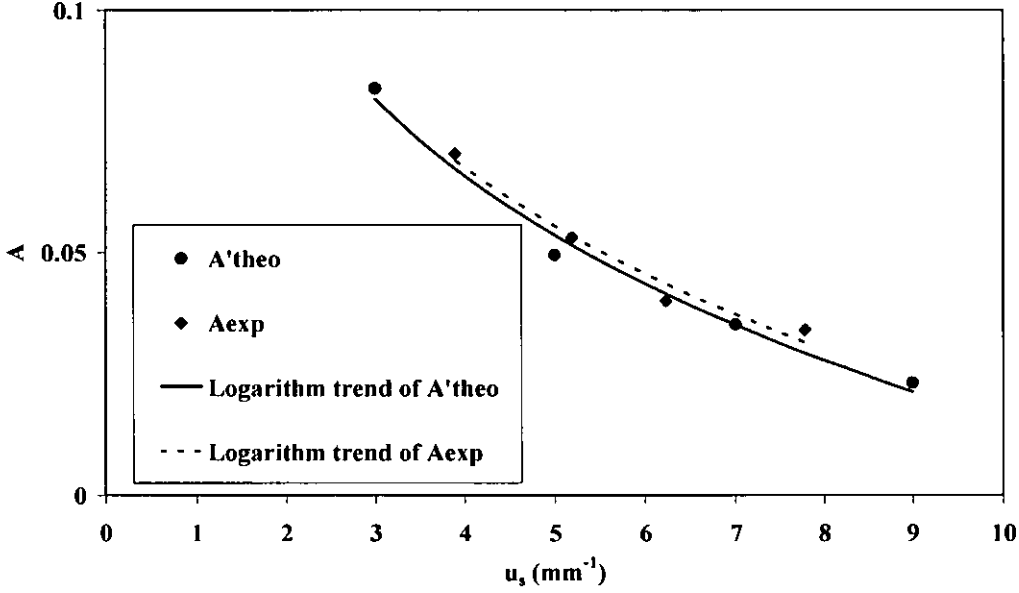


Figure 6.5 Results of A'_{theo} and A_{exp} of the one-layered phantoms with different μ_s . The absorption coefficient μ_a was set to 0.0263 mm^{-1} . The round blocks represent A'_{theo} corresponding to $\mu_s = 3, 5, 7$ and 9 mm^{-1} and the diamond blocks represent A_{exp} corresponding to $\mu_s = 3.89, 5.19, 6.23$ and 7.79 mm^{-1} . The solid line represents the logarithm trend of A'_{theo} and the dotted line represents the logarithm trend of A_{exp} .

Comparing A'_{theo} with A_{exp} in Figure 6.5, there is little difference over most of the scattering coefficients. This effectively validates that the opto-physiological model can predict the scattering effect on absorbance. In addition, the validation proves the MC simulation can provide a reliable environment to simulate the light propagation in tissue in IPPG and generate accurate MPL' based upon the tissue model with properties close to those in the experiment.

The relationship between A'_{theo} and A_{exp} of the one-layered phantoms with different absorption coefficients μ_a are presented in Figure 6.6.

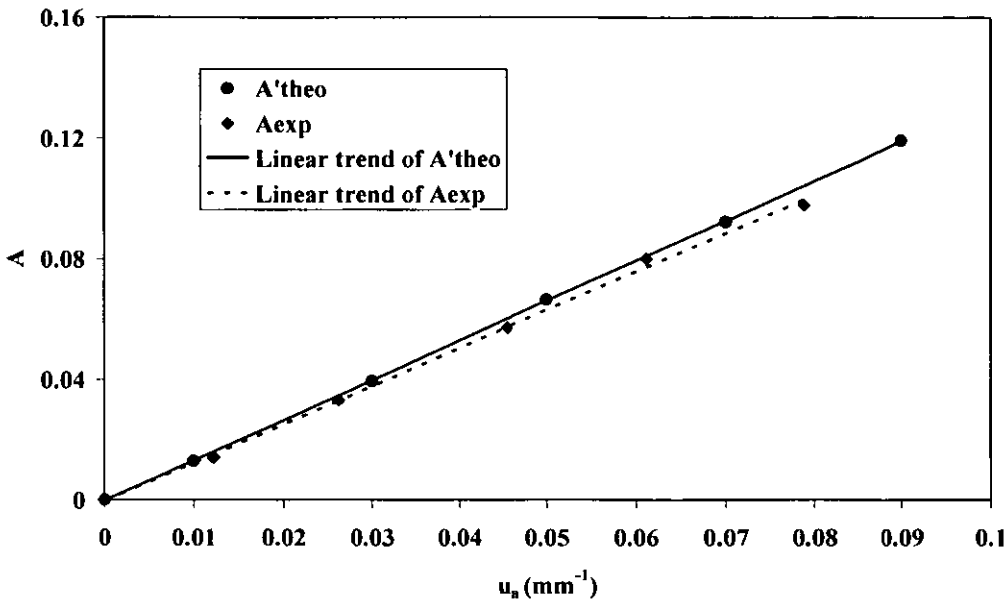


Figure 6. 6 Results of A'_{theo} and A_{exp} of the one-layered phantoms with different μ_a . The scattering coefficient μ_s was set to 7.79 mm^{-1} . The round blocks represent A'_{theo} corresponding to $\mu_a = 0, 0.01, 0.03, 0.05, 0.07$ and 0.09 mm^{-1} , and the square blocks represent A_{exp} corresponding to $\mu_a = 0, 0.0122, 0.02625, 0.0455, 0.0612$ and 0.0789 mm^{-1} . The solid line represents the linear trend of A'_{theo} and the dotted line represents the linear trend of A_{exp} .

In the opto-physiological model, when the scattering effect and thus MPL' is constant, the absorbance of tissue is solely determined by the absorption coefficient. The high correlation between A'_{theo} and A_{exp} in Figure 6. 6 validates this assumption well and proves the opto-physiological model can predict the absorbance over most of the absorbance range. Both of the absorbance from the experiments and the opto-physiological model show a linear function of μ_a . The greatest deviation from this linearity occurs at the highest absorption coefficient. This deviation comes from the underestimation of μ_a due to the spectrometer without sufficient sensitivity in high values when it was used to measure the absorbance of the dye-gelatin sample to calculate $\mu_{a,dye-gelatin}$ in Equation [5. 4].

6.2 VALIDATION BASED ON MULTI-LAYERED PHANTOM

Following the validation of the opto-physiological model in a simplified single-layered format, the two-layered phantom was prepared for the *in-vitro* experiment to validate the model in a multi-layered format.

6.2.1 Results of Experiment

6.2.1.1 Experimental protocol

The engineering setup was identical to that of the experiment based on the one-layered phantom. The two-layered phantom consisted of a top layer with low scattering and low absorption coefficient and a bottom layer with high scattering as shown in Figure 6. 7.



Figure 6. 7 An example of the two-layered phantom with a top layer with low scattering and low absorption coefficient and a bottom layer with high scattering.

The preparation of the two-layered phantom follows three steps and all the coefficients were calculated from Equation [6. 1] and [6. 2]:

- Firstly, the bottom layer was prepared following the steps of the one-layered phantom preparation described in the last section. The scattering coefficients $\mu_{s,bottom}$ of the bottom layer were maintained constant as 7.79 mm^{-1} and the absorption coefficients $\mu_{a,bottom}$ were prepared to 0.0122, 0.0263, 0.0455, 0.0612 and 0.0789

mm^{-1} respectively, by changing the concentrations of dye solution in the bottom layer;

- Two liquid mixtures were prepared for the top layer: a mixture of dye and gelatine with non-scattering $\mu_{s,top}=0 \text{ mm}^{-1}$ and low absorption coefficient $\mu_{a,top}=0.0263 \text{ mm}^{-1}$, and a mixture of milk, dye and gelatine with low scattering coefficient $\mu_{s,top}=0.779 \text{ mm}^{-1}$ and low absorption coefficient $\mu_{a,top}=0.0263 \text{ mm}^{-1}$;

- The water-milk-dye-gelatine mixture was then poured on top of the solidified bottom layer. The two-layered mixture was placed in the refrigerator to solidify for 2 hours. The geometries of both the two layers are nearly identical, i.e. $100 \times 60 \times 10 \text{ mm}^3$.

The experiment was performed following the same protocol of the experiment based on the one-layered phantom. The absorbance A_{exp} of the two-layered phantom can thus be calculated from Equation [6. 3].

6.2.1.2 Experimental Results and Discussion

The relationship between A_{exp} and the bottom absorption coefficients $\mu_{a,bottom}$ of the two-layered phantom with the dye-gelatine top layer ($\mu_{s,top}=0 \text{ mm}^{-1}$, $\mu_{a,top}=0.0263 \text{ mm}^{-1}$) is presented in Figure 6. 8. A_{exp} of the experiments based on the one-layered phantom is also presented for comparison.

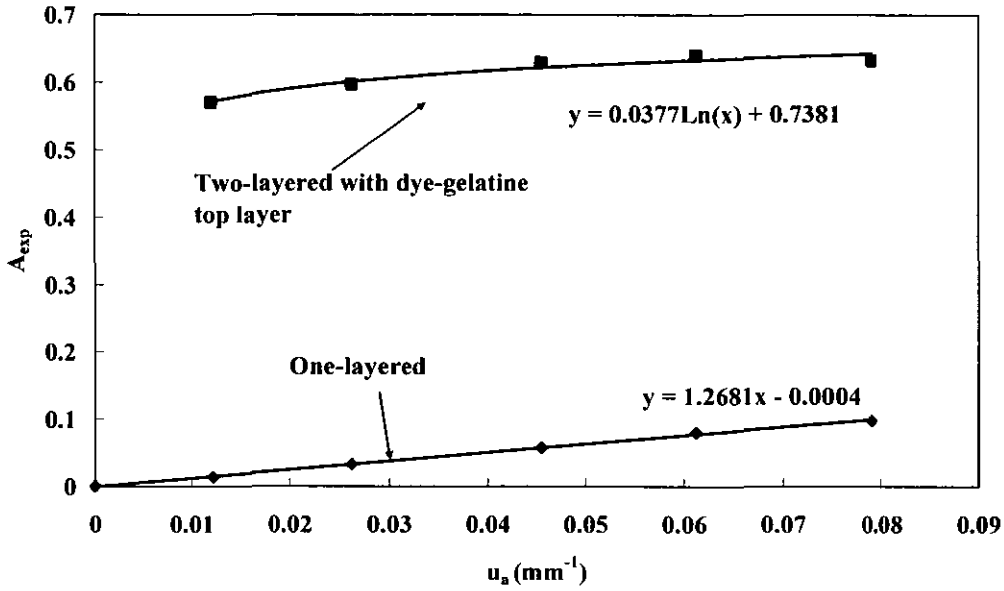


Figure 6. 8 Experimental results of A_{exp} of the one-layered phantom and two-layered phantom with dye-gelatine top layer. The square blocks represent A_{exp} of the two-layered phantoms corresponding to $\mu_{a,bottom}=0, 0.0122, 0.02625, 0.0455, 0.0612$ and 0.0789 mm^{-1} . The solid curve is the logarithm trend of these square blocks. The diamond blocks represent A_{exp} of the one-layered phantoms corresponding to the above absorption coefficients. The straight line is the linear trend of the triangle blocks.

Figure 6. 9 illustrates the relationship between A_{exp} and $\mu_{a,bottom}$ of the two-layered phantom with the milk-dye-gelatine top layer ($\mu_{s,top}=0.779 \text{ mm}^{-1}$, $\mu_{a,top}=0.0263 \text{ mm}^{-1}$), together with the results of the experiments based on the one-layered phantom.

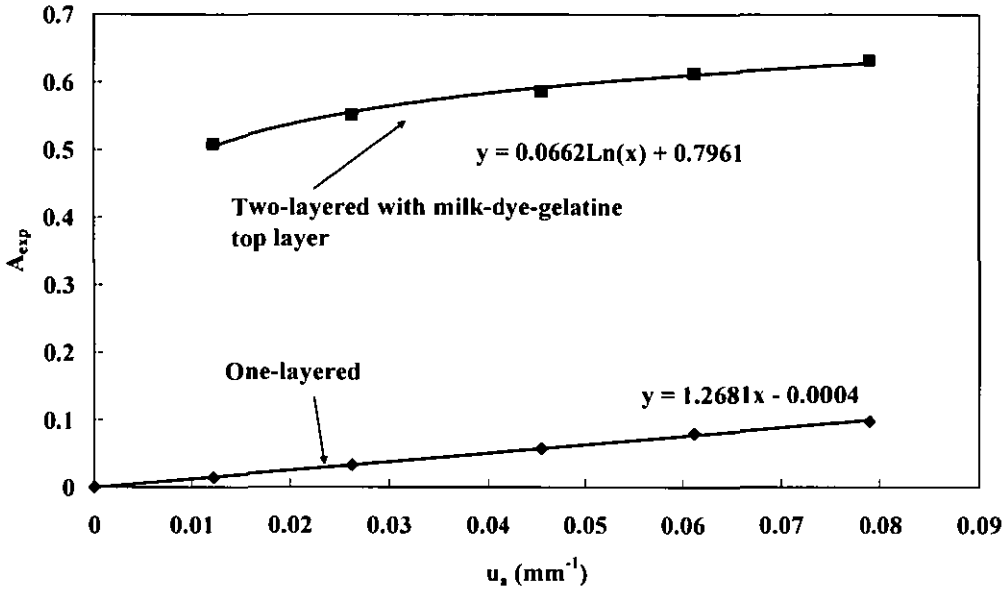


Figure 6. 9 Experimental results of A_{exp} of the one-layered phantom and the two-layered phantom with milk-dye-gelatine gel on top. The square blocks represent A_{exp} of the two-layered phantoms corresponding to $\mu_{a,bottom}=0, 0.0122, 0.02625, 0.0455, 0.0612$ and 0.0789 mm^{-1} . The solid curve is the logarithm trend of these square blocks. The diamond blocks represent A_{exp} of the one-layered phantoms corresponding to the above absorption coefficients. The straight line is the linear trend of the diamond blocks.

In Figure 6. 8 and Figure 6. 9, A_{exp} of the two-layered phantom performs a non-linear function of the absorption coefficients rather than the linear function from the experiment based upon the one-layered phantom. When comparing A_{exp} of the two-layered phantom with that of the one-layered phantom, there is a significant increase in the absorbance of the two-layered phantom developing from the absorbance of the additional top layer.

6.2.2 Results of Simulation

6.2.2.1 Simulation setup

All aspects of simulation setup were similar to that of the simulation based on the one-layered phantom model. The geometry of the model consisted of two layers, each with the dimensions of $100 \text{ mm} \times 60 \text{ mm} \times 10 \text{ mm}$ defined by the size of the actual two-layered phantom. To simulate the actual phantom, the absorption and scattering

coefficients of the top layer were set to either $\mu_{s,top}=0 \text{ mm}^{-1}$, $\mu_{a,top}=0.0263 \text{ mm}^{-1}$ or $\mu_{s,top}=0.779 \text{ mm}^{-1}$, $\mu_{a,top}=0.0263 \text{ mm}^{-1}$. For the bottom layer, the scattering coefficient $\mu_{s,bottom}$ was set to 7.79 mm^{-1} , and the absorption coefficients $\mu_{a,bottom}$ were set to lie between 0.01 and 0.1 mm^{-1} . The anisotropy g for both layers was set to 0.72 and the refractive index n was to 1.41. The surface and internal reflection was disregarded.

6.2.2.2 Simulation Results and Discussion

The aperture-dependent MPL' for each layer was calculated by Equation [4. 6] following the procedure of the post data processing of the simulation in section 4.2 based on the above two-layer phantom model. Figure 6. 10 illustrates the relationship between absorption coefficients on MPL' of both the top and bottom layers. The simulation was performed on the two-layered phantom model with non-scattering and low-absorption layer on top, i.e. $\mu_{s,top}=0 \text{ mm}^{-1}$ and $\mu_{a,top}=0.0263 \text{ mm}^{-1}$. The MPL' of the simulation based on the one-layered phantom is also presented as a reference.

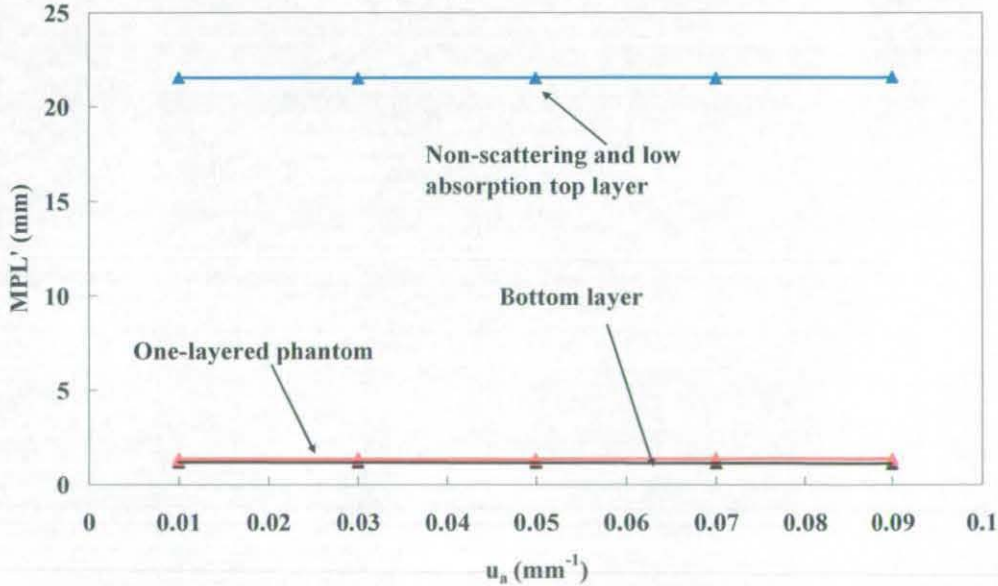


Figure 6. 10 The simulation results of MPL' of the one-layered and the two-layered phantom model with the non-scattering top layer. The red blocks represent MPL' of the one-layered phantom model corresponding to different absorption coefficients $\mu_{a,one-layered}=0.01, 0.03, 0.05, 0.07$ and 0.09 mm^{-1} . The black blocks represent MPL' of the bottom layer of the two-layered phantom model corresponding to the same

absorption coefficients. The blue blocks represent MPL' of the top layer $\mu_{s,top}=0$ mm^{-1} , $\mu_{a,top}=0.0263$ mm^{-1} .

Figure 6. 11 presents MPL' of the top layer and the bottom layer respectively yielded by the simulation on the two-layered phantom model consisting of low-scattering and low absorption top layer, i.e. $\mu_{s,top}=0.779$ mm^{-1} and $\mu_{a,top}=0.0263$ mm^{-1} , together with the MPL' by simulation based on the one-layered phantom.

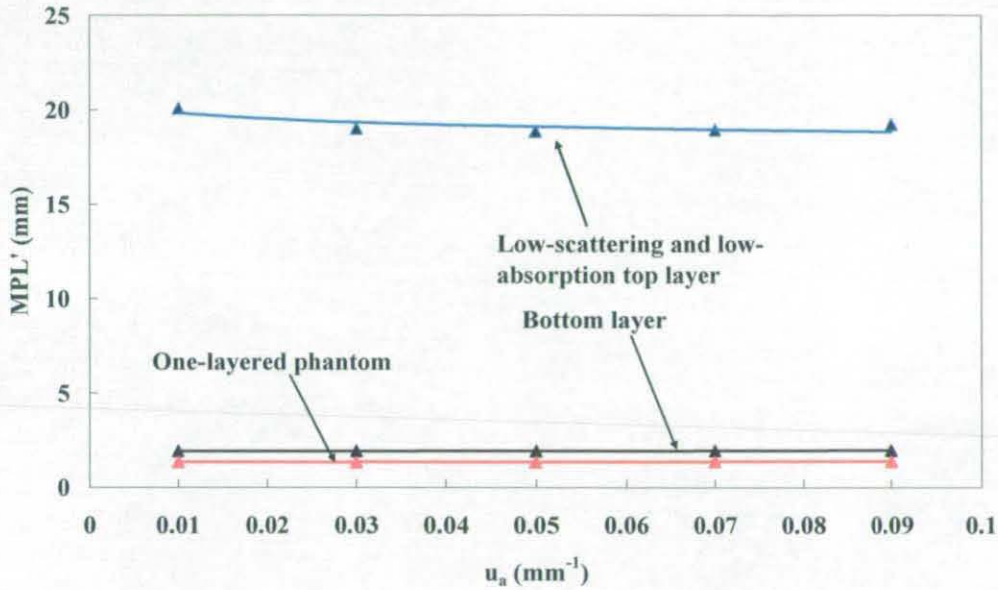


Figure 6. 11 The simulation results of MPL' of the one-layered and the two-layered phantom model with the low-scattering and low-absorption top layer. The red blocks represent the MPL' of the one-layered phantom model corresponding to $\mu_{a,one-layered}=0.01, 0.03, 0.05, 0.07$ and 0.09 mm^{-1} . The black blocks represent MPL' of the bottom layer of the two-layered phantom model corresponding to the same absorption coefficients. The blue blocks represent MPL of the top layer $\mu_{s,top}=0.779$ mm^{-1} , $\mu_{a,top}=0.0263$ mm^{-1} .

The simulation results of MPL' on the two-layered phantom model in Figure 6. 10 and Figure 6. 11 demonstrate little variation with the change of μ_a , which is in accordance with the simulation results on the one-layered phantom model. MPL of the top layer with either low-scattering or non-scattering coefficients is nearly two times the thickness of the top layer, i.e. $20mm$. This indicates that when the scattering is small, the light propagation is mainly forward-directed.

In Figure 6. 10, when the top layer is non-scattering, MPL of the bottom layer is smaller than that of the one-layered model. This is due to the limitations of the

simulation using OptiCAD. In the construction of the tissue model, the small spaces between layers are required by OptiCAD. Although the differences of refractive index between layers are set to be negligible, the refractive index change still exists among these small spaces. Thus the light experiences a small refraction when travelling between layers, which results in the variation of MPL between one-layered and two-layered phantom model. On the other hand, when the scattering coefficient $\mu_{s,t}$ of the top layer increases, MPL of the bottom layer is longer than that of the one-layered model as shown in Figure 6.11. When the top layer is a scattering medium, the light penetrates into the next layer with an ambient incident angle, which results in a considerable effect on the path length.

6.2.3 Validation Analysis

Based on the opto-physiological model, the absorbance A'_{theo} was calculated following Equation [5. 7] in a two-layered format:

$$A'_{theo} = \mu_{a,top} \times MPL'_{aperture,top} + \mu_{a,bottom} \times MPL'_{aperture,bottom} \quad [6. 5]$$

where $\mu_{a,top}$ and $\mu_{a,bottom}$ are the wavelength-dependent absorption coefficients of top and bottom layer, and $MPL'_{aperture,top}$ and $MPL'_{aperture,bottom}$ are the aperture-dependent mean path length of top and bottom layer as shown in Figure 6. 10 and Figure 6. 11.

A'_{theo} and A_{exp} of the two-layered phantom with non-scattering layer on top are presented in Figure 6. 12.

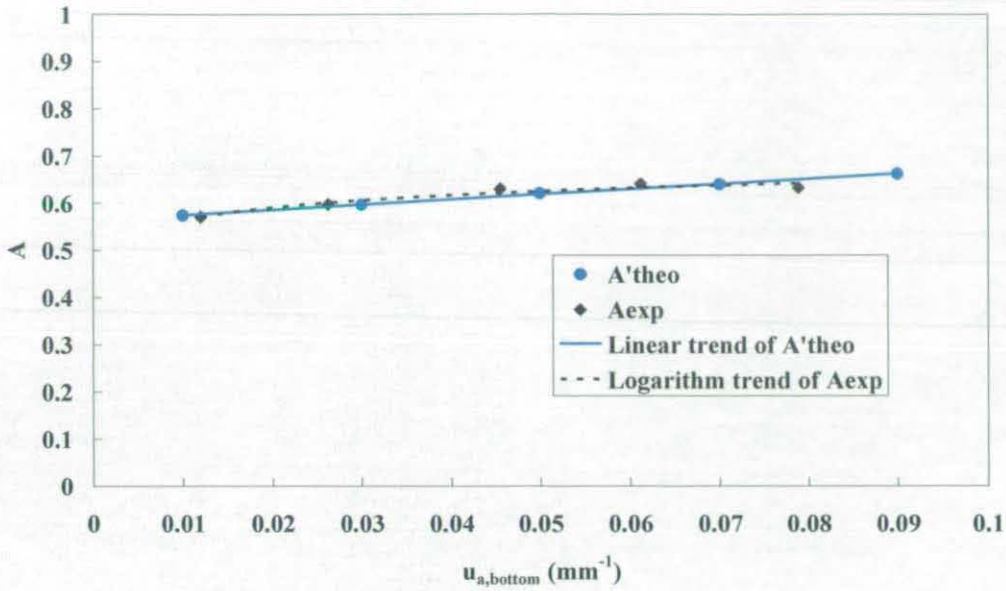


Figure 6. 12 Results of A'_{theo} and A_{exp} on the two-layered phantom with the non-scattering layer on top with $\mu_{s,top}=0 \text{ mm}^{-1}$, $\mu_{a,top}=0.0263 \text{ mm}^{-1}$. The round blocks represent A'_{theo} corresponding to different $\mu_{a,bottom}=0, 0.01, 0.03, 0.05, 0.07$ and 0.09 mm^{-1} and the diamond blocks represent A_{exp} corresponding to different $\mu_{a,bottom}=0, 0.0122, 0.0263, 0.0455, 0.0612$ and 0.0789 mm^{-1} . The solid line represents the linear trend of A'_{theo} and the dotted curve represents the logarithm trend of A_{exp} .

In Figure 6. 12, A'_{theo} demonstrates a linear function of the absorption coefficients same with the results of the one-layered phantom. The slope varies a little bit from that of the one-layered phantom due to the refractive index change of the inter-layer spaces. However, as the absorbance still performs a linear trend, the effect of the refractive index change can be considered to be stable and controllable. Compared to the results of the one-layered phantom model, there is a significant increase in absorbance of the two-layered phantom, due to the absorbance of the additional top layer.

Figure 6. 12 illustrates relatively good correlation between the results of the opto-physiological model and the experiments. There are small deviations due to the refractive index change between layers in simulation. Nevertheless, the deviation is not significant, thus the opto-physiological model can still be regarded as accurately predicting the absorbance in the two-layered phantom with the non-scattering top layer.

A'_{theo} and A_{exp} of the two-layered phantom with low-scattering top layer are presented in Figure 6. 13.

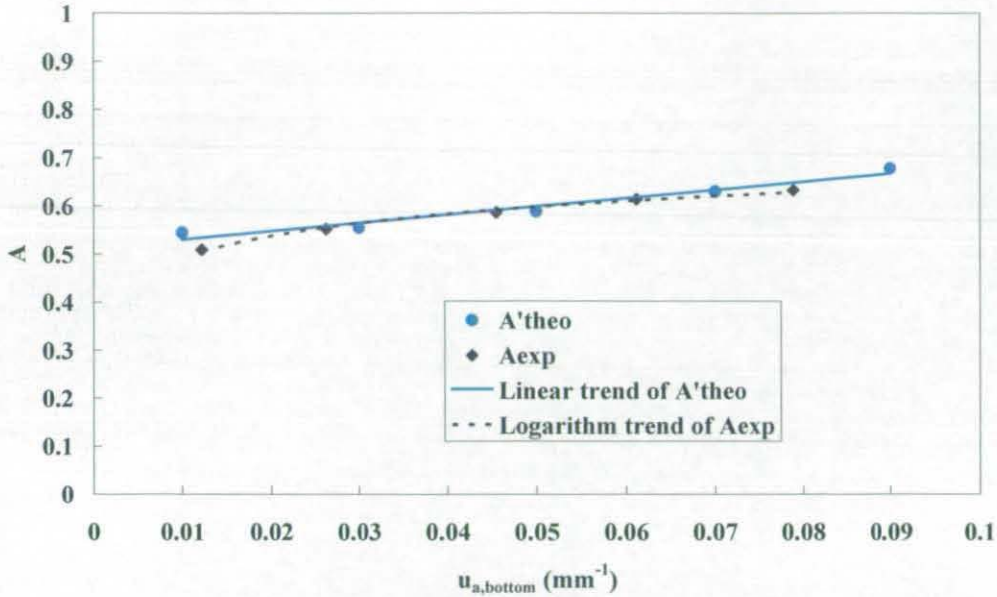


Figure 6. 13 Results of A'_{theo} and A_{exp} on the two-layered phantom with the low-scattering layer on top $\mu_{s,top}=0.779 \text{ mm}^{-1}$, $\mu_{a,top}=0.0263 \text{ mm}^{-1}$. The round blocks represent A'_{theo} corresponding to $\mu_{a,bottom}=0, 0.01, 0.03, 0.05, 0.07$ and 0.09 mm^{-1} and the diamond blocks represent A_{exp} corresponding to $\mu_{a,bottom}=0, 0.0122, 0.0263, 0.0455, 0.0612$ and 0.0789 mm^{-1} . The solid line represents the linear trend of A'_{theo} and the dotted curve represents the logarithm trend of A_{exp} .

In Figure 6. 13, A'_{theo} performs an approximate linear function of the absorption coefficients. There is a significant increase in the absorbance of the two-layered phantom, due to the absorbance of the top layer. Also there is an increase of the slope from two-layered phantom model compared to that from one-layered phantom model. This is due to the scattering effect of the top layer as discussed previously. There is some small deviation from this linearity. When the incident light penetrates into the bottom layer with an arbitrary incident angle, the effect on mean path length and total absorbance is random. However, this random effect is not significant enough to affect the whole propagation tendency. Thus it is reasonable to assume the linearity relationship between the absorbance and the multi-layered absorption coefficient.

The relatively high correlation between the absorbance of opto-physiological model and the experiment in Figure 6. 12 and Figure 6. 13 indicates that the

opto-physiological model predicts the absorbance over most of the ranges. When scattering is constant, the absorbance of the phantom can be regarded as a linear function of the multi-layered absorption coefficient.

In the validation on one-layered and two-layered phantoms, the output of the opto-physiological model and the experiment highly correlate when the properties of the phantom model in simulation approach those occurring in the actual phantom. This correlation proves the feasibility and applicability of the methodology of this thesis, in which the MC simulation provides a reliable environment to simulate the light-tissue interaction underlying IPPG and generate accurate *MPL* for the opto-physiological model. The model not only can accurately predict the output in the range of μ_a and μ_s close to human tissue, but also predict the effect of changes of μ_a and μ_s on the output.

6.3 SUBJECT-BASED VALIDATION

The opto-physiological model with the MC simulation was validated *in-vitro* to evaluate the performance of simulation platform and the accuracy of the model in a controlled environment. This section moves onto the *in-vivo* validation based upon experiments performed on healthy subjects and corresponding simulation on the multi-layered tissue model to imitate human skin.

Similar to the phantom-based validation, the experimental results serve as a reference for the validation of the opto-physiological model. In the subject-based validation, the ratio R of the static and dynamic components in both the experiment and the simulation are compared as introduced previously about the *in-vivo* validation analysis in section 5.2.2.3. According to Equation [5. 11], the experimental R_{exp} largely relies on the mean amplitude ac of the dynamic AC signal and mean value dc of the static DC signal. Thus the quality of IPPG signals directly affects the accuracy of the validation. The performance of the current IPPG system needs to be evaluated in reliability to deliver quality signals. Owing to the cardiac rhythm, the absorption of light due to the haemoglobin in blood, increasing during systole and decreasing during diastole, results in the dynamic AC signal containing numerous cardiac-vascular information. These measurements of cardiac-vascular

parameters such as heart rate provide an effective and straight-forward way to evaluate the performance of the current IPPG system. In this section, the performance was assessed by comparing the PPG signal from a conventional PPG sensor and IPPG system in both time domain and frequency domain. The experiments for reliability in statistics were performed on 8 healthy subjects to compare the heart rate derived from convention PPG sensor and IPPG system. The similar approach can also be found in previous research to evaluate the hardware [33].

6.3.1 Display of PPG waveform

6.3.1.1 Experimental protocol

An IPPG system was configured to capture signals under illumination with a dual-wavelength RCLED ring light at two different wavelengths of 650nm and 870nm in a remote reflection mode. Both the CCD camera and CMOS camera were employed for this protocol. The CMOS camera was configured to capture at a speed of 16*fps* and CCD camera at 15*fps*. A conventional PPG system (DISCO4, Dialog Devices Ltd., UK) was employed to provide the reference signals to compare with IPPG signals. The custom LabVIEW control software of DISCO4 is detailed in Appendix III. The output power of the ring light for each wavelength reached 8mW by setting the forward current for each RCLED as 20mA of 650nm and 10mA of 870nm. A trigger signal was sent simultaneously to the camera system and the conventional PPG data acquisition system, initiating a 10s capture of data by both.

A healthy male and female subject participated in this study and the experimental protocol was performed in a dark room. The male subject was requested to sit in an upright position with his right hand resting on a cushioned bench under the CMOS camera; the female subject was requested to perform the experiment in an upright position with her face opposite the CCD camera. The camera with the lens surrounded by the ring light was positioned and focused on the subject's designated area for each posture: the palm of the right hand and the forehead as shown in Figure 6. 14. A conventional transmission mode pulse oximetry probe (P861RA, ViaMed,

UK) connected to the DISCO4 PPG board was attached to the subjects' left index finger.

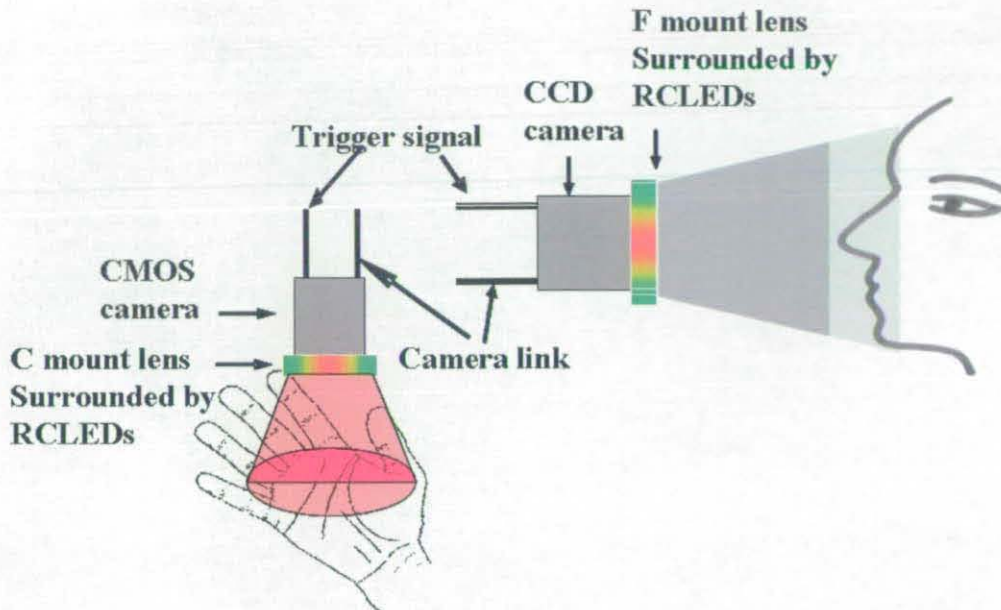


Figure 6. 14 A schematic diagram of the experimental setup and protocol.

The off-line processing follows the procedure of post data processing as shown in Figure 5. 7 and Figure 5. 12 in section 5.2.1 and section 5.2.2.1. The size of each ROI of 20×20 pixel² was chosen to derive IPPG signals from each set of frames for each posture and wavelength.

6.3.1.2 Experimental Results and discussion

The *AC* signals of the male hand from IPPG and conventional PPG are presented in Figure 6. 15 . The detected IPPG signal corresponds to the received light intensity. The upwards slope represents the diastole phase and the downwards slope the systole phase. The presence of a second, smaller pulse within an arterial pulsation, called dicrotic notch ^[86], represents closure of the aortic valve at the onset of ventricular diastole.

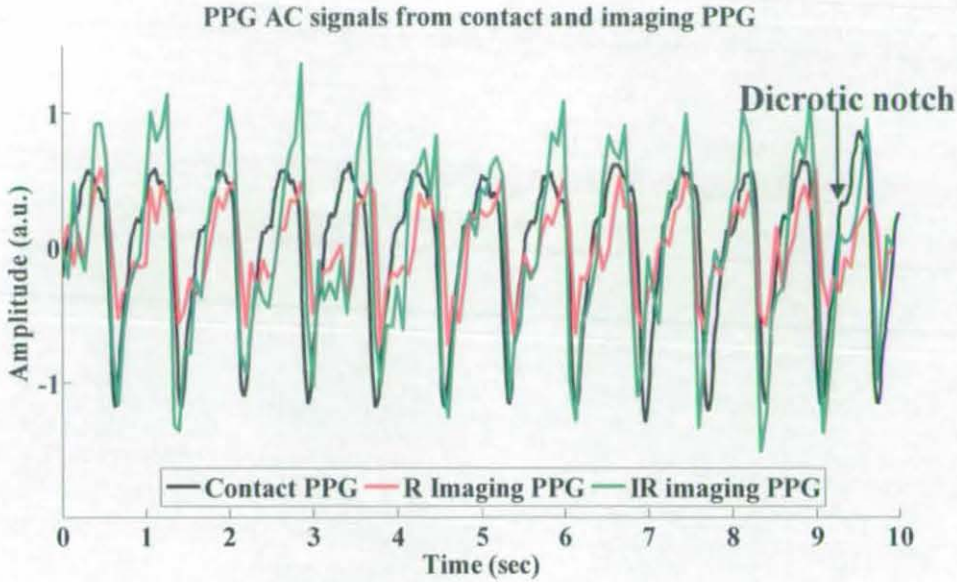


Figure 6. 15 The PPG AC signals in time domain of the male subject's hand from the conventional contact PPG and IPPG using CMOS camera under 650nm and 870nm illumination.

The PPG dynamic information such as the oscillations for heart rate is clearly indicated in Figure 6. 15 . The profiles of IPPG *AC* signals are clearly recognised in accordance with those of the contact PPG signal. The IPPG system demonstrates increased sensitivity to the dicrotic notch. Originated from the same heartbeat, different shape and amplitude of the IPPG *AC* signals are observed from the outputs illuminated by the two different wavelengths. This phenomenon may come from the different spectral sensitivity of the camera at the two wavelengths, and also the different penetration depths depending on the emitter wavelength.

Figure 6. 16 presents the *AC* signals of the female forehead from IPPG and conventional PPG. In Figure 6. 16, the characteristics of the IPPG *AC* signal are clearly identified with the contact PPG signal.

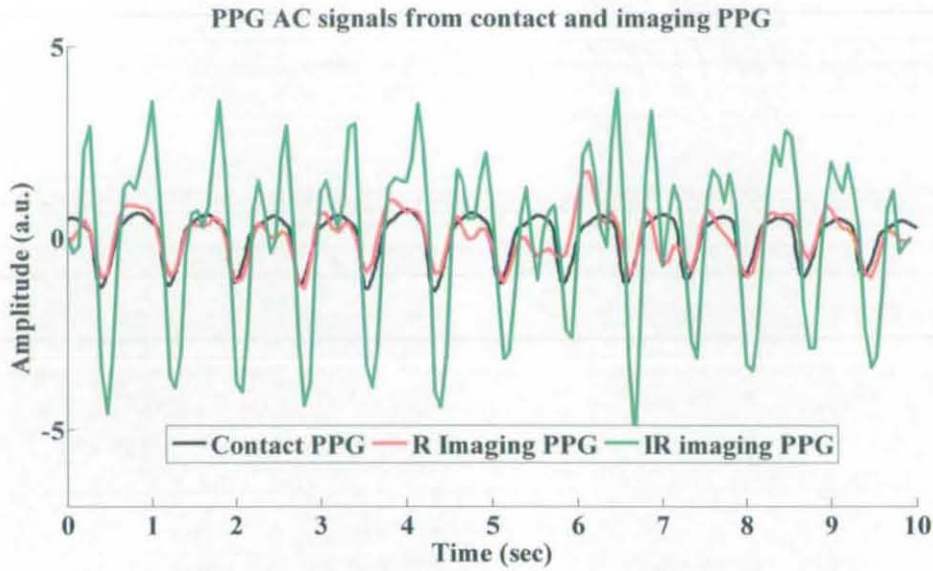


Figure 6. 16 The PPG *AC* signals in time domain of the female subject's face from contact PPG and IPPG using CCD camera under 650nm and 870nm illumination.

Attention should be drawn to the phenomenon that the dicrotic notch under 650nm illumination consistently appears at the opposite position to that under 870nm illumination in Figure 6. 16. This phenomenon does not occur in Figure 6. 15 . This might be due to the different underlying physiological mechanism in the hand and forehead, which needs further investigation.

6.3.2 Cardiac-Vascular parameters

6.3.2.1 Experimental protocol

Based upon the above *AC* signals, Fast Fourier transforms ("FFT" in Matlab) were performed to determine the spectra of these signals. A custom short-time frequency transform ("STFT" in Matlab) was performed to present the spectrogram in both the time-based and frequency-based views of the *AC* signal. The spectrogram can provide visualized information about both when and at what frequencies a signal event occurs.

6.3.2.2 Experimental Results and discussion

The Fourier spectra and the time-frequency spectrograms are plotted in Figure 6. 17 corresponding to the *AC* signals from the CMOS camera in Figure 6. 15 .

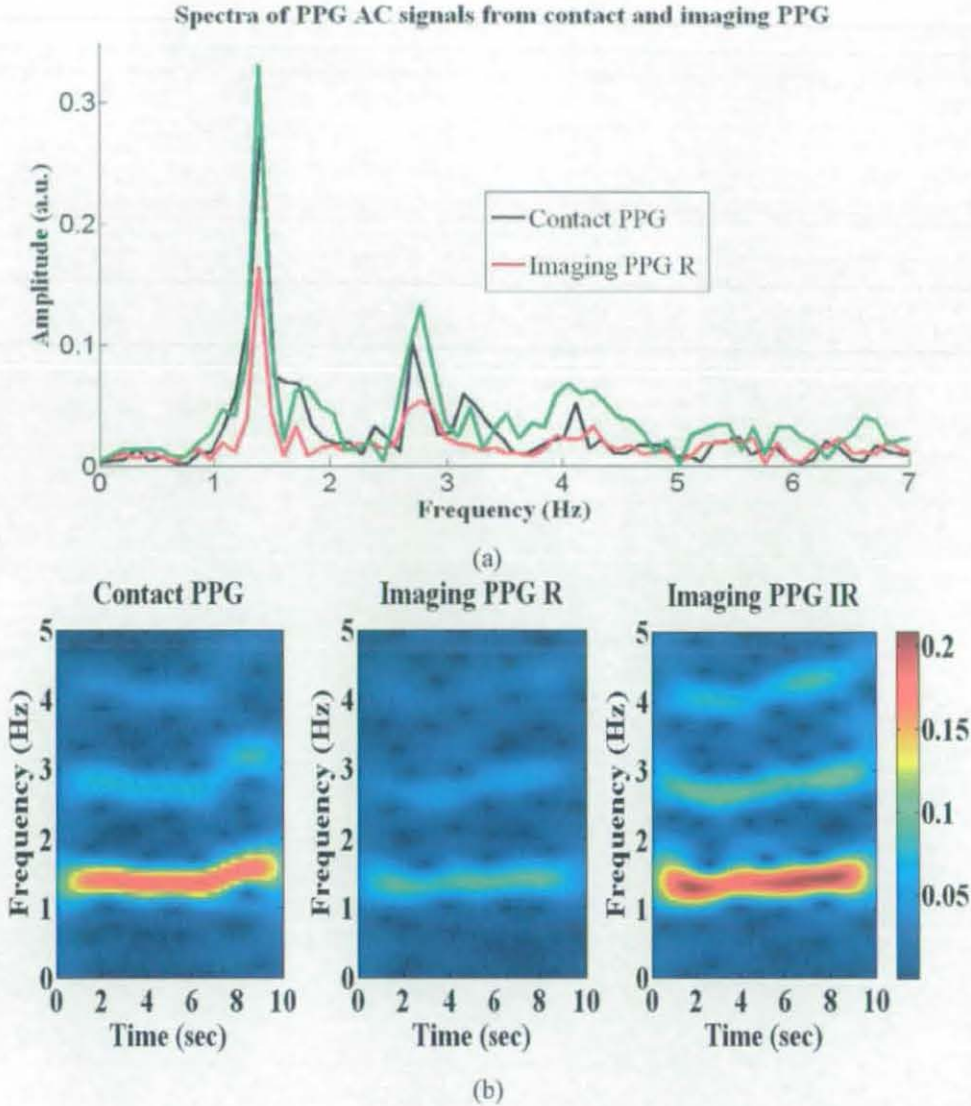


Figure 6. 17 The Fourier spectra (a) and time-frequency spectrograms (b) for AC signals from contact PPG and IPPG under 650nm and 870nm illumination from the hand.

The fundamental heart rate (HR) frequency is clearly visible in all spectra around 1.4 Hz^[4], which is 1.409Hz for contact PPG signals and 1.387 Hz for IPPG signals. The fundamental HR frequency of IPPG AC signals can be clearly identified in Figure 6.17(a) and (b). The 2nd and 3rd harmonics of the AC signal under 870nm illumination can even be recognised in both Fourier spectrum and the time-frequency spectrogram. The detection of the harmonics indicates that both the heart rate and the shape of the waveform can be determined.

Figure 6. 18 illustrates the Fourier spectra and the time-frequency spectrograms of the AC signals from the CCD camera in Figure 6. 16.

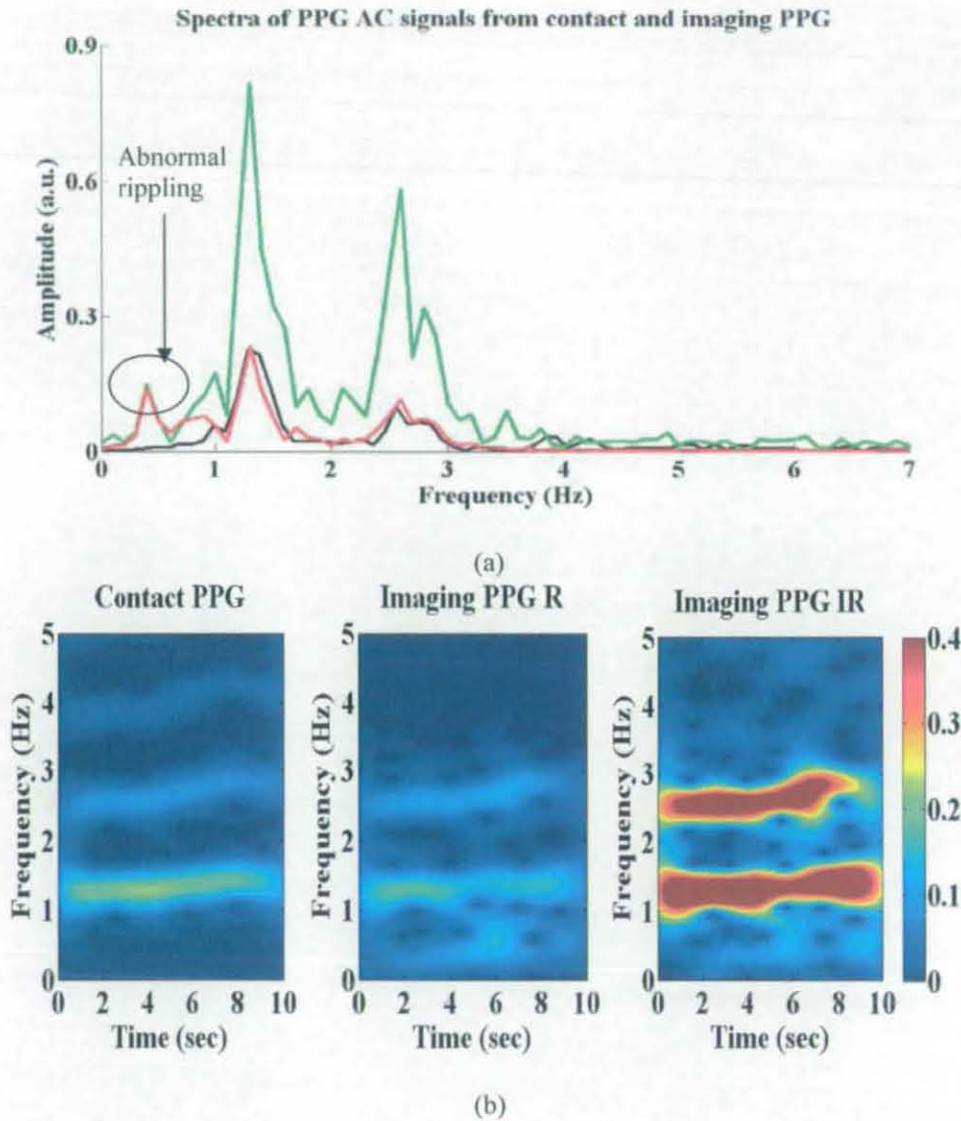


Figure 6. 18 The Fourier spectra (a) and time-frequency spectrograms (b) for AC signals from contact PPG and IPPG under 650nm and 870nm illumination from the face.

In Figure 6. 18, the fundamental HR frequency is identical of the contact PPG signal and that of IPPG signals 1.3Hz. These results demonstrate the comparability of IPPG in displaying the dynamic waveform with a conventional contact PPG instrument and exhibit the system with the capability of obtaining quality PPG AC signals from different tissue areas of human subjects. There is abnormal rippling in the low frequency range of the IPPG signal in Figure 6. 18 (a), which does not appear in the

contact PPG signal. The spectrograms in Figure 6. 18 (b) clearly demonstrate this rippling occurs at the time of about 6sec. Referring to the Figure 6. 16 of these signals in time domain, the profiles of the signals especially at 650nm illumination are truly not clearly recognised at this period of time. Physiological signals such as IPPG signal are generally transient, so the usage of the Fourier transform sometimes leads to ambiguous results. Combining the Fourier transform and the time-frequency analysis can give a more comprehensive analysis in Frequency domain for the IPPG signal.

6.3.3 Reliability

6.3.3.1 Experimental protocol

Eight healthy Chinese subjects (3 females, 5 males) participated in this study and all subjects gave their informed consent to participate in the study. The experimental protocol was performed in a dark room. The subjects were requested to sit in an upright position with their head resting on a bench. A conventional transmission mode pulse oximetry probe connected to the DISCO4 PPG board was attached to the subjects' right index finger. The CCD camera was chosen for this investigation as the fundamental HR frequency of the IPPG *AC* signal was found to be more significant in the previous section. The camera with the ring light was positioned 130 mm from the face and focused on the subjects' forehead. The camera was configured to capture at 30fps. A trigger signal was sent simultaneously to the camera system and the PPG board, initiating a 10s data acquisition in both systems.

The pulse rate *PR* (beat/minute) can be calculated as:

$$PR = 60 \times \frac{1}{t_{PPI}} \quad [6. 6]$$

where t_{PPI} is the mean duration of pulse-to-pulse intervals (PPI) as shown in Figure 5. 13. The pulse rate and the HR fundamental frequency from IPPG and contact PPG signals were compared to each other. Bland-Altman and correlation methods were employed to assess the level of agreement between the devices.

6.3.3.2 Results and Discussion

Figure 6. 19 shows a scatter plot of the pulse rate measurement from the contact PPG versus the measurement from IPPG. The results of contact and IPPG under 870nm measurements are plotted as circles, and those under 650nm measurements as crosses. The regression line $y=0.933x+5.22$ is plotted in Figure 6. 19, showing a high correlation ($r^2=0.932$) between the contact PPG and IPPG, while a small offset is evident from the regression line equation. The IPPG slightly overestimates the pulse rate.

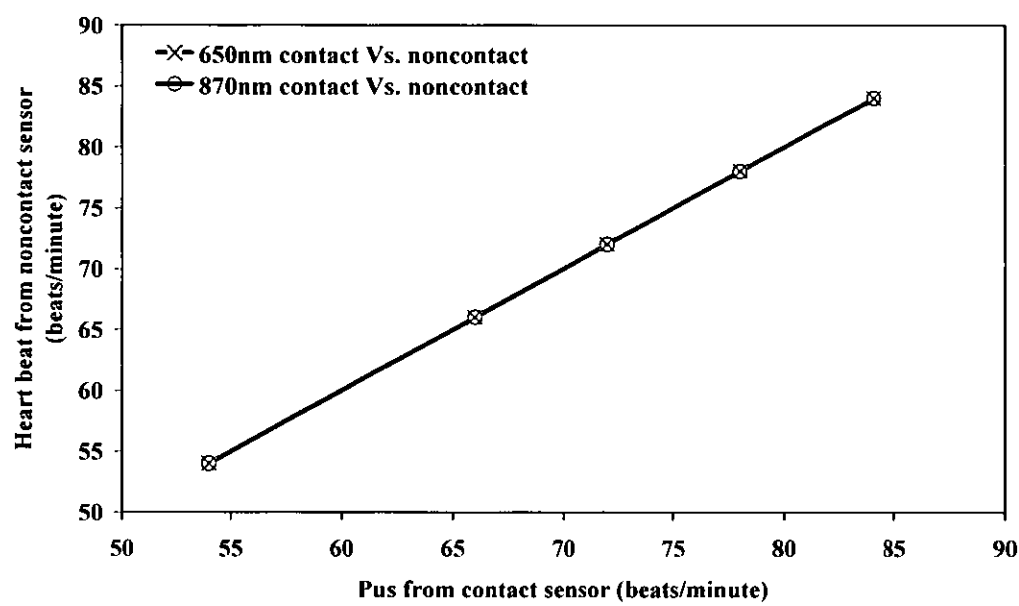


Figure 6. 19 The scatter plot showing the pulse rate from IPPG and PPG measurement at 870 nm (circles) and 650 nm (crosses) for each subject. Also shown is the line $y=0.933x+5.22$, where both methods are highly correlated.

Figure 6. 20 shows a Bland-Altman plot of the two methods by comparing the frequency difference of the cardiac component between IPPG and contact PPG, versus the mean frequency resulting from those two methods. Again data pertaining to 870nm are represented by circles and 650nm by crosses. The Bland-Altman plot^[87] is a popular method of assessing the level of agreement between a tested clinical device and a second device used as a gold standard.

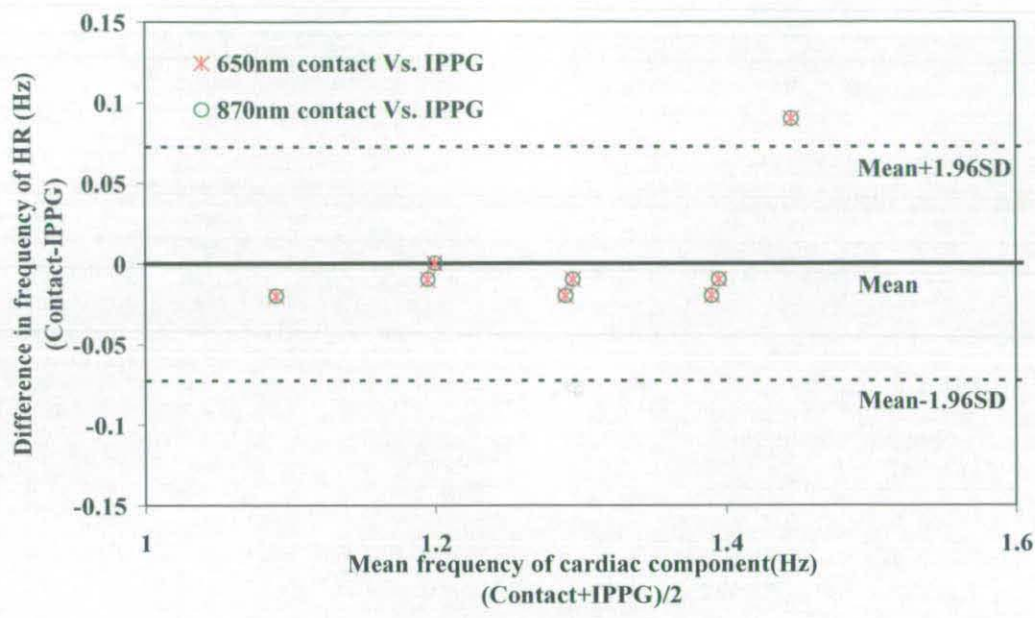


Figure 6. 20 The Bland-Altman plot, showing the frequency difference of cardiac component between IPPG and contact PPG, versus the mean frequency resulting from the two methods of measurement for each subject. The circles indicate measurements at 870nm, and the crosses at 650nm. The solid line indicates the mean frequency difference and the dotted lines represent the ± 1.96 standard deviations.

A visual inspection of the Bland-Altman plot enables to identify the type and level of error by comparison to the true value of the variable of interest. The mean frequency difference between the two techniques is -0.00125 Hz and the standard deviation (SD) is 0.0334 Hz. Assuming that the mean difference is normally distributed, the 95% confidence interval can be calculated as ± 1.96 SD, which means that pulse rate from IPPG might be 3.873 beats/minute above or 4.023 beats/minute below that from contact PPG. The insignificant mean difference means that the two methods can be used interchangeably for the measurement of pulse rate.

This study has demonstrated the reliability of the IPPG system to detect IPPG *AC* signals. Although the camera is more susceptible to ambient light and motion artefact than a conventional contact probe, the *AC* signals captured by the imaging system have still shown a strong similarity with those captured by the conventional PPG sensor in both time domain and frequency domain and deliver reliable cardiac-vascular parameters i.e. heart rate with good reliability. Thus it is ready for the *in-vivo* validation of the opto-physiological model.

6.3.4 Validation Analysis

6.3.4.1 Results of subject-based experiment

The experimental study was performed based upon the same database of the experiments in section 6.3.3. It is difficult to quantify the reflected light intensity I_{ref} in the subject-based experiment. Previous research ^[88] demonstrates polarization gating as a simple and effective method to eliminate surface reflection. It is difficult to implement this method in the current platform of IPPG as the polarizer reduces the light intensity, resulting in a critical loss of quality in the measurement of the weak AC component of IPPG signals. When assuming no surface reflection, the ratio R_{exp} of the experiment can be calculated following Equation [5. 11] as:

$$R_{exp} = \frac{ac}{dc} \quad [6. 7]$$

where ac and dc are calculated using Equation [5. 9] and [5. 10] as shown in Figure 5. 13 and Figure 5. 14. The results of R_{exp} from 8 subjects under 870nm illumination are presented in Figure 6. 21.

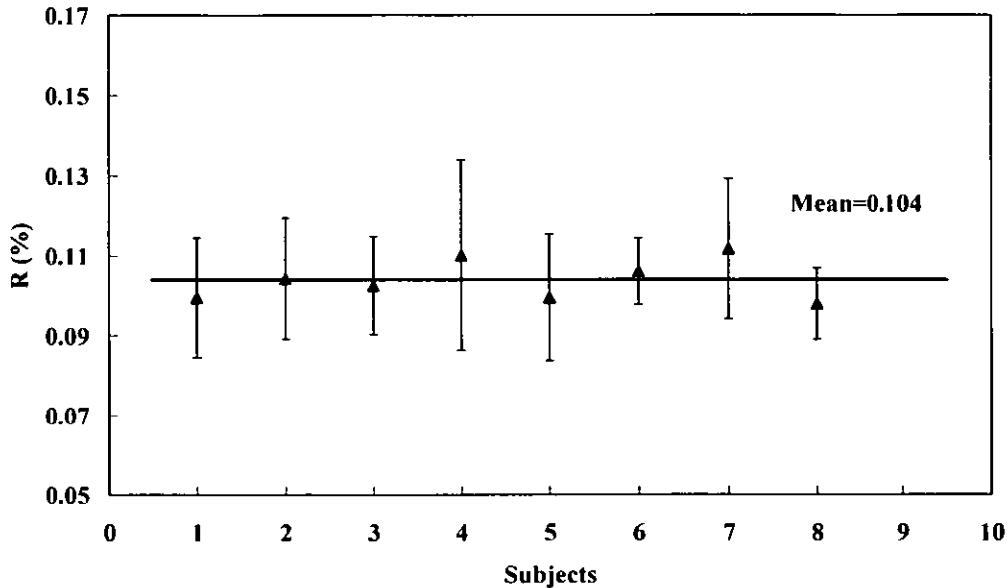


Figure 6. 21 The results of R_{exp} from 8 subjects under 870nm illumination. The triangle blocks represent the mean of R_{exp} with standard deviation for each subject. The straight line represents the mean of R_{exp} over all the subjects.

Figure 6. 21 illustrates a little variation between the mean values of R_{exp} over the 8 subjects. The variation may be due to the different surface reflection between subjects. Nonetheless, as the variation is not significant, the surface reflection and tissue properties between subjects can be regarded comparable in this controlled group. Thus one tissue model in MC simulation can represent a specific group or characterised tissue. This makes the opto-physiological model more applicable in biological tissue measurements, as it is not necessary to construct tissue models for individual subjects.

6.3.4.2 Results of skin-model-based simulation

The preparation of the six-layered tissue model has been previously described about skin tissue model in simulation in section 5.2.2.2. All tissue layers are set to be homogeneous with different blood fractions.

Light impinging upon the tissue was simulated using multiple spherical light sources each with 180 degree view angle and confined to the same arrangement as the right light in experiments in Figure 5.3. The light source was set to be 130 mm away from the surface. As introduced previously about the lens in the phantom-based simulation in section 6.1.2.1, the same double-convex lens (Dia: 30 mm, FL: 50 mm, Centre thickness: 6.55 mm, $R_1 = -R_2$: 50.67,) was selected in the subject-based simulation. The lens was positioned 130mm away from the tissue model in OptiCAD. The layered detector-dependent $MPL'_{static}(i)$ was calculated by Equation [4. 6] following the procedure of post data processing of the simulation in section 4.2. This simulation was based on the skin tissue model with the optical properties of non-pulsatile tissue in Table 6.1 corresponding to the static stage. The dynamic stage was simulated with the optical properties of pulsatile tissue in Table 6.1. Consequently, layered $MPL'_{dynamic}$ was calculated using Equation [4. 7] based on the skin tissue model in both the static and dynamic stage.

Following above, the MPL' of each tissue layer are listed in Table 6.2, including the static component static component MPL'_{static} and the dynamic component $MPL'_{dynamic}$.

| Layer | static(mm) | dynamic(mm) |
|-------------------------|------------|-------------|
| Epidermis | 0.1832 | 0 |
| Dermis | 0.6499 | 0 |
| Dermis papillary plexus | 0.5101 | 0.000305 |
| Dermis | 1.8996 | 0.00196 |
| Dermis cutaneous plexus | 0.7605 | 0.000128 |
| Hypodermis | 0 | 0 |

Table 6. 1 MPL' of each tissue layer with the static component MPL'_{static} and the dynamic component $MPL'_{dynamic}$.

The MPL' in Table 6.2 presents the dynamic component of MPL' which accounts only a small portion of the total. This is due to the small portion of arterial pulsatile blood. The simulation assumed no blood pulsation in epidermis and top dermis layer, thus $MPL'_{dynamic}$ is equal to 0. The fourth dermis layer is the main contributor to both static and dynamic component of MPL' .

6.3.4.3 Validation Results

In the opto-physiological model, the ratio of the amplitude of the static and dynamic component related only to the absorption coefficient of blood and dynamic MPL . It was calculated following Equation 5. 15 as

$$R'_{theo} = \sum_{i=1}^6 [\mu_{a,blood}(i) \times MPL'_{dynamic}(i)] = 0.14\% \quad [6. 8]$$

where $MPL'_{dynamic}$ is the dynamic component of MPL' in Table 6.2.

As the surface reflection was disregarded in the experimental results, there are certainly expected deviations between R_{exp} calculated using Equation [6. 7] and R'_{theo} calculated using Equation [6. 8] as shown in Figure 6. 22.

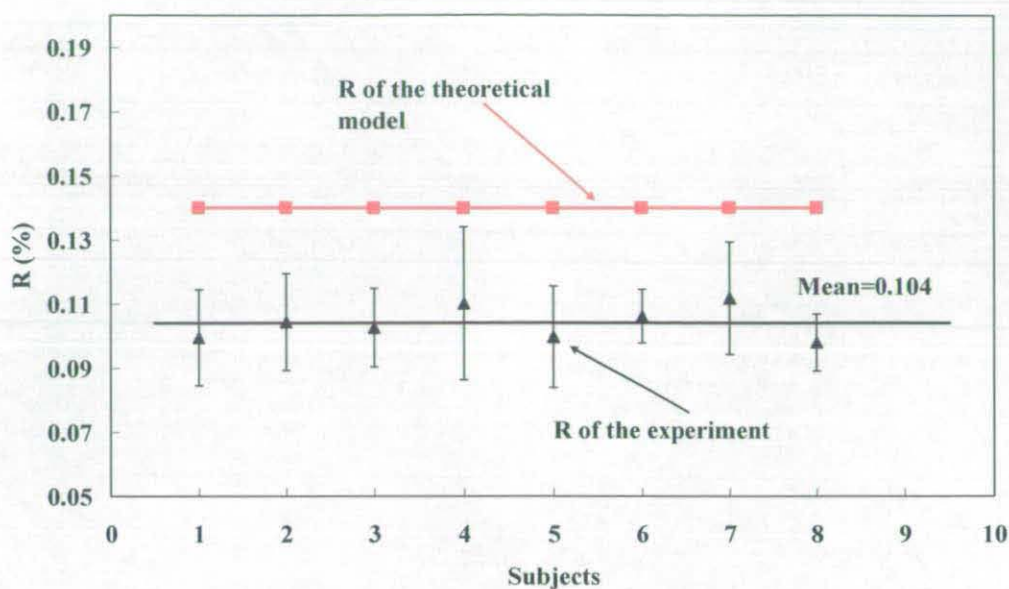


Figure 6. 22 The results of R_{exp} and R'_{theo} . The black triangle blocks represent the mean of R_{exp} with standard deviation for each subject. The red square blocks represent R'_{theo} based on the simulation of multi-layered tissue model.

Another factor that may affect the deviation is the degree of the correlation between the tissue model and the group of subjects in the experiment. The sensitivity of the current approach largely depends on the setup of the tissue model including the choice of optical properties and the definition of the tissue geometry, all of which were quoted from literature. Actually, these tissue properties may vary between people and tissue types. Thus the variation between the tissue model and real tissue could affect the above deviation. This was tested by changing the thickness of epidermis layer from 0.06 mm to 2 mm and changing the volume fraction of pulsatile blood from 0.25% to 0.15% based upon the current six-layered tissue structure. The Figure 6. 23 illustrated R_{theo} calculated from Equation 5. 15 based upon the model with thickness of epidermis layer 0.06 mm, 1 mm and 2 mm respectively.

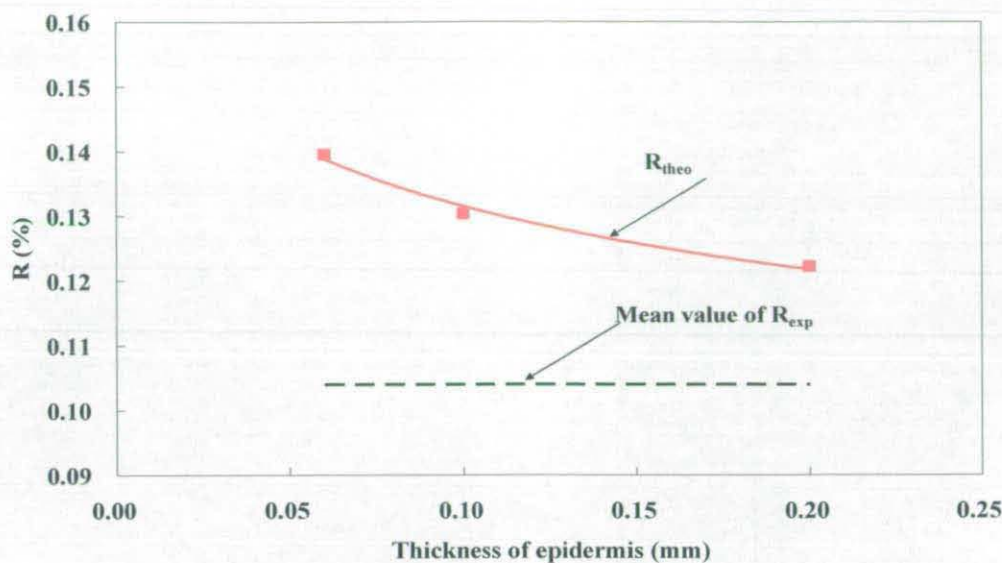


Figure 6. 23 The results of R_{theo} calculated from Equation 5. 15 based upon six-layered tissue models with different thickness of epidermis. The dotted line represents the mean value of R in the experiment. The blocks represent R corresponding to the thickness of epidermis 0.06mm (original setup), 1mm and 2mm, respectively. The curve represents logarithmic trend of these blocks.

As introduced in section 4.2, the arterial pulsation was simulated by adding the pulsatile blood into non-pulsatile tissue and thus increasing the blood volume fraction. The values of $\mu_{a,pulsatile}$ and $\mu_{s,pulsatile}$ with the volume fraction of pulsatile blood changing from 0.20% to 0.15% were calculated from Equation [5. 12] and [5. 13] as shown in Table 6. 2. Comparing to those values in Table 5.1, the decrease in total volume fraction of pulsatile blood results in the smaller pulsatile volume fraction and thus the optical properties of each layer.

| $f_{pulse}(\%)$ | 0.2 | | 0.15 | |
|-----------------------------|--------------------------------------|--------------------------------------|--------------------------------------|--------------------------------------|
| Layer | $\mu_{a,pulsatile}$ (mm^{-1}) | $\mu_{s,pulsatile}$ (mm^{-1}) | $\mu_{a,pulsatile}$ (mm^{-1}) | $\mu_{s,pulsatile}$ (mm^{-1}) |
| Epidermis (1) | 0.0245 | 4.45 | 0.0245 | 4.45 |
| Dermis (2) | 0.0245 | 4.45 | 0.0245 | 4.45 |
| Dermis Plexus (3) | 0.05558 | 10.14970 | 0.05557 | 10.14866 |
| Dermis (4) | 0.04789 | 8.73828 | 0.04786 | 8.73412 |
| Dermis Plexus Profundus (5) | 0.13836 | 25.32905 | 0.13834 | 25.32593 |
| hypodermis (6) | 0.04870 | 8.88788 | 0.048475 | 8.84633 |

Table 6. 2 The optical properties of each tissue layer of 870nm with f_{pulse} 0.20% and 0.15%.

The R_{theo} was calculated from Equation 5. 15 based upon the model with volume fraction of pulsatile blood 0.25%, 0.20% and 0.15% as shown in Figure 6. 24.

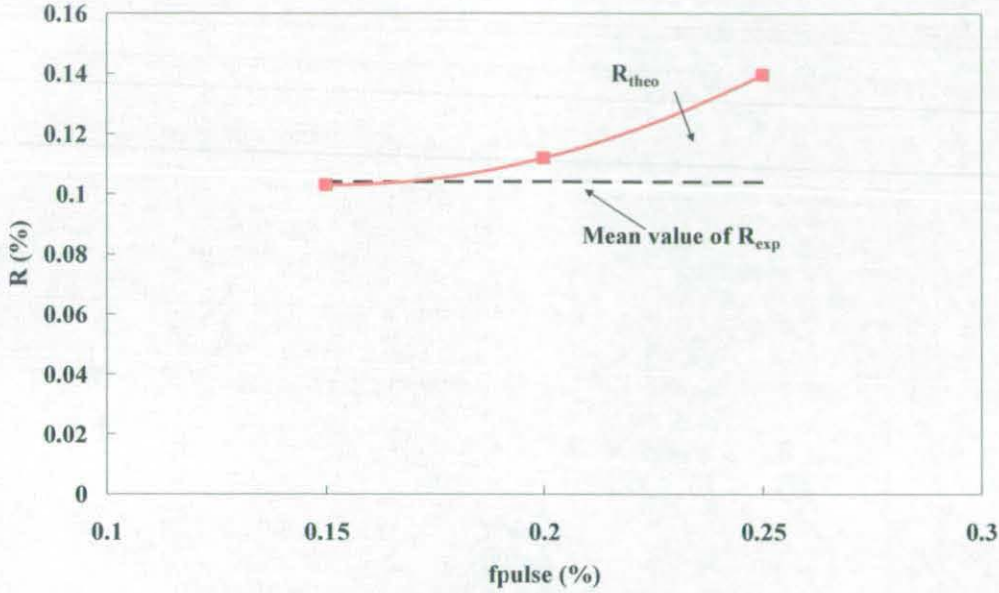


Figure 6. 24 The results of R calculated from Equation 5. 15 based on tissue models with different volume fraction of pulsatile blood. The blocks represent R corresponding to the volume fraction of pulsatile blood 0.25% (original setup), 0.20% and 0.15%, respectively.

The results in Figure 6. 23 and Figure 6. 24 demonstrate the effect of the thickness of epidermis layer and the volume fraction of pulsatile blood on R_{theo} . The epidermis is the top layer of the whole tissue model, and the change of the properties such as thickness in this layer leads to a significant effect on the whole light propagation in tissue. The change in volume fraction of pulsatile blood and thus the optical properties results in the change of $MPL'_{dynamic}$ and thus R_{theo} following Equation 5. 15 of the opto-physiological model. Consequently, the R_{theo} approaches the experimental result when increasing the thickness of the top layer and decreasing the pulsatile volume fraction. Thus a close-to-real tissue model will largely increase the accuracy and applicability of the current research.

6.4 RESULTS OF PERFUSION MAPPING

After validation, the opto-physiological model can thus be applied in biological measurements to construct blood perfusion mapping. Considering all the effects on the spatial resolution, i.e. the pixel resolution of camera, the tissue's spatial point spread function and the quality of IPPG signal, the size of ROI_{ip} is selected to be $100 \times 100 \text{ pixels}^2$ to guarantee the relatively high SNR of the IPPG signal in the experiment and also cover enough information to derive representative MPL. The size of ROI_{ip} may be decreased to maintain the basic structure when considering the limited size of the measurement sites such as fingers.

6.4.1 Experimental setup and protocol

The CMOS camera with the ring light was positioned 50 *mm* from the tissue surface. The camera was configured to capture 30*fps* at a resolution of $1280 \times 1024 \text{ pixel}^2$. The ring light was configured to illuminate at a single wavelength 870nm, and the output power reached 8mW by setting the forward current for each RCLED as 10mA. A female subject participated in this investigation. All the measurements were performed in a dark room to avoid the ambient light.

6.4.2 2-D Mapping of Static and dynamic component

As described previously about the mapping function in Figure 5. 16 in section 5.3, the 2-D mappings of static and dynamic components were based upon *dc* and *ac* which can illustrate the average tissue state and perfusion strength respectively.

6.4.2.1 Static component mapping

The 2-D mapping and the corresponding contour plot of ROI_{ip} -dependent *dc* under 870nm illumination on the human hand are presented in Figure 6. 25.

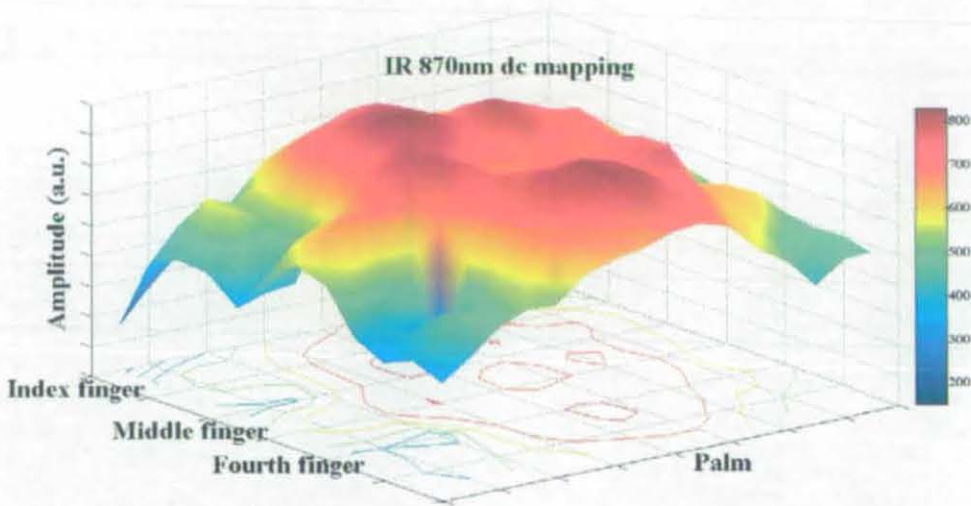


Figure 6. 25 The mapping of ROI_{ip} -dependent dc under 870nm illumination plotted in the 2-D and contour formats.

Figure 6. 25 demonstrates a direct visualisation of the static component of tissue, in which the finger and palm can be clearly distinguished. In Figure 6. 25, the dc of the palm shows higher values than that of the finger. This is due to the uneven surface of the hand. When the hand is laid flat on a surface, the palm usually protrudes more than the finger; thus the light illumination on the palm is stronger compared to the adjacent tissue areas. This results in the higher value of dc .

6.4.2.2 Dynamic component mapping

The 2-D blood perfusion mapping and the corresponding contour plot of ROI_{ip} -dependent ac calculated by Equation [5. 9] and R by Equation [5. 11] under 870nm illumination on the hand are presented in Figure 6. 26 and Figure 6. 27.

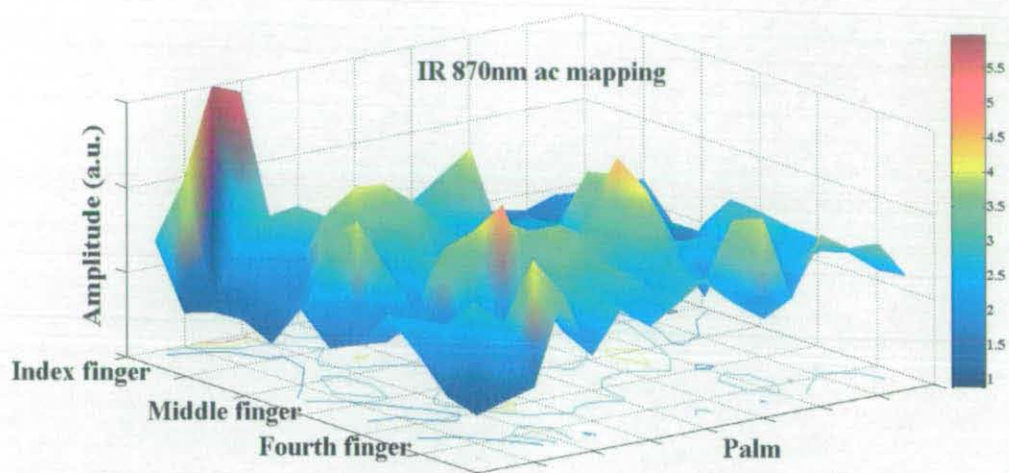


Figure 6. 26 The mapping of ROI_{ip}-dependent ac under 870nm illumination plotted in the 2-D and contour formats.

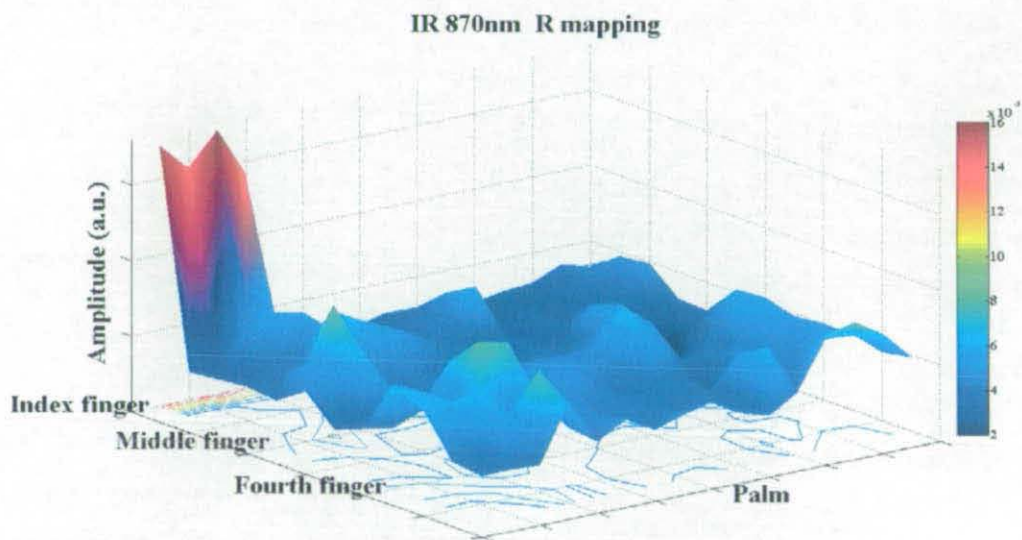


Figure 6. 27 The mapping of ROI_{ip}-dependent R under 870nm illumination plotted in the 2-D and contour formats.

In Figure 6. 27, the variation of the normalised amplitude is smaller than that in Figure 6. 26, as *R* is mainly attributed to the optical properties of blood following the Equation [3. 15].

In Figure 6. 27, the abnormal amplitude in the area of the index figure may come from the effect of motion artefact. Although motion artefact has no significant effect on heart rate, it can not be overlooked when generating perfusion mapping. Figure 6.

28(a) and (b) present the original image and the corresponding perfusion mapping of ac from the human face. Similarly as the results of the hand, motion artefact has a severe effect on the quality of perfusion mapping in Figure 6. 28(b). In this investigation, a simple method is developed to reduce the effect of motion artefact on perfusion mapping. This method is based upon the power mapping generated by averaging the amplitude of the AC spectrum at the bandwidth of interest as shown in Figure 6. 29. Motion artefact mainly induces lower or higher frequency noise than the HR frequency^[89]. To avoid the effect of motion artefact, the power mapping was generated by mapping the amplitude, named as ac_{power} , at the HR fundamental frequency i.e. 1.3Hz in frequency domain over the illuminated area as shown in Figure 6. 28(c).

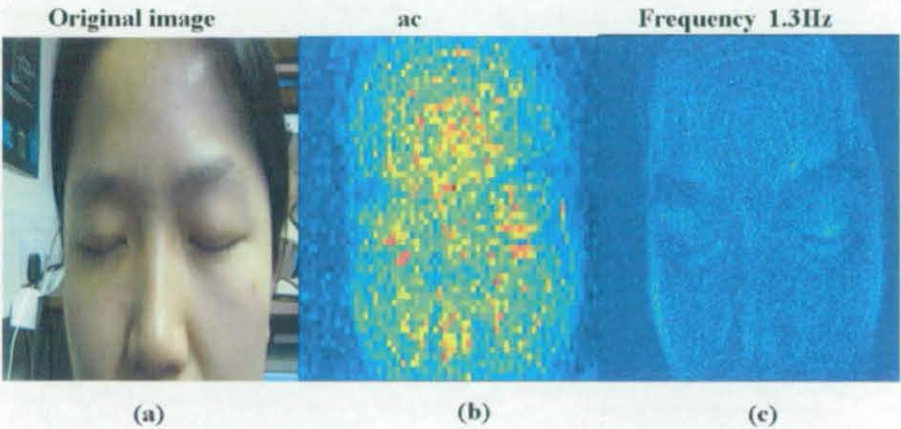


Figure 6. 28 (a) The original image. (b) Corresponding ac map. (c) Corresponding ac power map at HR = 1.3 Hz.

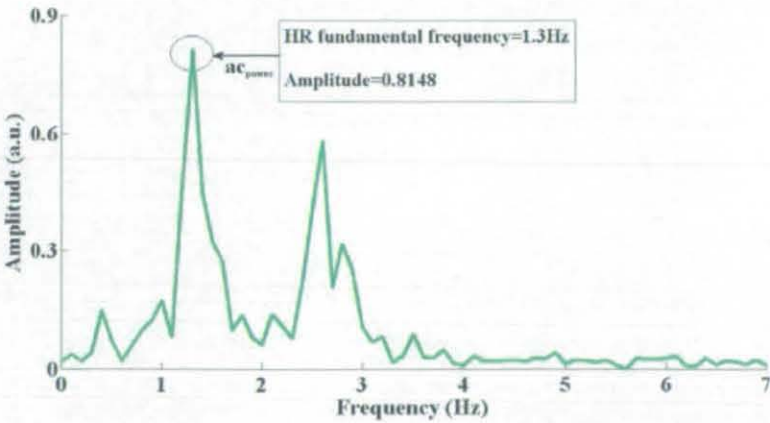


Figure 6. 29 An illustration of ac_{power} of the IPPG signal.

Figure 6. 28(c) shows the capability of the power mapping in reducing the effect of motion artefact. Based on this approach, the normalised pulsatile power R_{power} can be calculated as

$$R_{power} = \frac{ac_{power}}{dc} \quad [6. 9]$$

The 2-D mapping of ROI_{ip}-dependent R_{power} is presented in Figure 6. 30.

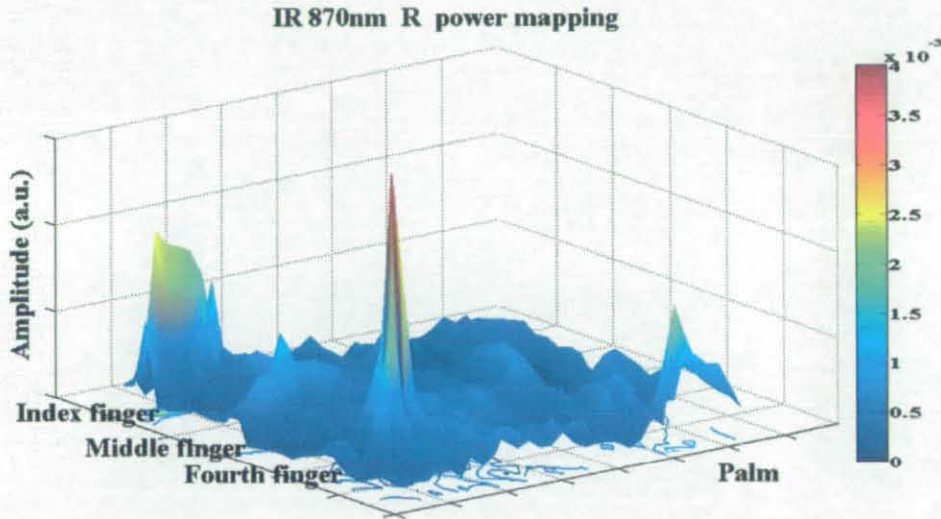


Figure 6. 30 The 2-D mapping of R_{power} under 870nm illumination on hand.

Figure 6. 30 indicates a better result of blood perfusion mapping than that in Figure 6. 27, especially in the palm area, where the effect of motion artefact has been reduced in most areas.

6.4.3 Layered Mapping of Blood Perfusion

In this section, the results of constructing the 3-D layered blood perfusion mapping using the opto-physiological model are detailed and discussed. Based upon the MPL' yielded by simulation in Table 6.2, the layered mapping was constructed following the procedure as shown in Figure 5. 18 in section 5.3.2.

The segmented ROI_{ip}-dependent R_{power} calculated from Equation [6. 9] under 870nm illumination is plotted in a 3-D format to illustrate the layered dynamic blood perfusion of the illuminated hand as shown in Figure 5. 4.

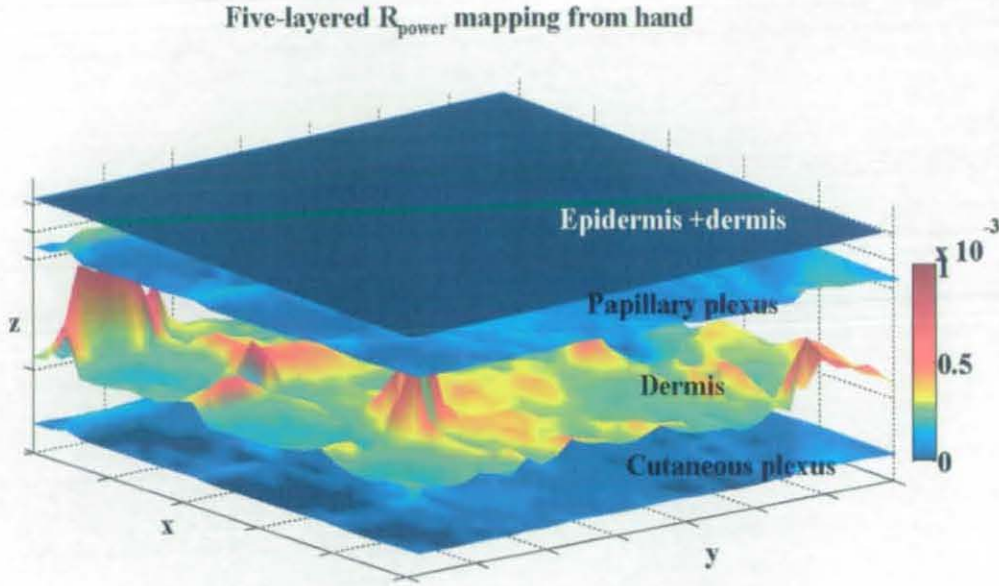


Figure 6. 31 The layered power mapping of ROI_{ip} -dependent R_{power} of the multi-layer skin tissue under 870nm illumination.

Through this, the IPPG signal is quantitatively related with the layered optical properties of each layer. By mapping the layered components of R of each ROI_{ip} , all the points within layered tissue's spatial point spread function in Figure 5.23 contribute to the ROI_{ip} -dependent R . Such kind of layered mapping illustrates the relationship between segmented AC and DC signal, and the relationship between segmented signal and the total IPPG signal.

Figure 5. 4 indicates that the deep dermis layers are the main contributor to blood perfusion up to 80% of the total perfusion, which is in accordance with simulation setup and empirical value. As the top two layers contain no pulsatile blood, there is no blood perfusion. Based upon the current results, when the geometry of individual layers of tissue is static and identical, the normalised layered power mapping can mainly provide information about optical properties of tissue.

The spatial resolution decreases with respect to depth as shown in the contour plot of tissue's spatial point spread function in Figure 5.23 and so these layered mapping does not provide a true representation of the actual physical distribution of light. To achieve this, the spatial distribution needs to convolve the corresponding tissue's spatial point spread function at each layer.

The current approach does suffer from the uncertainty of the degree of correspondence between this model and the real tissue. The uncertainty has been demonstrated in Figure 6. 23 and Figure 6. 24 by the simulation based on the tissue model with different thickness epidermis. Consequently, this research would greatly benefit from an accurate measurement of the internal makeup of the tissue bed. More discussions are detailed into the next chapter of further work.

7. CONCLUSIONS AND FURTHER WORK

This chapter summarises the experimental results of this research and the resultant conclusions. These are followed by a discussion of the areas which warrant further research and development, as suggested by the conclusions. Specifically, improvements are suggested to enhance the accuracy of the simulation for actual human tissue, including the implementation of other optical technologies to generate tissue models for simulation, the development of a proprietary MC simulation engine specific for this application to allow a much higher efficiency in the simulation process, and the more close-to-real setting for the tissue model including tissue optical properties.

7.1 CONCLUSIONS

In this research, an opto-physiological model was created to quantify the effect of optical properties on the IPPG signal through the use of MC simulation on multi-layered biological tissue. The approach to achieving this involved the redefinition of the path length in the Beer-Lambert law with mean path length (*MPL*). *MPL* was yielded by the MC simulation on a multi-layered tissue model with segmented close-to-real optical properties. Based upon this approach, the opto-physiological model was generated to mathematically describe the relationship of the output IPPG signal and the layered optical properties in a complex tissue structure. A series of *in-vitro* and *in-vivo* experiments were performed to provide reference outputs for the validation of the model. The validity of such data is a function of the quality of convergence achieved when correlating the results of experiment measurements with the corresponding data of the opto-physiological model. The quality of convergence depends on both the quality of experimental data and the accuracy of the tissue model employed in the MC simulation. After validation, the model was applied into the biological measurement to construct the 3-D mapping of layered blood perfusion.

7.1.1 Opto-Physiological Modelling

A linear increase in the accuracy of a model for optical propagation in biological tissue results in an exponential increase in its complexity. The thesis aims to create an accurate, yet applicable model to describe the effect of optical properties on the output signal in a complex tissue structure. The basic concept of this is to describe the complicated light-tissue interaction by a simplified representation with optimised parameters. This concept was achieved through the use of the MC simulation on multi-layered tissue model defined by close-to-real optical properties and geometries. The simulation yielded *MPL* for the opto-physiological model. Based upon *MPL* and the optical properties, the opto-physiological model was generated to quantify the effect of layered optical properties on the absorbance A and IPPG signals. The segmented A and IPPG signals for a specific tissue layer were hence derived as a directly linear function of the corresponding absorption coefficients μ_a when the scattering effect was constant.

7.1.2 Experiments

To validate the opto-physiological model, a custom IPPG setup and a series of *in-vitro* and *in-vivo* experimental protocols were generated towards high reliability standards. The accuracy of validation depends greatly on the quality of experimental outputs, which served as reference for the validation of the opto-physiological model. The validation platform configuration included a standard arrangement of reflection-mode IPPG and a RCLED ring light. The results demonstrated the capability of the IPPG system to detect quality and reliable signals from different tissue areas.

7.1.3 Validation

The concept of the validation is that as the assumptions and parameters of the opto-physiological model approach those occurring in the corresponding real-life experiment, the outputs of the opto-physiological model and the experiment increasingly correlate. Results of the *in-vitro* validation based upon the multi-layered phantom demonstrated a good correlation between the outputs of experiments and the opto-physiological model. This correlation proves the capability of the opto-physiological model, which not only can accurately predict the output in the range of μ_a and μ_s close to human tissue, but also predict the effect of changes of μ_a and μ_s on the output. In the *in-vitro* validation, the greatest deviation from the correlation occurred at the lowest and highest absorption coefficients. This was due to the spectrometer having insufficient sensitivity in these ranges. In the *in-vivo* validation, certainly variations between the outputs of experiments and the model were expected, due to the unknown effect of the surface reflection and the sensitivity of the current approach. The theoretical R_{theo} approaches the experimental result when increasing the thickness of the top layer and decreasing the pulsatile volume fraction of the tissue model.

7.1.4 Perfusion Mapping

The layered mapping illustrates the relationship between segmented AC and DC signal, and the relationship between segmented signal and the total IPPG signal. The

spatial resolution of the 2-D and layered perfusion mapping is determined by the size of ROI_{ip} , which is affected by the resolution of the captured frame, the quality of the IPPG signal and the tissue's spatial point spread function. Through the perfusion mapping, the IPPG signal is quantitatively related with the segment optical properties of each layer. By mapping the layered components of R of each ROI_{ip} , all the points within layered tissue's spatial point spread function in Figure 5.23 contribute to the ROI_{ip} -dependent R . The R_{power} mapping indicates that the deep dermis layers are the main contributor to blood perfusion up to 80% of the total perfusion, which is in accordance with simulation setup and empirical value. As the top two layers contain no pulsatile blood, there is no blood perfusion. Main issues limiting the accuracy of the current approach are the motion artefact and the uncertainty of the degree of correspondence between this model and the real tissue. To address the first, the data processing of spatial averaging and power mapping of interested bandwidth has been developed. Furthermore, this issue may be further addressed by improved positioning of the volunteers, software to laterally synchronize frames and more uniform illumination. For the uncertainty of the tissue model, this research would greatly benefit from an accurate measurement of the real tissue. More discussions are detailed into the next section of the further work.

7.2 FURTHER WORK

7.2.1 Effective Monte-Carlo Engine

OptiCAD was used as a prototype for a MC engine in order to perform a feasibility study in the least possible amount of time. Unfortunately, its limitations have proven to be a hindrance even at these early stages of platform development. Firstly, the software is closed source and is protected by a hardware key, which poses several problems. Processing power applied to MC simulation is limited to that of a single workstation and its rate of data output is severely limited as a consequence. Also, the data output of OptiCAD is an ASCII text file, which poses a bottleneck when importing the data into MATLAB. Finally, the output data does not include information pertaining to the medium in which ray segments are contained. A significant amount of reverse engineering was necessary to overcome this issue.

The limitations posed by the use of OptiCAD make it essential to develop an open-source MC engine in a flexible and efficient programming language such as C/C++. A proprietary engine specific to the application presented in this research would inherently remove the bottlenecks and unnecessary steps found in the current implementation. An open-source solution would allow the possibility of distributed computing, the ongoing optimisation of the platform, and the development of new features.

7.2.2 Close-to-real Tissue model

MC simulation in this project was performed on a flat, empirical tissue model; therefore, the degree of correspondence between this model and the real tissue has an important impact on the accuracy of the opto-physiological model. Consequently, this research would greatly benefit from an accurate measurement of the internal makeup of the tissue bed in question. Some optical tomographic technologies might be suitable to produce cross-sectional images of designated tissue area, such as MRI or optical coherence tomography (OCT).



Figure 7.1 DICOM image from MRI scan of adult male hand performed in Glenfield Hospital, University Hospital of Leicester, UK.

An example image of a MRI scan from an adult finger is shown in Figure 7.1. The resultant data indicates that the information gathered from MRI scans with low resolution can only be used to determine the major dimensions and positions of internal structures such as blood vessels.

The limitations posed by the use of OptiCAD make it essential to develop an open-source MC engine in a flexible and efficient programming language such as C/C++. A proprietary engine specific to the application presented in this research would inherently remove the bottlenecks and unnecessary steps found in the current implementation. An open-source solution would allow the possibility of distributed computing, the ongoing optimisation of the platform, and the development of new features.

7.2.2 Close-to-real Tissue model

MC simulation in this project was performed on a flat, empirical tissue model; therefore, the degree of correspondence between this model and the real tissue has an important impact on the accuracy of the opto-physiological model. Consequently, this research would greatly benefit from an accurate measurement of the internal makeup of the tissue bed in question. Some optical tomographic technologies might be suitable to produce cross-sectional images of designated tissue area, such as MRI or optical coherence tomography (OCT).

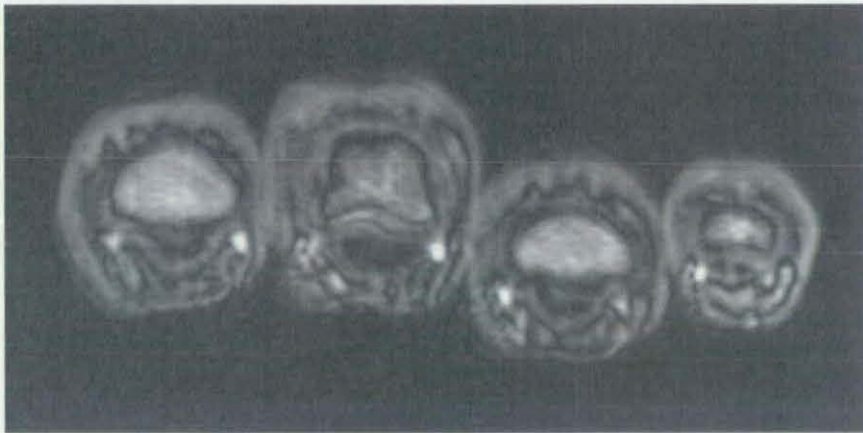


Figure 7.1 DICOM image from MRI scan of adult male hand performed in Glenfield Hospital, University Hospital of Leicester, UK.

An example image of a MRI scan from an adult finger is shown in Figure 7.1. The resultant data indicates that the information gathered from MRI scans with low resolution can only be used to determine the major dimensions and positions of internal structures such as blood vessels.

OCT is another optical tomography modality with high resolution and cross-sectional imaging. An example image of OCT from the layered retina is shown in Figure 7.2.

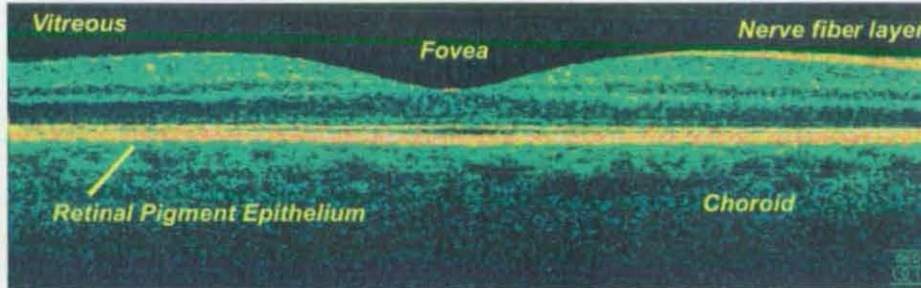


Figure 7.2 An example image of OCT scan of a retina at 800nm with an axial resolution of $3\mu\text{m}$ (image courtesy of <http://en.wikipedia.org/wiki/File:Retina-OCT800.png>).

OCT^[90] is particularly suited to ophthalmic applications and other tissue imaging requiring micrometer resolution and millimetre penetration depth. However, its imaging penetration is limited to millimetre depth, due to the highly scattering property of the medium. If the advantage of MRI scanning and OCT can be integrated to provide a high resolution and whole structure tissue model, it will largely increase the accuracy and applicability of the current research.

7.2.3 Model Settings

MC simulations were performed on a five-layered skin model without taking the melanin layer into account. Therefore, a more accurate methodology should include modelling of melanin in the epidermis. Additionally, it would be ideal to account for the inhomogeneity and the geometry change during the pulsatile stage.

With the complexity of the model increasing, the rate of data production in the current MC simulation poses a significant limitation. Any experiment that could elucidate potential ways to increase the efficiency of ray tracing is therefore justified. One such experiment would be to perform a series of comparative simulations to determine the relationship between ray traces resulting from three-dimensional arbitrary geometry and a corresponding two-dimensional simulation of a specific cross-section of the full geometry. If little geometrical variation is expected with respect to a change in cross-section, it may be possible to simplify the simulation to

two dimensions while still maintaining the precise nature of results resulting from an arbitrary geometry. Another feature that should be considered is the virtual definition of the light source, which was limited to a near-point source with Lambertian distribution. Characterisation of responses with respect to the light source beam parameters would be advantageous as an expansion of the capabilities of the platform.

It is clear that the accuracy of coefficients plays an important part in the accuracy of the opto-physiological model. In the context of this project, there is a need for full relational reviews of optical properties in which coefficients are given certain ranges with respect to relevant physiological parameters such as perfusion. As the availability and accuracy of these coefficients increases, so will the convergence of the results from this platform. As model settings of this sort are improved, it is possible that inverse Monte Carlo techniques of arbitrary geometries could be used to determine increasingly accurate *in-vivo* optical properties of biological tissues.

7.2.3 Dynamic Component Validation

When considering the perfusion as tissue with dynamic blood volume change, this change is simulated by adding the pulsatile blood into the non-pulsatile tissue and thus changing the volume fraction of each component. Consequently, this leads to the variation of μ_a and μ_s in tissue. The current validation was performed using static layered phantom but with different μ_a and μ_s . The phantom-based validation using multi-layered phantom with different μ_a and μ_s proves the ability of the opto-physiological model, which not only can accurately predict the output in the range of μ_a and μ_s close to human tissue, but also predict the effect of changes of μ_a and μ_s on the output. The changes of μ_a and μ_s can be related to the dynamic change, and this means the dynamic part of the opto-physiological model has been validated through in-vitro validation. This kind of validation for the dynamic component can also be achieved by using a phantom with an artificial vessel network pumped with a blood substitute. This leads a further work for this research.

REFERENCE

-
- [¹] Wardell K. and Nilsson G.E., "Duplex Laser Doppler Perfusion Imaging," *Microvasc. Res.*, **52**, pp. 171-182 (1996).
- [²] Chen Z. P, Milner T. E., Srinivas S., Wang X. J., Malekafzali A., VanGemert M. J. C., and Nelson J. S., "Noninvasive imaging of in vivo blood flow velocity using optical Doppler tomography," *Optics Letters*, **22**(14), 1119-1121 (1977).
- [³] Hertzman A.B., "Photoelectric plethysmography of the fingers and toes in man," *Proc. Soc. Exp. Biol. Med.*, **37**, pp. 529-534 (1937).
- [⁴] Allen J., "Photoplethysmography and its application in clinical physiological measurement," *Physiol. Meas.*, **28**, pp. R1- R39 (2007).
- [⁵] Dubois A.B., "New method for measuring airway resistance in man using a body plethysmography-values in normal subjects and in patients with respiratory disease," *J. Clin. Inv.*, **35**(3), pp 327-335 (1956).
- [⁶] Hertzman A.B., "The blood supply of various skin areas as estimated by the photoelectric plethysmography," *AM. J. Physiol.*, **124**, pp. 329-340 (1938).
- [⁷] Allen J., "Photoplethysmography assessments in cardiovascular disease," *Meas. Contr.*, **39**(3), pp. 80-83 (2006).
- [⁸] Allen J., "Microvascular blood flow and skin temperature changes in the fingers following a deep inspiratory gasp," *Physiol. Meas.*, **23**(2), pp. 365-373 (2002).
- [⁹] Benfeldt E., "In vivo microdialysis for the investigation of drug levels in the dermis and the effect of barrier perturbation on cutaneous drug penetration.

-
- Studies in hairless rats and human subjects," *Acta Derm. Venereol. Suppl.*, **206**, pp. 1–59 (1999).
- [¹⁰] Nijboer J.A., Dorlas J.C., Mahieu H.F., "Photoelectric plethysmography-some fundamental aspects of the reflection and transmission method," *Clin. Phys. Physiol. Meas.*, **2(3)**, pp. 205-215 (1981).
- [¹¹] Cartwright C.M., "Infrared transmission of the flesh," *J. Opt. Soc. Amer.*, **20**, pp. 81-84 (1930).
- [¹²] Yelderman M. and New W., "Evaluation of pulse oximetry," *Anesthesiology*, **59**, pp. 349-352 (1983).
- [¹³] Irvine W.M. and Pollack J.B., "Infrared optical properties of water and ice spheres," *Icarus*, **8**, pp.324-360 (1968).
- [¹⁴] Sarna T. and Sealy R. C., "Photoinduced oxygen-consumption in melanin systems-action spectra and quantum yields for eumelanin and synthetic melanin," *J. Photochem. Photobiol.*, **39(1)**, pp.69-74 (1984).
- [¹⁵] Srinivasan S., Pogue B. W., Jiang S. D. Dehghani H., Kogel C., Soho S., Gibson J. J., Tosteson T. D., Poplack S. P. and Paulsen K. D., "Interpreting haemoglobin and water concentration, oxygen saturation, and scattering measured in vivo by near infrared breast tomography," *PNAS*, **100(21)**, 12349-12354 (2003).
- [¹⁶] Wray S., Cope M., Delpy D.T., Wyatt J.S. and Reynolds E.O., "Characterization of the near infrared absorption spectra of cytochrome aa3 and haemoglobin for the non-invasive monitoring of cerebral oxygenation," *Biochimica et Biophysica Acta.*, **933(1)**, pp. 184-192 (1988).

-
- [¹⁷] Mannheimer P.D., Casciani J.R., Fein M.E, and Nierlich S.L., "Wavelength selection for low saturation pulse oximetry," *IEEE Trans. Biomed. Eng.*, **44**(3), pp. 148-158 (1997).
- [¹⁸] Konig V., Huch R., and Huch A. "Reflectance pulse oximetry-principles and obstetric application in the zurich system," *J. Clin. Monit.*, **14**, pp. 403-412 (1998).
- [¹⁹] Meglinskin I. V. and Matcher S. J., "Computer simulation of the skin reflectance spectra," *Comput. Meth. Programs Biomed.*, **70**, pp. 179-186 (2003).
- [²⁰] Reuss J., "Multilayer modelling of reflectance pulse oximetry," *IEEE Trans. Biomed.*, **52**, pp.153-160 (2005).
- [²¹] Standness D. E. and Bell J. W., "Peripheral vascular disease: diagnosis and objective evaluation using a mercury strain gauge," *Ann. surg.*, **161**, pp. 4-35 (1965).
- [²²] Trafford J.D. and Lafferty K., "What does photoplethysmography measure?" *Med. Biol. Eng. Comput.*, **22**, pp. 479-480 (1984).
- [²³] Lindberg L.G. and Oberg P.A., "Photoplethysmography. II. Influence of light source wavelength," *Med. Biol. Eng. Comput.*, **29**, pp. 48-54 (1991).
- [²⁴] Abramowitz H.B., Queral L.A., Flinn W.R. and Nora P.F., "The use of photoplethysmography in the assessment of venous insufficiency: a comparison to venous pressure measurement," *Surgery*, **86**, pp. 434-441 (1979).
- [²⁵] Barnes R.W., "Noninvasive diagnostic techniques in peripheral vascular disease," *Am. Heart J.*, **97**, pp. 2-9 (1979).

-
- [²⁶] Nitzan M., Boer H.D., Turivenko S., Babchenko A. and Sapoznikov D., "Spontaneous oscillation in the peripheral circulation system, as measured by photoplethysmography," *SPIE*, **2328**, pp. 188-195 (1994).
- [²⁷] Brown T.R., Goldstein B. and Little J., "Severe burns resulting from magnetic resonance imaging with cardiopulmonary monitoring. Risks and relevant safety precautions," *Am. J. Phys. Med. Rehabil.*, **72(3)**, pp. 166-167 (1993).
- [²⁸] Briers J. D., "Laser Doppler, speckle and related techniques for blood perfusion mapping and imaging," *Physiol.Meas.*, **22**, pp. R35-R66 (2001).
- [²⁸] Briers J. D., "Laser Doppler, speckle and related techniques for blood perfusion mapping and imaging," *Physiol. Meas.*, **22**, pp. R35-R66 (2001).
- [²⁹] Shi P., Zhu Y. S., Allen J., and Hu S. J., "Analysis of pulse rate variability derived from photoplethysmography with the combination of lagged poincare plot and spectral characteristics," *Med. Eng. Phys.*, **31(7)**, pp. 866-871(2009).
- [³⁰] Loukogeorgakis S., Dawson R., Phillips N., Martyn C. N. and Greenwald S. E., "Validation of a device to measure arterial pulse wave velocity by a photoplethysmographic method," *Physiol. Meas.*, **23**, pp. 581-596 (2002).
- [³²] Zheng J. and Hu S., "The preliminary investigation of imaging photoplethysmographic system", *J. of Physics: Conference Series*, **85**, pp. 012031 (2007).
- [³³] Wieringga F.P., Mastik F., and Van Der Steen A.F.W., "Contactless Multiple Wavelength Photoplethysmographic Imaging: A First Step Toward 'SpO2 Camera' Technology," *Ann. Biomed. Eng.*, **33(8)**, pp. 1034-1041(2005).

-
- [³⁴] Humphreys K. and Ward T., "Noncontact simultaneous dual wavelength photoplethysmography: A further step toward noncontact pulse oximetry," *Rev. Sci. Instrum.*, **78**, pp. 044304 (2007).
- [³⁵] Niazi Z.B.M., Essex T.J.H., Papini R., Scott D., McLean N.R. and Black M.J.M., "New laser Doppler scanner, a valuable adjunct in burn depth assessment," *Burns*, **19**, pp. 485-489 (1993).
- [³⁵] Hulsbusch M. and Blazek V., "Contactless Mapping of Rhythmical Phenomena in Tissue Perfusion Using PPGL," *Proc. of SPIE.*, **4683**, pp. 110-117(2002).
- [³⁷] Verkruysse W., Svaasand L. O., and Nelson J. S., "Remote plethysmography imaging using ambient light," *Opt. Express*, **16 (26)**, pp. 21434-21225 (2008).
- [³⁸] Wolpaw J. R., Birbaumer N., and Heetderks W.J. et al., "Brain-computer interface technology: A review of the first international meeting," *IEEE Trans. Rehabil. Eng.*, **8(2)**, pp. 164-173 (2000).
- [³⁹] Wolpaw J.R., Birbaumer N., McFarland D.J., Pfurtscheller G. and Vaughan T.M., "Brain-computer interface for communication and control," *Clin. Neurophysiol.*, **113**, pp. 767-791 (2002).
- [⁴⁰] Eda H., Kuroda Y., Okamoto N. and Maesako T., "NIRS evaluates the thinking process of Mushi-kuizan task," *Proc. of SPIE*, **68502**, pp. 1-6 (2008).
- [⁴⁰] Churmakov D.Y., Meglinski I.V. and Greenhalgh D.A., "Influence of refractive index matching on the photon diffuse reflectance," *Phys. Med. Biol.*, **47**, pp. 4271-4285 (2002).

-
- [⁴²] Bolin F. P., Preuss L. E., Taylor R. C. and Ference R. J., "Refractive index of some mammalian tissues using a fiber optic cladding method," *Appl. Opt.*, **28**, pp. 2297-2303 (1989).
- [⁴³] Schmitt J. M., Zhou G. X., Walker E.C. and Wall R.T., "Multilayer model of photon diffusion in skin," *J. Opt. Soc. Am. A*, **7**(11), pp. 2141-2153 (1990).
- [⁴⁴] Van Gemert M.J., Jacques S.L., Sterenborg H.J. and Star W.M., "Skin optics," *IEEE Trans. Biomed. Eng.*, **36**(12), pp. 1146-1154 (1989).
- [⁴⁵] Mie G., "Contributions to the optics of diffuse media, especially colloid metal solutions," *Ann. Phys.*, **25**, pp. 377-445 (1908)
- [⁴⁶] <http://omlc.ogi.edu/classroom/ece532/class3/scatterers.html>.
- [⁴⁷] Michael R. Hamblin, Ronald W. Waynant and Juanita Anders, "Mechanisms for Low-Light Therapy", *Proc. of SPIE*, **6140**, 614001(2006).
- [⁴⁸] Tuchi V.V., "Light scattering study of tissues," *PHYS-USP*, **40**, pp. 495-515, (1997).
- [⁴⁹] Davies C., Takatani S., Sakakibara N. and Nose Y., "Application of the Kubelka Munk equation to characterizing a reflectance pulse oximeter," *Proc. Int. Conf. IEEE Eng. Med. Biol. Soc.*, **4**, pp. 1095-1097 (1989).
- [⁵⁰] Patterson M. S., Wilson B. C. and Wyman D. R., "The propagation of optical radiation in tissue I. Models of radiation transport and their application," *Laser. Med. Sci.*, **6**(2), pp. 158-168.
- [⁵¹] Marble D.R. and Cheung P.W., "Mathematical model of transmission pulse oximetry," *Proc. Annu. Int. Conf. IEEE Eng. Med. Biol. Soc.*, **2**, pp. 534-542 (1988).

-
- [⁵²] Schmitt J.M., "Simple photon diffusion analysis of the effects of multiple scattering on pulse oximetry," *IEEE Trans. Biomed. Eng.*, **38**(12), pp. 1194-1203 (1991).
- [⁵³] Marble D.R., Burns D.H. and Cheung P.W., "Diffusion-based model of pulse oximetry: In vitro and in vivo comparisons," *Appl. Opt.*, **33**(7), pp. 1279-1285 (1994).
- [⁵⁴] Takatani S. and Graham M.D., "Theoretical analysis of diffuse reflectance from a two-layer tissue model," *IEEE Trans. Biomed. Eng.*, vol. 26, no. 12, pp. 656-664, (1979).
- [⁵⁵] Metropolis N. and Ulam S., "The Monte Carlo Method," *J. of the American Statistical Association*, **44**(247), pp. 335-341 (1949).
- [⁵⁶] Graaff R., Dassel A.C., Zijlstra W.G., De Mul F.F., and Aarnoudse J.G., "How tissue optics influences reflectance pulse oximetry," *Adv. Exp. Med. Biol.*, **388**, pp. 117-132 (1996).
- [⁵⁷] Wood E.H., "Apparatus for determining percentage oxygen-saturation in blood," United States Patent No:2706927 (1955).
- [⁵⁸] Mendelson Y., "Pulse oximetry: theory and applications for noninvasive monitoring," *Clin. Chem.*, **38**, pp. 1602-1607 (1992).
- [⁵⁹] Delpy D. T., Cope M., Vanderzee P., Arridge S. R., Wray S. and Wyatt J. S., "Estimation of optical pathlength through tissue from direct time of flight measurements," *Phys. Med. Biol.*, **33**, pp. 1433-1442(1988).
- [⁶⁰] Cope M., Delpy D. T., Reynolds E. O., Wray I., Wyatt J. and Vanderzee P. "Methods of quantitating cerebral near infrared spectroscopy data," *Adv. Exp. Med. Biol.*, **222**, pp. 183-189 (1988)

- [⁶¹] Matcher S. J., Cope M. and Delpy D. T., "Use of water absorption spectrum to quantify tissue chromophore concentration changes in near-infrared spectroscopy," *Phys. Med. Biol.*, **38**, pp. 177–196 (1993).

- [⁶²] Cope M., "The development of a near infrared spectroscopy system and its application non-invasive monitoring of cerebral blood and tissue oxygenation in newborn infant," *PHD thesis*, University of London.

- [⁶³] Duncan A., Meek J. H., Clemence M., Elwell C., Tyszczuk L., Cope M. and Delpy D. T., "Optical pathlength measurements on adult head, calf and forearm and the head of the newborn infant using phase resolved optical spectroscopy," *Phys. Med. Biol.*, **40**, pp. 295–304(1995).

- [⁶⁴] Vanderzee P., Cope M., Arridge S. R., Essenpreis M., Potter L. A., Edwards A. D., Wyatt J. S., McCormick D. C., Roth S. C. and Reynolds E. O., "Experimentally measured optical pathlengths for the adult head, calf and forearm and the head of the newborn infant as a function of inter optode spacing," *Adv. Exp. Med. Biol.*, **316**, pp. 143-153 (1992)

- [⁶⁵] Takatani S., "On the theory and development of a non-invasive tissue reflectance oximeter," Ph.D. dissertation, Case Western Reserve University, Cleveland, Ohio (1978).

- [⁶⁶] Wan S., Anderson R.R. and Parrish J.A., "Analytical modelling for the optical properties of the skin with in vitro and in vivo applications," *Photochem. Photobiol.*, **34**, pp. 493-499 (1981).

- [⁶⁷] Anderson R.R., Hu J. and Parrish J.A., "Optical radiation transfer in the human skin and applications in in vivo remittance spectroscopy," *Proc.of the Symposium on Bioengineering and the Skin*, pp. 253-313 (1980).

- [⁶⁸] Bruls W.A.G. and Van Der Leun J.C., "Forward scattering properties of human epidermal layers," *Photochem. Photobiol.* **40**, pp. 231-242 (1984).

-
- [⁶⁹] Pologe J.A., "Pulse oximetry: technical aspects," *Int. Anesthesiol. Clin.*, **25(3)**, pp. 137-153 (1987).
- [⁷⁰] Vilokkinen V., Sipila P., Melanen P., Saarinen M., Orsila S., Dumitrescu, P. Savolainen M., Toivonen M., and Pessa M., "Resonant cavity light-emitting diodes at 660nm and 880nm", *Materials Sci. and Eng.*, **B74**, pp. 165-167 (2000).
- [⁷¹] Drexler B., Davis J. L., and Schofield G., "Diaphanography in the diagnosis of breast cancer," *Radiology*, **157**, pp. 41-44 (1985).
- [⁷²] Waterworth M.D., Tarte B.J., Joblin A.J., Van Doorn T. and Niesler H.E., "Optical transmission properties of homogenised milk used as a phantom material in visible wavelength imaging," *Australas. Phys. Eng. Sci. Med.* **18(1)**, pp. 39-44 (1995).
- [⁷⁴] Zhao Z. and Myllyla R., "The effect of optical scattering on pulsed photoacoustic measurement in weakly absorbing liquids," *Meas. Sci. Technol.*, **12**, pp. 172-2177 (2001).
- [⁷⁵] Vanveen R. L. P., Sterenborg H., Pifferi A., Torricelli A., and Cubeddu R., "Determination of VIS- NIR absorption coefficients of mammalian fat, with time- and spatially resolved diffuse reflectance and transmission spectroscopy," *Biomedical Topical Meeting*, pp SF4 (2004).
- [⁷⁶] Pogue B. W. and Patterson M. S., "Review of tissue simulating phantoms for optical spectroscopy, imaging and dosimetry," *J. Biom. Opt.*, **11**, pp. 041102 (2006).
- [⁷⁶] Moes C., Gemert M., Star W., Marijnissen J. and Prah S., "Measurements and calculations of the energy fluence rate in a scattering and absorbing phantom at 633nm," *Appl. Opt.*, **28(12)**, pp. 2292-2296 (1989).

- [⁷⁸] Zhao Z. and Myllyla R., "The effect of optical scattering on pulsed photoacoustic measurement in weakly absorbing liquids," *Meas. Sci. Technol.*, **12**, pp. 172-2177 (2001).

- [⁷⁸] Kohen E., Santus R. and Hirschberg J.G. "Photobiology," *Academic* (1995).

- [⁷⁹] Zonios G., Dinou A., Bassukas I., Galaris D., Tsolakidis A., Kaxiras E., "Melanin absorption spectroscopy: new method for noninvasive skin investigation and melanoma detection," *J. Biomed Opt.*, **13**(1), 014017 (2008).

- [⁸⁰] <http://omlc.ogi.edu/news/jan98/skinoptics.html>

- [⁸¹] Marozas M. and R. Jurkonis, "Review on skin lesion imaging, analysis and automatic classification," *Conference Biomed. Eng.*, pp. 109-114 (1999).

- [⁸²] Nickell S., Hermann M., Essenpreis M., Farrell T.J., Kramer U., and Patterson M.S, "Anisotropy of light propagation in human skin," *Phys. Med. Biol.*, **45**(10), pp. 2873-2886 (2000).

- [⁸³] Enejder A.M., Swartling J., Aruna P. and Andersson-Engels S., "Influence of cell shape and aggregate formation on the optical properties of flowing whole blood," *Appl. Opt.*, **42**(7), pp. 1384-1394 (2003).

- [⁸⁴] Bolin F.P., Preuss L.E., Taylor R.C., and Ference R.J., "Refractive index of some mammalian tissues using a fiber optic cladding method," *Appl. Opt.*, **28**, pp. 2297-2303 (1989).

- [⁸⁵] Ai-qadiri H., Lin M., Ai-holy A., Cavinato A. and Rasco B., "Monitoring quality loss of pasteurized skin milk using visible and short wavelength near-infrared spectroscopy and multivariate analysis," *J. Dairy Sci.*, **91**, pp. 950-958 (2007)

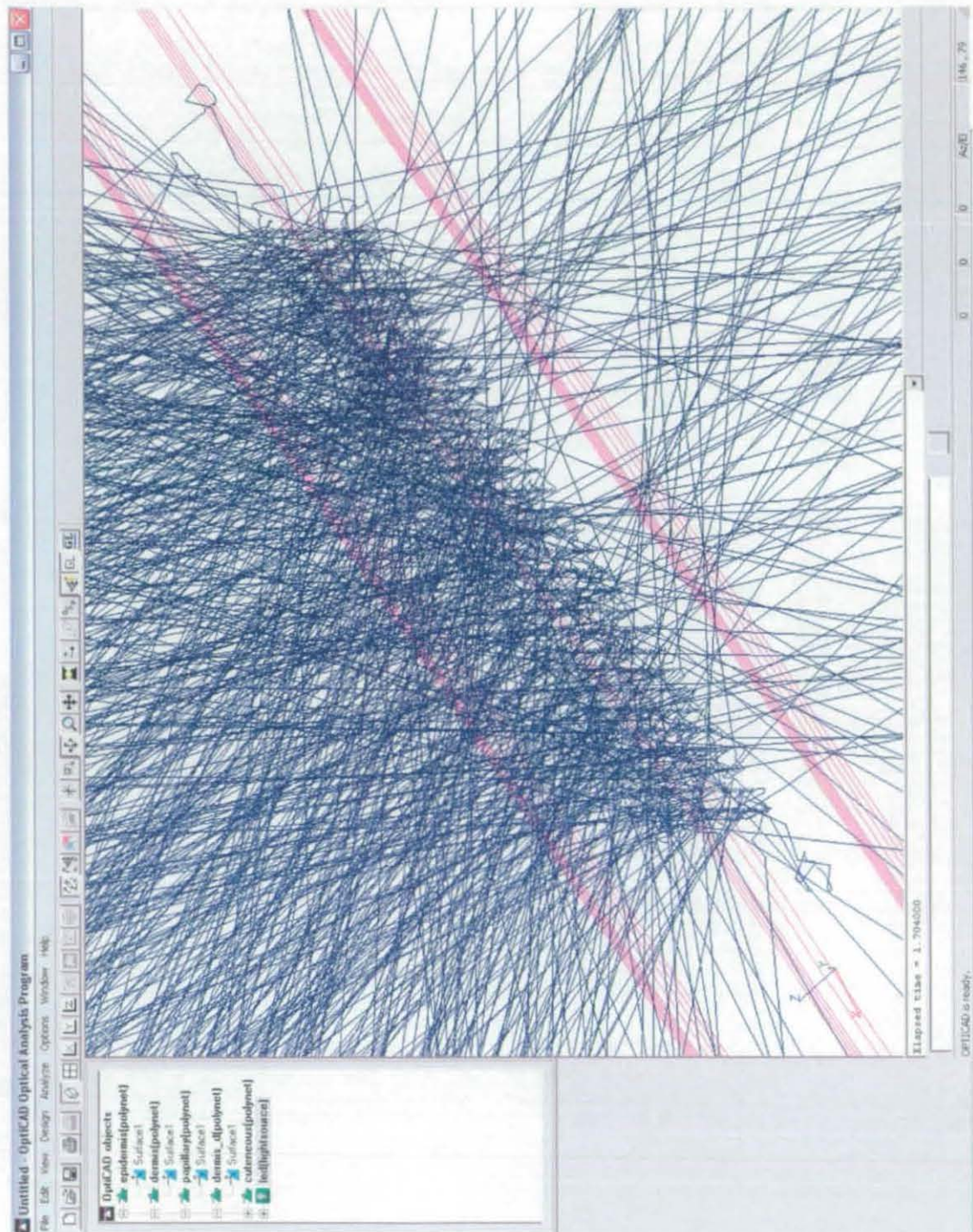
- [⁸⁶] Allan J and Murray A, "Age-related changes in the characteristics of the photoplethysmographic pulse shape at various body sites," *Phys. Meas.* **24**(2), pp. 297-307 (2003).
- [⁸⁷] Altman D.G. and Bland J.M., "Measurement in medicine: the analysis of method comparison studies," *The Statistician*, **32**, pp. 307-317 (1983).
- [⁸⁸] Morgan S. P. and Stockford I. M., "Surface-reflection elimination in polarization imaging of superficial tissue," *Optic. Lett.*, **28**(2), pp. 114-116 (2003).
- [⁸⁹] Hayes M. J. and Smith P. R., "A new method for pulse oximetry possessing inherent insensitivity to artifact," *IEEE Trans. Biom. Eng.*, **48**(4), 452-461.
- [⁹⁰] Schmitt J. M., "Optical coherence tomography (OCT): A review," *IEEE. J. Selected Topics in Quantum Electronics*, **5**(4), pp. 1205-1215 (1999).

APPENDICES

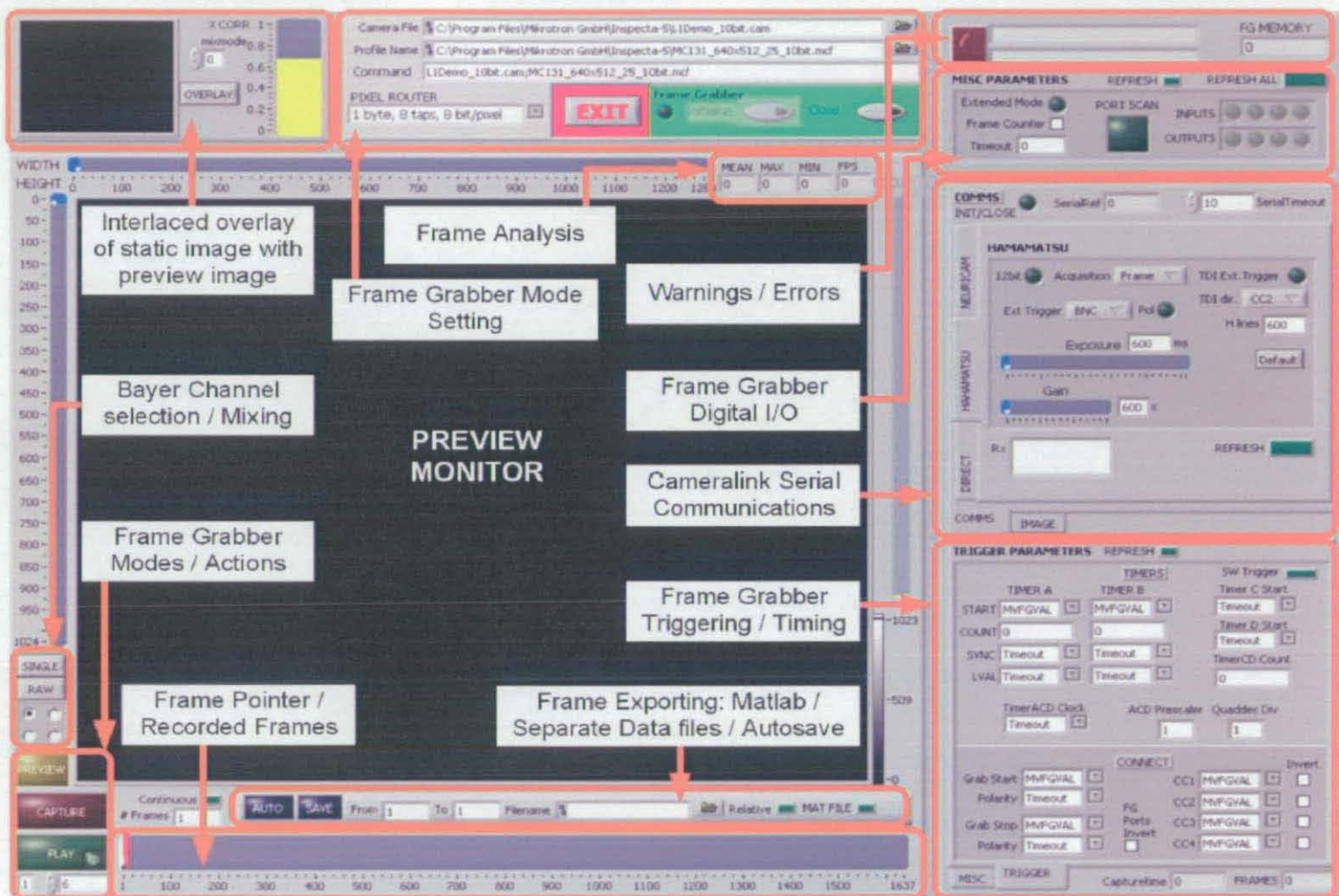
The following appendices have been included:

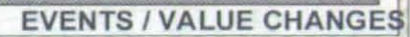
- I. Graphical user interface for OptiCAD software (OptiCAD Corporation, USA).
- II. LabVIEW front panel and block diagram for the virtual instrument developed for the control of the Inspecta-5 frame grabber (Mikrotron, Germany) and communications with a range of cameras via the CameraLink serial interface.
- III. LabVIEW front panel and block diagram for the virtual instrument developed for the control of the DISCO4 PPG board (Dialog Devices, UK) and USB data acquisition device NI-DAQ M-6015 (National Instruments, USA).
- IV. Specification and optical properties of dye, FD&C #1 (ROHA CALEB Ltd., UK).

I GRAPHICAL USER INTERFACE OF OPTICAD

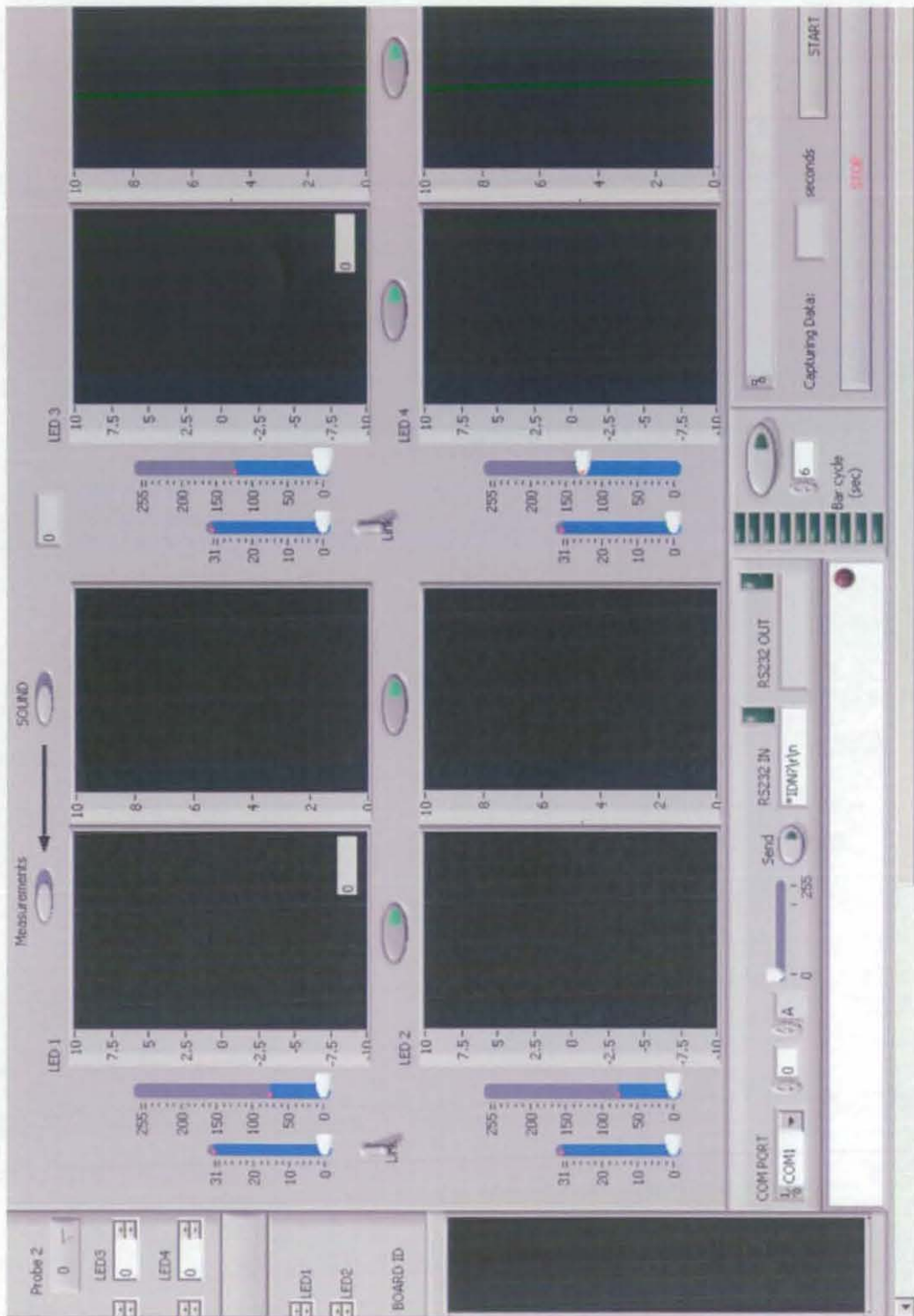


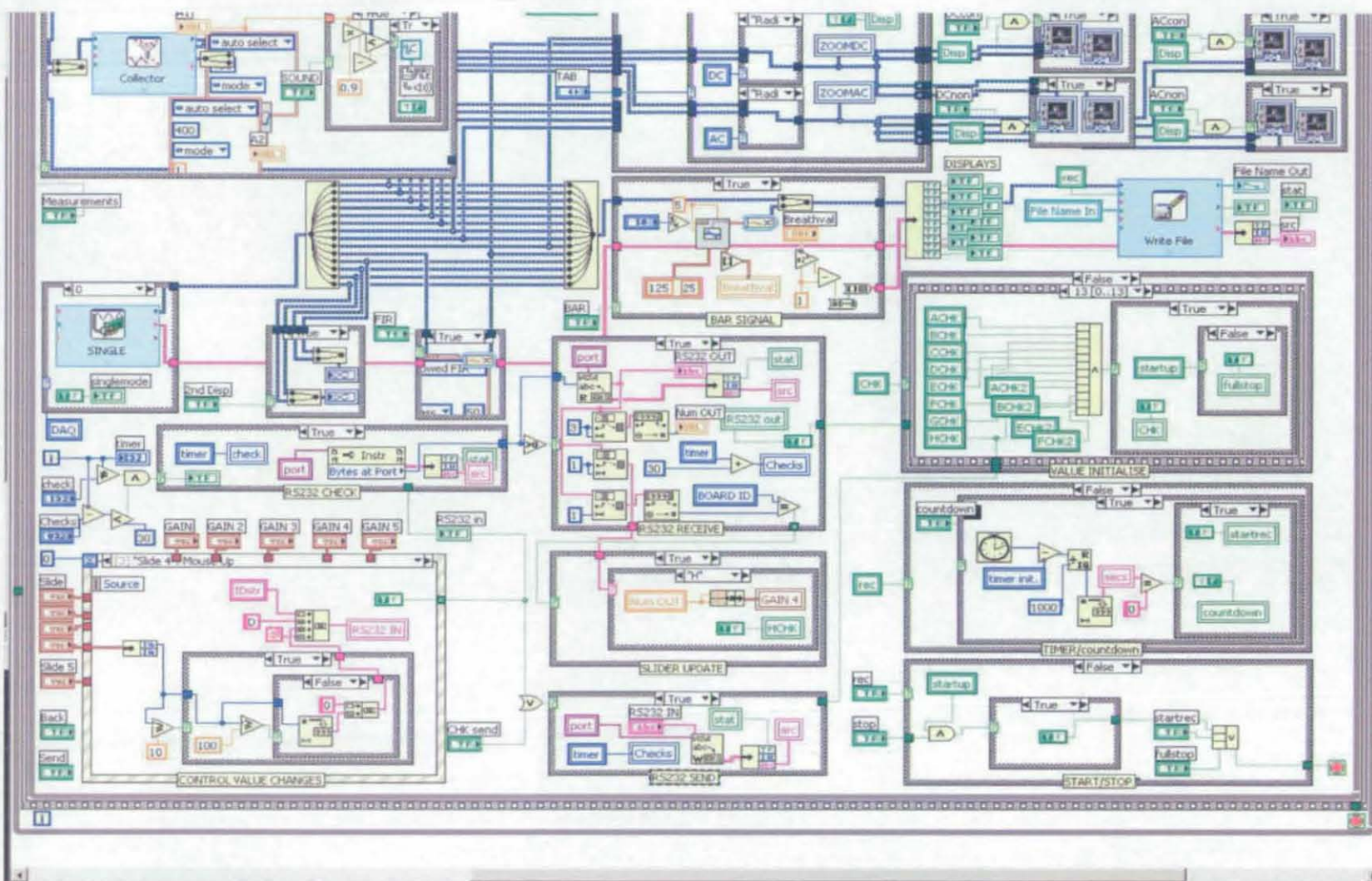
II. LABVIEW APPLICATION FOR FRAME GRABBER





III LABVIEW APPLICATION FOR DISCO4 PPG BOARD





VI OPTICAL PROPERTIES OF FD & C BLUE # 1

The dye, FD&C Blue #1 (ROHA Ltd. UK), was selected as one of the main components of the phantom to increase light absorption preferentially at 650 nm. The dye, also known as Brilliant Blue FCF, is a colorant for food and other substances to induce a colour change with the appearance of a reddish-blue powder. It is soluble in water, thus the scattering coefficient is negligible when it is fully dissolved. The solution has a maximum absorption at 629 nm. Its molecular weight is 792.84 g/mol. The dye solution performs in a stable way over temperature (up to 100 °C) and time (up to days).

The measurement of the absorption of dye used a spectrophotometer (USB4000, Ocean Optics Inc., USA) and a tungsten halogen lamp (LS-1, Ocean Optics Inc., USA) in a transmission method. The calculation of absorption coefficients is usually quoted to be a base-10 format in the Beer-Lambert law because of the relation to optical density. The absorption A can be described as:

$$A = -\log\left(\frac{I}{I_0}\right) = \varepsilon_a \times C \times d \quad \text{[A-1]}$$

where

C the concentration of dye with units of $M(\text{mol} / l)$,

d the thickness of cuvette with units of mm ,

ε_a the wavelength-dependent molar absorption coefficient with units of $M^{-1}mm^{-1}$,

I_0 and I the incident and transmitted intensity,

A the absorption.

Equation A-1 is satisfied by distilled water:

$$A = -\log\left(\frac{I_w}{I_0}\right) = \varepsilon_{a,w} \times C \times d \quad [\text{A-2}]$$

Assuming the absorption coefficient of water is negligible, the absorption is approximate to 0 and the incident light intensity can be represented by the transmitted light intensity of water I_w .

In the actual measurement of absorption coefficient of a dye solution, the dark noise of the camera itself was subtracted from the transmitted light intensity. Thus Equation A-1 can be modified as:

$$A = -\log\left(\frac{I - I_{dark}}{I_w - I_{dark}}\right) = \varepsilon_a \times C \times d \quad [\text{A-3}]$$

where

I the transmitted light intensity from sample

I_w the transmitted light intensity from distilled water

I_{dark} the dark noise of the device.

When fixing the thickness of the cuvette, the molar absorption coefficient ε_a of a

dye solution is deduced to be proportional to the slope of the $\log\left(\frac{I - I_{dark}}{I_w - I_{dark}}\right) - C$ plot,

as shown in Figure A.1.

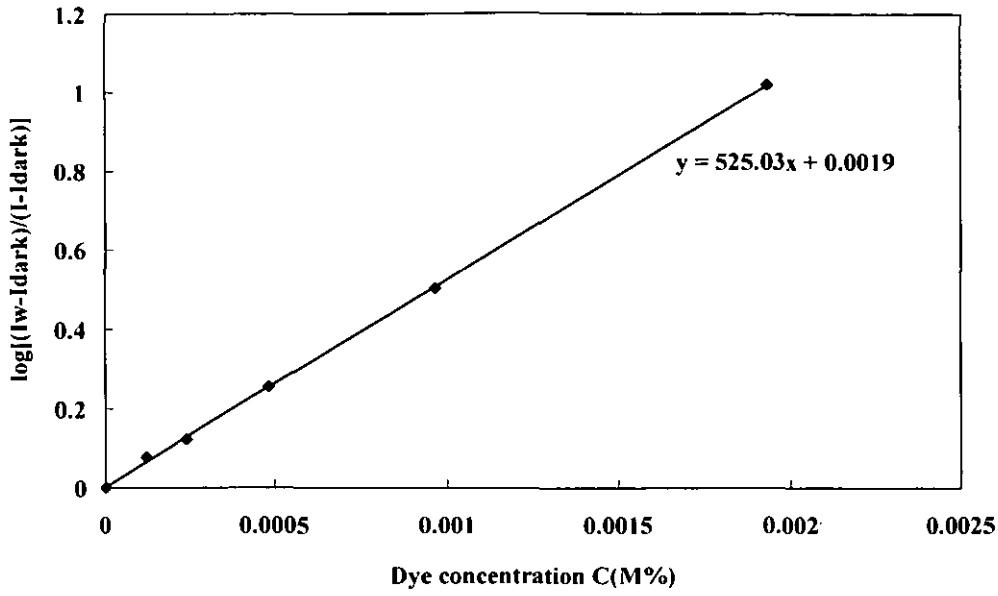


Figure A.1 The relationship between the absorption and dye concentration.

Performing a linear least squares regression, the molar absorption coefficients of dye, measured using the cuvette with thicknesses of 10 mm, is calculated as $\varepsilon_a = 52.503 \text{ mm}^{-1} / (\%C)$. For a specific concentration of dye solution, the absorption coefficient μ_a can be derived as:

$$\mu_a = \varepsilon_a \times C \quad [\text{A-4}]$$

where

ε_a the molar absorption coefficient

C the concentration of dye solution.

